Universidade do Minho
Escola de Engenharia

André Gustavo Silva de Macedo

Multi-responsive structures based on electroactive polymers and hydrogels as a novel approach for tissue engineering

janeiro de 2026

Multi-responsive structures based on electroactive polymers and hydrogels as a novel approach for tissue engineering

André Gustavo Silva de Macedo

UMinho | 2026



Universidade do Minho
Escola de Engenharia

André Gustavo Silva de Macedo

Multi-responsive structures based on electroactive polymers and hydrogels as a novel approach for tissue engineering

Tese de Doutoramento
Engenharia de Materiais

Trabalho efetuado sob a orientação de
Doutora Clarisse Marta de Oliveira Ribeiro
Professor Doutor Senentxu Lanceros-Méndez
Doutora Vanessa Fernandes Cardoso

janeiro de 2026

DIREITOS DE AUTOR E CONDIÇÕES DE UTILIZAÇÃO DO TRABALHO POR TERCEIROS

Este é um trabalho académico que pode ser utilizado por terceiros desde que respeitadas as regras e boas práticas internacionalmente aceites, no que concerne aos direitos de autor e direitos conexos.

Assim, o presente trabalho pode ser utilizado nos termos previstos na licença abaixo indicada.

Caso o utilizador necessite de permissão para poder fazer um uso do trabalho em condições não previstas no licenciamento indicado, deverá contactar o autor, através do RepositóriUM da Universidade do Minho.

Licença concedida aos utilizadores deste trabalho



Atribuição-NãoComercial

CC BY-NC

https://creativecommons.org/licenses/by-nc/4.0/

Acknowledgements

This work signals the end of a journey only possible with the direct or indirect support of numerous people.

I want to thank the financial support by the Foundation for Science and Technology (FCT), grant 2020.09218.BD.

Firstly, great many thanks to all my supervisors: Clarisse Ribeiro, Vanessa Cardoso, and Professor Senentxu Lanceros-Méndez, for their ubiquitous availability and dedication, as well as the knowledge transmitted, which were essential for bringing the work to a successful completion.

To all elements of the Electroactive Smart Materials (ESM) group, to which Professor Senentxu opened its doors with his unwavering positivity, embodying an example in and of itself. I especially thank Ricardo, for his fraternity, and all my IB-S friends with whom I went somewhere with, literally and figuratively: Pedro, Joana and her friend Joana, Diana, Dinis and Soraia.

I would also like to thank the Centre of Physics and the Institute of Science and Innovation for Bio-sustainability of the University of Minho for providing access to the laboratory facilities and equipment.

To all elements of the BIOMAT group in beautiful Donostia, the stay supervisors Alaitz Etxabide, Koro de la Caba, and Pedro Guerrero, as well as Teresa and Maialen for being perfectly welcoming and their pervasive good disposition.

To all my friends, for the years and moments, especially Gil, Bruno, Susana, Luís, the Pedros and Rui.

To Ana, for being there, for accepting me for who I am, and for helping me in becoming a better version of myself.

To my parents, godmother and godfather, and those who came before them.

STATEMENT OF INTEGRITY

I hereby declare having conducted this academic work with integrity. I confirm that I have not used plagiarism or any form of undue use of information or falsification of results along the process leading to its elaboration.

I further declare that I have fully acknowledged the Code of Ethical Conduct of the University of Minho.

Resumo

A procura de soluções em engenharia de tecidos (ET) tem aumentado para responder à degeneração ligada ao envelhecimento ou a regeneração após trauma ou intervenção cirúrgica. O tecido ósseo é naturalmente piezoelétrico e a sua regeneração regulada por sinais elétricos, o que tem motivado estratégias de ET. Esta tese foca-se em produzir e caracterizar plataformas eletroativas e multiresponsivas nesta área. O documento encontra-se dividido em três secções principais, para além da introdução e conclusões, que apresentam alternativas inovadoras para estratégias de ET. A primeira centra-se no desenvolvimento de matrizes responsivas a estímulos de poly(3-hydroxybutyrate-*co*-3-hydroxyvalerate) (PHBV), um polímero piezoelétrico, em forma pura ou compósita por integração de nanopartículas magnéticas de Fe_3O_4, fabricadas através de moldes sacrificiais obtidos por impressão 3D. As matrizes compósitas com 10% de Fe_3O_4 mostram um efeito positivo na proliferação celular de pré-osteoblastos sob estímulo magnético. A segunda apresenta o refinamento da síntese de microesferas por técnicas de emulsão e *electrospray*. Os melhores resultados foram obtidos com a última, com esferas quase perfeitas apesar de polidispersas em tamanho. Estas microesferas expandem as morfologias magnetoelétricas e biomiméticas disponíveis. A terceira contém duas estratégias para o desenvolvimento de matrizes dinâmicas com resposta eletroativa e potencial libertação de fatores bioquímicos. Na primeira subsecção, gelatina foi conjugada com sericina, uma proteína extraída *in situ* de casulos de *Bombyx mori*, para produzir hidrogéis não reticulados impressos em 3D. Uma maior concentração de sericina induz maior resistência a solubilização, e o hidrogel comprovado não citotóxico. Na segunda, gelatina foi reticulada com diferentes metodologias e reticulantes: exposição a UV com riboflavina; reação de Maillard com frutose; e reticulação química usando 1-Ethyl-3-(3-dimethylaminopropyl) carbodiimida (EDC) e N-Hydroxysuccinimida (NHS). Estas estratégias produziram hidrogéis com diferentes perfis de degradação que variam de horas até mais de um mês. Os hidrogéis foram introduzidos nas matrizes poliméricas e compósitas desenvolvidas e estudados de acordo, comprovando-se também não citotóxicos. Os hidrogéis EDC-NHS, possuindo estabilidade estrutural e adesão celular superiores, foram selecionados para ensaios de proliferação. A presença de hidrogel e o estímulo magnetoelétrico mostraram-se benéficos, com maiores taxas de proliferação do que as suas contrapartes sem hidrogel ou sem estímulo. Em conjunto, este trabalho apresenta opções piezoelétricas, magnetoelétricas, e hidrogéis com eficácia comprovada como matrizes para ET que abrem caminhos para estratégias de regeneração usando estímulos dinâmicos e eletroativos de microambientes celulares.

Palavras-chave: compósitos magnetoelétricos; engenharia de tecidos ósseos; hidrogéis; impressão 3D; matrizes eletroativas

Abstract

Tissue engineering (TE) solutions are increasingly needed to address age-related degeneration and to accelerate recovery following trauma or surgical intervention. Bone is a naturally piezoelectric tissue whose regeneration is closely regulated by electrical cues, which has motivated bone TE research. This thesis focuses on designing and characterizing multiresponsive electroactive platforms in this field. The document is divided in three main sections, along an introduction and conclusions that present innovative approaches for TE strategies. The first concerns the development of stimuli-responsive piezoelectric poly(3-hydroxybutyrate-*co*-3-hydroxyvalerate) (PHBV) scaffolds both in pure polymer and composite form with the integration of magnetic Fe_3O_4 nanoparticles, fabricated using 3D-printed sacrificial molds. Composite 10% Fe_3O_4 scaffolds show a positive effect on MC3T3-E1 preosteoblast cell proliferation under magnetic stimulation. The second section presents the refinement of microsphere synthesis through emulsion and electrospray techniques. The latter ultimately provided the best results with nearly perfect sphere formation, although markedly polydisperse in size. These microspheres expand the available magnetoelectric biomimetic morphological approaches. The third section contains two different strategies for the development of dynamic scaffolds with electroactive response and potential release of biochemical factors. In the first subsection, gelatin was combined with sericin, a protein extracted *in situ* from *Bombyx mori* silk cocoons, to develop 3D-printable, non-crosslinked hydrogels. Higher sericin content induced higher resistance to solubilization, and the hydrogel was confirmed as non-cytotoxic. In the second subsection, gelatin was crosslinked using three methodologies and crosslinkers: UV exposure using riboflavin; the Maillard reaction using fructose; and chemical crosslinking using 1-Ethyl-3-(3-dimethylaminopropyl) carbodiimide (EDC) and N-Hydroxysuccinimide (NHS). These strategies yielded hydrogels with degradation profiles ranging from hours to over one month. The hydrogels were loaded into the polymer and composite scaffolds developed in the first section and studied accordingly. All hydrogels were confirmed as non-cytotoxic. EDC-NHS hydrogels, possessing superior structural stability and cell adhesion performance, were selected for proliferation assays. Both hydrogel presence and magnetoelectric stimulation were shown to be beneficial, with higher proliferation rates than the counterparts either without hydrogel or without stimuli. Together, this work presents piezoelectric, magnetoelectric, and hydrogel options with proven efficacy as TE scaffolds that open a multitude of avenues for regeneration strategies using electroactive dynamic stimulation of cell microenvironments.

Keywords: 3D printing; bone tissue engineering; electroactive scaffolds; hydrogels; magnetoelectric composites

Table of contents

ACKNOWLEDGEMENTS iii

RESUMO v

ABSTRACT vi

LIST OF FIGURES xii

LIST OF TABLES xv

LIST OF ACRONYMS xvi

LIST OF SYMBOLS xx

CHAPTER 1 – INTRODUCTION 1

1.1. CONTEXTUALIZATION 2

1.2. BONE BIOLOGY AND PHYSIOLOGY 3

1.3. BONE DISEASE 6

1.4. TISSUE ENGINEERING APPROACHES FOR BONE REGENERATION 7

1.5. MULTIFUNCTIONAL, RESPONSIVE AND ELECTROACTIVE MATERIALS 9

1.5.1. PIEZOELECTRIC MATERIALS 9

1.5.2. NANOMATERIALS 11

1.5.3. MAGNETOELECTRIC EFFECT 13

1.6. HYDROGELS 15

1.7. 3D PRINTING 18

1.8. Objectives and methodology 21

1.9. Thesis structure 22

Chapter 2 – 3D poly(3-hydroxybutyrate-*co*-3-hydroxyvalerate) scaffolds 38

2.1. Introduction 39

2.2. Materials and methods 40

2.2.1. Materials 40
2.2.2. 3D Printing of sacrificial molds 41
2.2.3. Preparation of 3D PHBV scaffolds 41
2.2.4. Morphological and physicochemical characterization 42
2.2.5. Cell studies 44
2.2.6. Cytotoxicity 44
2.2.7. Cell proliferation 45
2.2.8. Fluorescence microscopy 46
2.2.9. Statistical analysis 46

2.3. Results and discussion 46

2.3.1. Morphology, topology and piezoelectric response of the scaffolds 46
2.3.2. Physical and chemical characterization 49
2.3.3. Degradation studies 52
2.3.4. Cell studies 53
2.3.4.1. Cytotoxicity studies 53
2.3.4.2. Proliferation studies 54

2.4. Conclusions 56

Chapter 3 – Magnetically responsive electroactive polymer composite microspheres 62

3.1. Introduction 63

3.2. Materials and methods 64

3.2.1. Materials 64
3.2.2. Morphological and magnetic properties characterization 64
3.2.3. PHBV, Fe_3O_4@PHBV and $CoFe_2O_4$@PHBV microsphere preparation 64
3.2.4. Fe_3O_4@PVDF microsphere preparation 65

3.3. Results and discussion 65

3.3.1. PHBV and Fe_3O_4@PHBV microspheres 65
3.3.2. $CoFe_2O_4$@PHBV microspheres 66
3.3.3. Fe_3O_4@PVDF microspheres 67

3.4. Conclusions 68

Chapter 4 – Hydrogels 70
Subchapter 4.1 – 3D-printed hydrogels 71

4.1.1. Introduction 72

4.1.2. Materials and methods 73

4.1.2.1. Materials 73
4.1.2.2. Silk sericin extraction 74
4.1.2.3. Hydrogel preparation 74
4.1.2.4. Rheological assessment 74
4.1.2.5. 3D printing 75
4.1.2.6. Morphological and physicochemical characterization 75
4.1.2.7. Cytotoxicity 76

4.1.3. Results and discussion 76

4.1.3.1. Amino acid composition 76
4.1.3.2. Rheological properties of the hydrogels 78

4.1.3.3. Morphology of the 3D printed samples 79
4.1.3.4. Physicochemical properties 80
4.1.3.5. Swelling and degradation studies 82
4.1.3.6. Cytotoxicity studies 83

4.1.4. Conclusions 83

Subchapter 4.2 – Hydrogel films and loading into scaffolds 89

4.2.1. Introduction 90

4.2.2. Materials and Methods 92

4.2.2.1. Materials 92
4.2.2.2. Preparation of 3D PHBV scaffolds 92
4.2.2.3. Hydrogel preparation and loading into scaffolds 92
4.2.3.3.1. Gelatin-Riboflavin hydrogel 93
4.2.3.3.2. Gelatin-Fructose hydrogel 93
4.2.3.3.3. Gelatin-EDC-NHS hydrogel 94
4.2.2.4. Morphological and physicochemical characterization 94
4.2.2.5. Cell studies 95

4.2.3. Results and discussion 95

4.2.3.1. Morphology of the hydrogel-loaded 3D printed samples 95
4.2.3.2. Compression studies 97
4.2.3.3. Degradation studies 98
4.2.3.3.1. Solubility of the Gelatin-Riboflavin hydrogel films 98
4.2.3.3.2. Swelling of the Gelatin-Fructose hydrogel films 99
4.2.3.3.3. Hydrogel-loaded scaffold mass loss 99
4.2.3.3.4. Vibrational spectra of the hydrogel-loaded scaffold 101
4.2.3.3.5. Assessment of the degradation of the hydrogel-loaded scaffold 104
4.2.3.4. Cell studies 105

4.2.3.4.1. CYTOTOXICITY STUDIES 105
4.2.3.4.2. PROLIFERATION STUDIES 106

4.2.4. CONCLUSIONS 109

CHAPTER 5 – CONCLUSIONS AND FUTURE WORK 114

5.1. CONCLUDING REMARKS 115

5.2. FUTURE WORK 117

List of figures

Figure 1.1. Schematic representation of the macro and microstructure of long bone. Reproduced from [10], CC BY 4.0. 3

Figure 1.2. Schematic representation of the magnetoelectric effect in a composite scaffold seeded with cells. Upon application of a magnetic field, the magnetostrictive nanoparticles deform, inducing mechanical strain in the piezoelectric matrix. This deformation generates a localized electrical output, which can promote enhanced cell activity and proliferation..... 14

Figure 1.3. Illustration of an extrusion-based 3D printer equipped with a syringe containing a hydrogel with adequate rheological properties for printing. Hydrogels can be loaded with different elements (before or after printing), such as cells, nanoparticles, growth factors, or pharmaceutical compounds..... 20

Figure 2.1. a) BVOH 3D-printed sacrificial mold and corresponding b) printing parameters. 41

Figure 2.2. Representative images of the surface, cross-section and elemental composition of the pure and composite PHBV scaffolds via stereo microscopy, SEM, and SEM-EDX..... 47

Figure 2.3. Representative piezoresponse force microscopy images of the topography, phase and amplitude maps of two pure PHBV scaffolds. 48

Figure 2.4. a) DSC scans, b) FTIR-ATR spectra, c) mechanical compression stress-strain curves, and d) VSM hysteresis curves of the pure and composite PHBV scaffolds. 50

Figure 2.5. a) Contact angle and b) porosity values of the pure and composite PHBV scaffolds. 52

Figure 2.6. Representative images of the degradation suffered by the pure and composite PHBV scaffolds under static and dynamic conditions and when submerged in PBS and DMEM after 30 and 40 days. 53

Figure 2.7. Indirect cytotoxicity assay of MC3T3-E1 preosteoblasts in contact with the pure and composite PHBV scaffolds. 54

Figure 2.8. Cell proliferation of MC3T3-E1 preosteoblast culture after 7 days under static and dynamic conditions. The cell proliferation values of the pure and composite PHBV scaffolds were determined regarding the cells adhered on the material after 24 h adhesion, just before the first magnetic stimulus. The results are expressed as mean ± SD. **$p < 0.01$, ***$p < 0.001$..... 55

Figure 2.9. Fluorescence microscopy images of MC3T3-E1 cells adhered on the pure and composite PHBV scaffolds under static and dynamic conditions after 1 (T_0) and 7 days (T_1). 56

Figure 3.1. SEM images of a) PHBV and b) Fe_3O_4@PHBV microspheres prepared using an emulsion technique..... 65

Figure 3.2. SEM images of $CoFe_2O_4$@PHBV microspheres prepared using an emulsion technique..... 66

Figure 3.3. a) Room-temperature magnetic hysteresis cycles for the $CoFe_2O_4$@PHBV microspheres and $CoFe_2O_4$ nanoparticle and b) magnetic remanence (M_R), saturation magnetization (M_S), coercivity (H_C) and $CoFe_2O_4$ wt.% for the different samples. 66
Figure 3.4. SEM images of Fe_3O_4@PVDF microspheres prepared using the electrospray technique. 67
Figure 3.5. Histogram of Fe_3O_4@PVDF microsphere diameter by count. 68
Figure 4.1. a) Shear rate and b) temperature sweeps of the 3D printed samples at different sericin:gelatin ratios. 78
Figure 4.2. Digital photography images of the hydrogels at different sericin:gelatin ratios. 79
Figure 4.3. SEM images of the cross-section of the 3D printed samples with different sericin:gelatin ratios. 80
Figure 4.4. a) FTIR spectra and b) XRD patterns of neat proteins and 3D printed samples with different sericin:gelatin ratios. 81
Figure 4.5. Swelling behavior of the 3D printed samples at different sericin:gelatin ratios when immersed in PBS solution at 37 °C. 82
Figure 4.6. Indirect cytotoxicity assay of MC3T3-E1 preosteoblasts in contact with as-prepared extraction exposed to the SerGe3 hydrogel. 83
Figure 4.7. Illustration of the methods of crosslinking and crosslinkers combined with gelatin to prepare the different hydrogel-loaded PHBV scaffolds. 92
Figure 4.8. Stereo microscopy images of PHBV scaffolds loaded with gelatin hydrogels crosslinked by riboflavin (first row), fructose (second row and last position), and EDC-NHS (first and second images in the last row). (R1: 0.2% riboflavin, 1 h crosslinking; R2: 0.2% riboflavin, 2 h crosslinking; R3: 0.4% riboflavin, 2 h crosslinking; F1: pH 7, 80 °C; F2: pH 10, 80 °C; F3: pH 10, 110 °C)....96
Figure 4.9. Mechanical compression stress-strain curves of the Gelatin-Riboflavin, Gelatin-Fructose and Gelatin-EDC-NHS-loaded PHBV scaffolds (R1: 0.2% riboflavin, 1 h crosslinking; R2: 0.2% riboflavin, 2 h crosslinking; R3: 0.4% riboflavin, 2 h crosslinking; F1: pH 7, 80 °C; F2: pH 10, 80 °C; F3: pH 10, 110 °C). 97
Figure 4.10. Mass variation of the Gelatin-Fructose hydrogel films and Gelatin-EDC-NHS hydrogels over 30 days (F1: pH 7, 80 °C; F2: pH 10, 80 °C; F3: pH 10, 110 °C). 99
Figure 4.11. Average mass loss of PHBV scaffolds loaded with riboflavin and fructose-crosslinked gelatin hydrogels after 30 and 40 days, under static and dynamic conditions (F1: pH 7, 80 °C; F2: pH 10, 80 °C; F3: pH 10, 110 °C; R1: 0.2% riboflavin, 1 h crosslinking; R2: 0.2% riboflavin, 2 h crosslinking; R3: 0.4% riboflavin, 2 h crosslinking)....100

Figure 4.12. FTIR-ATR spectra of the interior and exterior of PHBV scaffolds loaded with Gelatin-Riboflavin hydrogels before and after immersion in water (R1: 0.2% riboflavin, 1 h crosslinking; R2: 0.2% riboflavin, 2 h crosslinking; R3: 0.4% riboflavin, 2 h crosslinking); before (Day 0) and after immersion in water for 10 days; and the interior (INT) or exterior (EXT) of the scaffolds. 101
Figure 4.13. FTIR-ATR spectra of the interior and exterior of PHBV scaffolds loaded with Gelatin-Fructose hydrogels before and after immersion in water (F1: pH 7, 80 °C; F2: pH 10, 80 °C; F3: pH 10, 110 °C); before (Day 0) and after immersion in water for 10 days; and the interior (INT) or exterior (EXT) of the scaffolds. 102
Figure 4.14. FTIR-ATR spectra of the interior and exterior of PHBV scaffolds loaded with Gelatin-EDC-NHS hydrogels before and after immersion in water for 10 days.....103
Figure 4.15. Representative UV-Vis spectroscopy spectra of Gelatin-Riboflavin and Gelatin-Fructose-loaded PHBV scaffolds. PBS medium simples recovered after 7 days of immersion, under static conditions (F1: pH 7, 80 °C; F2: pH 10, 80 °C; F3: pH 10, 110 °C; R1: 0.2% riboflavin, 1 h crosslinking; R2: 0.2% riboflavin, 2 h crosslinking; R3: 0.4% riboflavin, 2 h crosslinking). 104
Figure 4.16. Indirect cytotoxicity assay of MC3T3-E1 preosteoblasts in contact with the Gelatin-Fructose and Gelatin-Riboflavin hydrogel films and Gelatin-EDC-NHS hydrogels. (F1: pH 7, 80 °C; F2: pH 10, 80 °C; F3: pH 10, 110 °C; R1: 0.2% riboflavin, 1 h crosslinking; R2: 0.2% riboflavin, 2 h crosslinking; R3: 0.4% riboflavin, 2 h crosslinking).....105
Figure 4.17. Cell proliferation of MC3T3-E1 preosteoblast culture after 4 days under static and dynamic conditions. The cell proliferation values of the pure and composite PHBV scaffolds both with and without the Gelatin-EDC-NHS hydrogel were determined regarding the cells adhered on the material after 24 h adhesion, just before the first magnetic stimulus. The results are expressed as mean ± SD. *** $p < 0.001$, ****$p < 0.0001$. 106
Figure 4.18. a) Composite of three layers of b), c), d) different z-axis focal points fluorescence microscopy images of MC3T3-E1 cells adhered on the same sample of a Gelatin-EDC-NHS hydrogel-loaded pure PHBV scaffold, under static conditions, after 4 days (T_1). 108

List of tables

Table 1.1. Some of the most important signaling molecules involved in bone metabolism. Information compiled from [7]. 5

Table 1.2. Representative examples of natural and synthetic piezoelectric materials, processed morphology, and corresponding piezoelectric coefficients. 10

Table 1.3. Classification of hydrogel crosslinking strategies according to physical and chemical methods, including representative techniques and examples for each category. Information compiled from [115]. 16

Table 2.1. Measurements of the areas, perimeter and circularity of the pores of the 3D pure and composite PHBV scaffolds. 47

Table 2.2. Crystallinity degree of the pure and composite PHBV scaffolds. 50

Table 4.1. Amino acid composition of the gelatin and sericin samples used for preparation of the hydrogels. 77

Table 4.2. n (flow index) and K (consistency index) fitting parameters of the power law model applied. Values are presented as mean ± SD. 79

Table 4.3. Averages for the areas of the central voids and the width of the printed lines in-between at different ratios of composition (sericin:gelatin) and corresponding values of the printable design (for comparison). Values are presented as mean ± SD. 79

Table 4.4. Frequency values for amide A, I, II and III bands in the FTIR spectra of neat proteins and 3D printed samples with different sericin:gelatin ratios. Values are presented as mean ± SD. 81

Table 4.5. Synthesis parameters of the gelatin-riboflavin UV-crosslinked hydrogels. 93

Table 4.6. Synthesis parameters of the gelatin-fructose temperature-crosslinked hydrogels. 93

Table 4.7. Young's modulus, elastic and plastic behavior values of the Gelatin-Riboflavin, Gelatin-Fructose and Gelatin-EDC-NHS-loaded PHBV scaffolds (R1: 0.2% riboflavin, 1 h crosslinking; R2: 0.2% riboflavin, 2 h crosslinking; R3: 0.4% riboflavin, 2 h crosslinking; F1: pH 7, 80 °C; F2: pH 10, 80 °C; F3: pH 10, 110 °C) 98

Table 4.8. Average mass loss of the Gelatin-Riboflavin hydrogel films after 24 h in water (R1: 0.2% riboflavin, 1 h crosslinking; R2: 0.2% riboflavin, 2 h crosslinking; R3: 0.4% riboflavin, 2 h crosslinking; F1: pH 7, 80 °C; F2: pH 10, 80 °C; F3: pH 10, 110 °C). 98

List of acronyms

2PP	Two-photon polymerization
AA	Amino acid
ABS	Acrylonitrile butadiene styrene
AFM	Atomic force microscopy
AM	Additive manufacturing
AMF	Alternating magnetic field
ANOVA	Analysis of variance
ASTM	American Society for Testing and Materials
ATP	Adenosine triphosphate
ATR	Attenuated total reflectance
$BaTiO_3$	Barium titanate
B. mori	*Bombyx mori*
BLC	Bone lining cell
BMP6	Bone morphogenetic protein 6
BVOH	Butenediol vinyl alcohol
CT-1	Cardiotrophin-1
CAD	Computer-assisted design
CaO	Calcium oxide
CTHRC1	Collagen triple helix repeat containing 1
DAPI	4′,6-diamidino-2-phenylindole
DART	Dual AC Resonance Tracking
diH_2O	Deionized water
DMEM	Dulbecco's Modified Eagle Medium
DMF	Dimethylformamide
DMSO	Dimethyl sulfoxide
DSC	Differential scanning calorimetry
EAP	Electroactive polymer
ECM	Extracellular matrix
EDC	1-Ethyl-3-(3-dimethylaminopropyl) carbodiimide
EDTA	Ethylenediaminetetraacetic acid
EDX	Energy-dispersive X-ray
EFNB2	EphrinB2
FBS	Fetal bovine serum
FDM	Fused deposition modeling
Fe_3O_4	Magnetite
FGF-2	Fibroblast growth factor 2
FITC	Fluorescein isothiocyanate
FTIR	Fourier transform infrared
GAG	Glycosaminoglycan

HA	Hydroxyapatite
HB	Hydroxybutyrate
HDPE	High-density polyethylene
HIPS	High-impact polystyrene
HSC	Hematopoietic stem cell
HV	Hydroxyvalerate
IGF-1	Insulin-like growth factor 1
ISO	International Organization for Standardization
KNN	Potassium sodium niobate
LVR	Linear viscoelastic region
M-CSF	Monocyte/macrophage colony-stimulating factor
ME	Magnetoelectric
MeHA	Methacrylated hyaluronic acid
MES	2-(N-morpholino)ethanesulfonic acid
MNP	Magnetic nanoparticle
MOF	Metal organic framework
MPP	Metalloproteinases
MR	Maillard reaction
MSC	Mesenchymal stem cell
NHS	N-Hydroxysuccinimide
Na_2O	Sodium oxide
NIR	Near-infrared
NP	Nanoparticle
OPG	Osteoprotegerin
P(VDF-TrFE)	Poly(vinylidene fluoride-*co*-trifluoroethylene)
P/S	Penicillin/streptomycin
P_2O_5	Phosphorus pentoxide
PA11	Polyamide 11
PAA	Polyacrylic acid
PAM	Polyacrylamide
PBS	Phosphate-buffered saline
PC	Polycarbonate
PCL	Poly(ε-caprolactone)
PEG	Poly(ethylene glycol)
PEO	Poly(ethylene oxide)
PET	Polyethylene terephthalate
PDGF-BB	Platelet-derived growth factor-BB
PFM	Piezoresponse force microscopy
PGA	Poly(glycolic acid)
PHA	Polyhydroxyalkanoate

PHBV	Poly(3-hydroxybutyrate-*co*-3-hydroxyvalerate)
PLA	Polylactic acid
PLGA	Polylactic-*co*-glycolic acid
PLLA	Poly(*L*-lactic acid)
PMMA	Polymethylmethacrylate
PNAGA	Poly(N-acryloyl glycinamide)
PNIPAm	Poly(N-isopropylacrylamide)
PP	Polypropylene
PPA	Polyphosphoric acid
PPF	Poly(propylene fumarate)
PPG	Polypropylene glycol
PS	Polystyrene
PVA	Polyvinyl alcohol
PVDF	Polyvinylidene fluoride
RANKL	Receptor activation of NF-κB ligand
ROS	Reactive oxygen species
RT	Room temperature
S1P	Sphingosine 1-phosphate
SA	Sodium alginate
SD	Standard deviation
SDF-1	Stromal-derived factor
SEM	Scanning electron microscopy
SEMA3A	Semaphorin 3A
SEMA4D	Semaphorin 4D
SiO_2	Silicon dioxide
SLA	Stereolithography
SLM	Selective laser melting
SLS	Selective laser sintering
SOST	Sclerostin
TCPS	Tissue culture polystyrene
TE	Tissue engineering
TGF-β	Transforming growth factor-β
THF	Tetrahydrofuran
TiO_2	Titanium dioxide
UP	Ultrapure
US	Ultrasound
UV	Ultraviolet
VEGF	Vascular endothelial growth factor
VSM	Vibrating sample magnetometry
WCA	Water contact angle

WNT10B	Wnt gene family 10B
WNT16	Wnt gene family 16
WNT5A	Wnt gene family 5A
XRD	X-ray Diffraction
YLD	Years lived with disability
ZnO	Zinc oxide
γ-Fe_2O_3	Maghemite

List of symbols

$\boldsymbol{ABS}$	Absorbance
$\boldsymbol{DW}$	Dry weight
$\boldsymbol{FW}$	Final weight
$\boldsymbol{G'}$	Storage modulus
$\boldsymbol{G''}$	Loss modulus
$\boldsymbol{H_C}$	Coercivity
$\boldsymbol{IW}$	Initial weight
$\boldsymbol{K}$	Consistency index
$\boldsymbol{M_R}$	Magnetic remanence
$\boldsymbol{M_S}$	Saturation magnetization
$\boldsymbol{n}$	Flow index
$\boldsymbol{SW}$	Swelled weight
$\boldsymbol{T_B}$	Blocking temperature
$\boldsymbol{T_C}$	Curie temperature
$\boldsymbol{W_S}$	Weight of sample
$\boldsymbol{X_C}$	Crystallinity degree
$\dot{\gamma}$	Shear rate
$\boldsymbol{\Delta H_{f^0}}$	100% crystalline fusion enthalpy
$\boldsymbol{\Delta H_f}$	Experimental fusion enthalpy
$\boldsymbol{\tau_0}$	Shear stress
η	Viscosity

CHAPTER 1

Introduction

1.1. Contextualization

From Prometheus' liver regrowing overnight, Eve's creation from Adam's rib, to the assembling of a living being from mismatched body parts in Mary Shelley's Frankenstein, concepts loosely relating to tissue engineering (TE) and regenerative medicine have, in one way or another, long belonged to humanity's imaginary. Curiously, the work of Mary Shelley, published in 1818, preceded what was arguably the first breakthrough in the modern view of TE: Johann Friedrich Dieffenbach's study on skin grafting in *Nonnulla de regeneratione et transplantatione*, published in 1822 [1, 2]. However, the practice of skin transplantation is reported as far back as 300 BCE in the *Sushruta Samhita* Sanskrit texts from ancient India, where nasal reconstruction was performed after mutilation as punishment for crimes [3].

TE utilizes components such as living cells, biocompatible materials, and biochemical and physical cues - such as growth factors or cyclic mechanical loading (the application of mechanical stress in a recurring and controlled manner). These elements are used alone or in combination to promote the creation of tissue-like structures. The end goal is often implantation into the body for regeneration, but extracorporeal life support systems containing cells (artificial organs, organ-on-a-chip), as well as tissue units for diagnostic screening are also common. Beyond clinical applications, other uses include drug testing for efficacy or toxicology, as well as basic studies on tissue development and morphogenesis [4].

Endogenous bioelectrical signals carried by ions and electrons mediate the regulation of many biological processes in the human body, with tissue regeneration as no exception. Stimulation using electricity, ultrasound, or magnetic fields can accelerate bone healing without the drawbacks associated with conventional treatments, such as the risk of infection and the limited availability of treatments for overly large bone defects [5]. Contrary to common misconceptions, bone tissue responds positively to high rates or frequencies of stimulation. It has been demonstrated that high-intensity impact training can preserve or even improve bone mass in postmenopausal women, who are especially susceptible to osteoporosis, when compared to low-intensity training [6]. This effect is partly attributed to bone's inherent piezoelectricity, its capacity to generate an electrical charge in response to small deformations induced by mechanical stress [5]. This natural bioelectrical property of bone serves as a key conceptual foundation for the present work. In the following sections, and with particular focus on this phenomenon, concepts and developments relating to bone TE will be explored.

1.2. Bone biology and physiology

The human skeletal system consists of 206 individual bones, amounting to approximately 15% of the total body weight of an average individual. Beyond providing mechanical support for movement and protection of vital organs, it also acts as a reservoir for minerals including calcium, phosphate and magnesium, as well as organic molecules including collagen fibers and amorphous matrix [7]. The adult human skeleton is composed of 80% cortical bone and 20% trabecular bone, even though different bones and sites within them present different ratios. Cortical bone is dense and solid, forming the outer shell that surrounds the marrow cavity and is composed of concentric structural units known as osteons [8]. In contrast, trabecular bone consists of a honeycomb-like network of plates and rods interspersed throughout the bone marrow compartment [9]. Figure 1.1 presents bone structure and constitution in further detail.

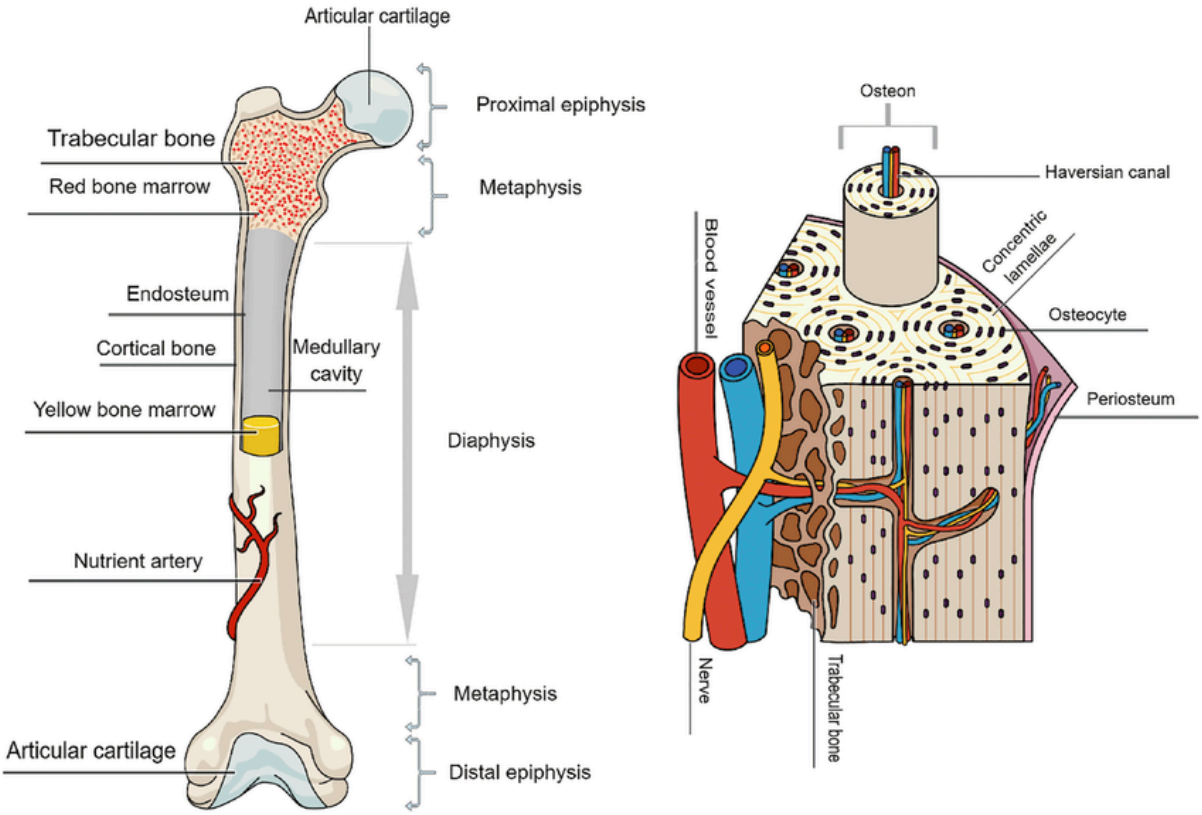


Figure 1.1. Schematic representation of the macro and microstructure of long bone. Reproduced from [10], CC BY 4.0.

After skeletal development during gestation, which occurs either through intramembranous or endochondral ossification, two processes govern bone homeostasis throughout life: bone modeling and

bone remodeling. In both, osteoclasts, osteoblasts, and their precursors play central roles. Bone modeling occurs primarily during childhood, although it can continue throughout life, and aims to increase bone mass and shape bone. The main trigger for osteoblast activation and bone formation is local tissue strain. Conversely, in low-strain conditions, resorptive modeling via osteoclasts predominates [11]. Bone remodeling, on the other hand, is a continuous process involving sequential osteoclast-mediated bone resorption followed by osteoblast-mediated bone formation at the same location. Remodeling can be targeted and initiated by local signaling events, such as microdamage or osteocyte apoptosis, that direct osteoclast activity. These signals may also include high mineralization or alterations in collagen cross-linking. Alternatively, stochastic remodeling occurs randomly, without a specific spatial signal, and is thought to contribute mainly to calcium homeostasis. Targeted remodeling, by contrast, plays a key role in repairing mechanically compromised bone matrix [12].

Osteoclasts are multinucleated cells originating from hematopoietic stem cells (HSCs) [7]. Derived from myeloid precursors, these cells are long-lived, constantly renewed by circulating precursors, and capable of recycling through fission into osteomorphs and fusion back into osteoclasts [13]. Although previously believed to be terminally differentiated cells and to undergo apoptosis after around 2 weeks, recent studies show that osteoclasts may persist for up to 6 months [14, 15]. Dysregulation of osteoclast function may lead to pathological increase or decrease in bone mass, depending on whether cell activity or development is up or downregulated [16]. Additionally, osteoclasts influence other physiological processes, including hematopoiesis, stem cell mobilization, and specific immune functions [17]. The skeletal lineage cells responsible for osteogenesis go through three differentiation stages: osteoprogenitor, preosteoblasts, and osteoblasts [18]. These cells originate from mesenchymal stem cells (MSCs) [7] and are responsible for synthesizing osteoid, an organic portion of the extracellular matrix (ECM) primarily composed of type I collagen and glycosaminoglycans (GAGs). Upon mineralization, the osteoid transforms into bone matrix composed of both organic and inorganic portions. The inorganic portion consists mainly of calcium hydroxyapatite (HA), which provides bone with its rigidity and mechanical strength [19, 20]. Following matrix deposition, osteoblasts may follow one of three fates. They can undergo apoptosis, a normal aspect of bone homeostasis [12]; they can differentiate into osteocytes, becoming embedded in the mineralized bone matrix and losing most of their cytoplasmic organelles. Osteocytes are the most abundant cell type in mature bone and serve as mechanosensory regulators of bone mass by detecting strain and secreting signaling molecules such as sclerostin (SOST), which inhibits osteoblast activity. Alternatively, osteoblasts can become quiescent bone lining cells (BLCs) that remain on the bone surface but can be reactivated to resume bone formation [21].

Bone metabolism is a complex and dynamic process, and its scientific comprehension is still evolving. Table 1.1 summarizes some of the most relevant endogenous signaling molecules involved in bone regulation. Notably, several of these molecules are also applied exogenously in clinical and experimental settings, a topic that will be discussed in later sections.

Table 1.1. Some of the most important signaling molecules involved in bone metabolism. Information compiled from [7].

Molecule	Secreted by	Type	Main role in bone metabolism
Monocyte/macrophage colony-stimulating factor (M-CSF)	Osteoblasts and Osteocytes	Cytokine	Stimulates survival, proliferation, and differentiation of osteoclast precursors
Receptor activation of NF-κB ligand (RANKL)			Promotes osteoclast differentiation and activation via RANK-RANKL signaling
Osteoprotegerin (OPG)		Glycoprotein	Binds RANKL, preventing its interaction with RANK and inhibiting osteoclastogenesis
Semaphorin 3A (SEMA3A)			Inhibits osteoclastogenesis; promotes osteoblast activity
Wnt gene family 5A (WNT5A)			Non-canonical Wnt signaling; regulates osteoblast differentiation
Wnt gene family 16 (WNT16)			Protects against cortical bone loss
Sclerostin (SOST)	Osteocytes		Inhibition of osteoblast differentiation
Bone morphogenetic protein 6 (BMP6)	Osteoclasts		Differentiation and functions of osteoblasts and osteocytes
Collagen triple helix repeat containing 1 (CTHRC1)			
EphrinB2 (EFNB2)			
Wnt gene family 10B (WNT10B)			
Semaphorin 4D (SEMA4D)			
Cardiotrophin-1 (CT-1)			
Platelet-derived growth factor-BB (PDGF-BB)			
Sphingosine 1-phosphate (S1P)		Sphingolipid	

1.3. Bone disease

Globally, from the 1990s to 2019, there were approximately 178 million new fractures (an increase of 33.4%), 455 million cases of either acute or long-term symptoms of a fracture (a 70.1% increase), and 25.8 million years lived with disability (YLD) (an increase of 65.3%) [22].

Bone diseases affect the lives of millions of people worldwide. Among them, the most prevalent is osteoporosis, a degenerative condition that affects the entire skeletal system. It is characterized by a decrease in bone mineral density, leading to deterioration of the tissue's microstructure and resulting in low bone mass [23]. This makes bones fragile, increasing the risk of fracture and contributing to reduced quality of life, limiting an individual's autonomy due to disability, and decreased life expectancy [24]. It is a multifactorial disease influenced by age, sex, ethnicity, race, heredity, lifestyle, and dietary habits. Post-menopausal women are at particularly high risk. At age 60, 10% of women are estimated to be affected; this prevalence rises to 20%, 40%, and nearly 66% for each of the following decades of life [25]. Osteopenia refers to a similar condition in which bone mineral density is lower than normal, but not low enough to meet the criteria for osteoporosis [26].

Bone tumors are also associated with high morbidity and mortality [27]. Osteosarcoma, the most common primary bone malignancy, arises from bone-forming cells such as preosteoblasts and osteoblasts [28]. As radiotherapy is generally ineffective, treatment typically includes both neoadjuvant (preoperative) and adjuvant (postoperative) chemotherapy. The neoadjuvant phase aims to induce tumor necrosis, reduce the size of the primary tumor, and decrease the number and size of pulmonary metastases (present in up to 20% of cases) [29]. This is followed by surgical resection and adjuvant chemotherapy [30], which, even if successful, leaves structural defects that may require long-term therapy and reconstruction. Cancer statistics for 2025 [31] estimate an approximate 42% survival rate for bone and joint cancer, with a high portion of these patients likely in need of new therapies that can help them have a full recovery.

A wide range of bone diseases is influenced or aggravated by lifestyle factors such as dietary deficiencies (e. g., in calcium or vitamin D) or physical inactivity and overexertion [32]. Many are physiologically associated with dysregulated osteoclast activity. For instance, osteoporosis, osteopetrosis (characterized by increased bone mass due to impaired bone resorption [33]), rheumatoid arthritis, bone metastases, and periodontitis (chronic gum inflammation associated with alveolar bone loss and even jaw osteoporosis [34]) are all linked to altered osteoclast function. Denosumab, an FDA-approved monoclonal antibody against human RANKL, is used in an anti-resorptive therapy that inhibits the RANKL-

RANK interaction. However, in some pathological conditions such as inflammatory arthritis, RANKL-independent osteoclastogenesis has also been observed [17].

1.4. Tissue engineering approaches for bone regeneration

As explored in the previous section, whether they result from trauma, infection, tumors, or genetic disorders, bone defects are among the most common clinical conditions. Evidence of bone grafting has been found in skeletal remains from antiquity. Since then, from xenografts and allografts to autografts, bone remains the second most commonly transplanted tissue, only behind the cornea [35], with an estimated 2 million procedures performed worldwide each year [36]. These grafts, along with prosthetic surgery, fracture fixation, and reoperation, constitute the four most common surgical treatments for bone defect repair. Other techniques, such as osteotomy (bone cutting for realignment) and debridement (removal of dead or damaged bone), are also performed, although less frequently [37]. Given the limitations and invasiveness of these procedures, there is a growing demand for therapies that do not require tissue excision and that improve biocompatibility and healing outcomes. TE addresses this demand by seeding cell cultures *in vitro* onto scaffolds, which serve as temporary templates that support cell adhesion, proliferation, and differentiation, ultimately promoting new tissue formation. This is often achieved by mimicking the structure and composition of the ECM, enhancing cell-ECM communication and accelerating tissue remodeling [38]. Although TE strategies can involve multiple elements, the central component is usually the scaffold. The ability of cells to attach, proliferate, and differentiate depends strongly on the scaffold's porosity. Porous networks allow for cellular ingrowth, vascularization, and nutrient diffusion. Scaffolds must also be biocompatible, non-toxic, and non-immunogenic. Biodegradability is essential, enabling the gradual replacement of the scaffold by native tissue. Ideally, the degradation rate should match the rate of new tissue mineralization, and the scaffold should possess mechanical properties similar to bone to avoid stress shielding, a common complication in hip prosthesis caused by mismatched mechanical loads between bone and implant [39].

Materials and fabrication methods used for scaffold development vary widely. Materials are generally divided into organic (including natural and synthetic biodegradable polymers) or inorganic. Natural polymers such as gelatin, alginate, collagen, and hyaluronic acid are often used to produce hydrogels. Synthetic polymers like polyethylene glycol (PEG), polyvinyl alcohol (PVA), or poly(N-isopropylacrylamide) (PNIPAm) can also form hydrogels [40]. Other synthetic polymers, such as poly(*L*-lactic acid) (PLLA), polylactic-*co*-glycolic acid (PLGA), and polycaprolactone (PCL), are commonly used in scaffold fabrication through various methods [41]. Inorganic materials include metals (such as stainless steel) and ceramics

such as HA, bioactive glass (mainly composed of silicon dioxide (SiO_2), calcium oxide (CaO), sodium oxide (Na_2O), phosphorus pentoxide (P_2O_5)), and zirconia [42, 43]. Although scaffolds are predominantly 3D structures, they can also take the form of or incorporate 2D components. Electrospun fibers and thin films (often produced by doctor blading or solvent casting), are particularly interesting when composed of piezoelectric materials, as they promote bone cell proliferation and differentiation [44]. Today, scaffold fabrication frequently involves advanced 3D printing techniques [45], while conventional methods like solvent casting, particulate leaching (salt/sugar particle removal), and freeze-drying remain relevant for producing highly porous networks [46, 47].

As previously mentioned, bone TE strategies commonly combine structural and functional components. Hydrogels are especially suitable for incorporating bioactive agents such as pharmaceutical drugs or nanoparticles (NPs), taking advantage of their tunable degradation to allow controlled release and enhanced regenerative outcomes [48].

Among the most widely used additives are growth factors, with bone morphogenetic protein-2 (BMP-2) being one of the most prominent. Part of the transforming growth factor-β (TGF-β) family, it promotes both osteogenesis and angiogenesis at the defect site. BMP-4 and BMP-7 have also received attention from researchers [49]. Vascular endothelial growth factor (VEGF) stimulates angiogenesis and contributes to osteogenesis by promoting the differentiation of MSCs into osteoblasts and inhibiting adipogenic differentiation, thus playing a critical role in bone homeostasis [50]. Fibroblast growth factor 2 (FGF-2) supports osteoblast proliferation, angiogenesis, and intracellular signaling in bone progenitors. Its effect is concentration-dependent: high doses may inhibit bone formation, whereas low doses are stimulatory [51]. Insulin-like growth factor 1 (IGF-1), released by osteoclasts during bone resorption, stimulates embryonic cell differentiation and promotes osteoblast growth and proliferation [52]. Stromal-derived factor (SDF-1) plays a vital role in stem cell recruitment and migration during early bone repair, resulting in increased MSC population at the regeneration site [53]. An example of a multi-component strategy is the work by Kempen *et al.* [49, 54], who incorporated BMP-2 in different combinations of gelatin hydrogel, PLGA microspheres, and a poly(propylene fumarate) (PPF) scaffold, significantly enhancing bone formation. Some of the materials and assembly strategies for tissue-engineered scaffolds, as well as additional biological components, will be further discussed in the following sections.

1.5. Multifunctional, responsive and electroactive materials

Responsive materials, often referred to as smart materials, exhibit changes in their properties in response to environmental stimuli. In the biomedical field, controlling or exploiting a material's responsiveness to such stimuli improves its effectiveness, for example, by enabling the targeted release of active agents at specific zones. Stimuli can be either external or internal. External stimuli include temperature changes, ultraviolet (UV) light, near-infrared (NIR) radiation, magnetic fields, or ultrasound (US). Internally, materials may respond to variations in pH, redox conditions, reactive oxygen species (ROS), glucose, adenosine triphosphate (ATP), or hypoxia, and may also interact with specific enzymes [55]. Due to this versatility, responsive materials have found applications across multiple biomedical domains, including drug delivery, regenerative medicine, diagnostics, and TE.

Polymers are macromolecules composed of repeating units, referred to as monomers, covalently bonded to form long chains. Depending on the type and distribution of monomers, polymers display different physical, chemical, electrical, and thermal properties, such as flexibility, shapeability, reversibility, chemical stability, and biocompatibility. This tunability has enabled their use in a wide range of applications, including robotics, batteries, sensors, 3D printing, and semiconductors [56-58].

External stimuli such as chemical, electrical, optical, or thermal inputs can induce physical changes in certain polymers. Among these, electroactive polymers (EAPs) are of particular interest. This kind of polymer undergoes physical deformation in response to an applied electrical potential and returns to its original shape when the stimulus is removed. Two main types of EAPs exist: ionic and electronic. Both owe their electromechanical properties to charge delocalization: through ion movement in ionic EAPs, and via electron mobility in electronic EAPs [59].

1.5.1. Piezoelectric materials

Piezoelectric materials are a particular class of EAPs. Not only do they present a mechanical deformation in response to an electrical polarization, but the reverse is also observable: when mechanical stress or deformation is applied, an electrical potential is generated [60]. This phenomenon, known as the piezoelectric effect, was first described in 1880 by Pierre and Jacques Curie and was initially observed in substances such as quartz [61]. The term comes from the Greek word *piezein*, which refers to the action of exerting pressure [62]. The direct piezoelectric effect is the ability to convert mechanical stimuli into an electrical potential variation. Conversely, the indirect or converse piezoelectric effect involves

mechanical deformation as a consequence of an applied electrical field. The relationship between mechanical and electrical stimuli is generally linear and reversible [63].

At the molecular level, in the resting state, the centers of mass of negative and positive charges within each unit cell coincide, resulting in an electrically neutral state (Figure 1a)). When an external force is applied and deformation occurs, these charge centers are displaced, creating dipoles (Figure 1b)). Dipoles with opposing orientations cancel out internally, and fixed charges appear at the surface, thereby polarizing the material [64].

The piezoelectric behavior of a material is often described by its piezoelectric charge constant (usually expressed in $pC.N^{-1}$). Table 1.2 presents examples of differently processed natural and synthetic piezoelectric materials and corresponding piezoelectric coefficients as reported in the literature.

Table 1.2. Representative examples of natural and synthetic piezoelectric materials, processed morphology, and corresponding piezoelectric coefficients.

	Piezoelectric material	**Structure morphology**	**Piezoelectric coefficient ($pC.N^{-1}$)**	**Ref.**
Natural Polymers	Cellulose	Nanofiber films	≈ 7-8	[65]
	Chitosan	Films	≈ 4-6	[65]
	Collagen	Films	0.122 (d_{14})	[66]
	Fibroin	Electrospun membranes	38 ± 2 (d_{33})	[67]
	Diphenylalanine	Self-assembled peptide nanotubes	60 (d_{15})	[68]
Synthetic Polymers	PVDF	Polarized films	24 – 34 (d_{33}) 8 – 22 (d_{31}) depending on β phase %	[63]
	P(VDF-TrFE)	Polarized films	28 (d_{33})	[69]
	Polyamide 11 (PA11)	Films	2.73	[70]
	PLLA	Films	16	[71]
	Poly(3-hydroxybutyrate-*co*-3-hydroxyvalerate) (PHBV) (12% valerate fraction)	Electrospun fibers	0.605 ± 0.09	[72]
Piezoceramics	Li-doped barium titanate ($BaTiO_3$)	Nanoparticles	260 (d_{33})	[73]
	Potassium sodium niobate (KNN)	Die-pressed powder into discs	≈ 93 (d_{33})	[74]
	Zinc oxide (ZnO)	ZnO/TiO_2 composite coating	3.73 – 4.87 (d_{33})	[75]

The effect of piezoelectricity on bone cells will be further discussed in the next section. However, as a contextual example, it has been shown that cell proliferation is influenced not only by the electrical stimuli provided by the material, but also by its surface properties. Electrospun PLLA mats, for instance, have demonstrated support for both osteoblast and fibroblast proliferation. Interestingly, fiber roughness was found to favor fibroblast growth, while osteoblast proliferation was reduced [76]. This suggests that scaffold topography and surface features, in addition to electrical responsiveness, play a key role in regulating cell-specific behavior. As such, careful consideration of all scaffold characteristics is vital when designing materials for tissue regeneration.

1.5.2. Nanomaterials

The history of NPs dates back further than the scientific understanding of the time could explain and identify. Famously, Lycurgus Cup, a Roman artifact from the 4th century is made from dichroic glass, appearing green when illuminated from the outside and red when illuminated from the opposite side; in other words, when light is reflected or transmitted, respectively. This optical phenomenon is due to gold and silver NPs embedded in the glass matrix [77]. More recently, in the 1950s and 1960s, NPs started being studied for drug transport and release, as well as vaccine development [78]. Their reduced size (typically up to 100 nm when strictly considering the nanoscale, though this classification is sometimes applied more broadly) is especially advantageous when targeting eukaryotic cells, whose dimensions generally range from 10 to 100 μm in diameter [79]. This size compatibility facilitates cellular uptake, particularly in intracellular drug delivery. Furthermore, their high surface area to volume ratio allows for strong interaction with the surrounding biological environment and other compounds present within [80]. NP applications are not limited to biomedicine. In civil engineering, SiO_2 NPs have been incorporated into concrete [81] to enhance mechanical properties, while in architecture, TiO_2 (titanium dioxide) is used in window coatings to promote photocatalytic self-cleaning by decomposing biofilm [82]. A wide range of materials can be used for NP synthesis, including both natural and synthetic polymers. Among natural polymers, alginate (extracted from algae) and chitosan (from crustacean exoskeleton) are frequently employed [83, 84]. These biopolymers can be used alone or combined to enhance yield and bioadhesive properties, and can encapsulate not only pharmaceutical drugs but also peptides and proteins. However, drug leaching during formulation can compromise retention efficiency [85].

Dextran, a natural analogue of PEG, is also widely used in biomedical applications due to its excellent biocompatibility and water solubility [86]. Regarding synthetic polymers, polyacrylic acid (PAA) has been combined with polyacrylamide (PAM) to generate NPs with tunable surface charge by changing the ratio

in which these polymers are present. The tuning of the surface charge allows the particles to cross physiological barriers such as the mucous membrane [87].PLGA is one of the most used synthetic polymers in the synthesis of polymeric NPs for pharmaceutics encapsulation, largely due to its excellent biodegradability and biocompatibility. Upon hydrolysis, it breaks down into lactic and glycolic acid, endogenous monomers that are metabolized by the human organism, ensuring minimal systemic toxicity [88]. PLGA has been used to encapsulate growth factors that promote cell proliferation and differentiation in bone regeneration [89]. Moreover, the piezoelectric effect has been harnessed in NP-based systems. Polyvinylidene fluoride (PVDF) NPs have demonstrated the ability to promote pre-osteoblast adhesion when incorporated into scaffolds [90].

Different methods can be employed in NP synthesis. In electrospray, a high voltage electrical field is applied to a polymeric solution, typically fed through a syringe with a metallic needle by a pump. As the solvent evaporates, a fine jet is created. By adjusting parameters such as the intensity of the electrical field, solution concentration, flow rate, and distance to the collector, it is possible to tune the production of either microspheres or fibers (in which case the technique is called electrospinning) [91]. Alternative methods for microsphere preparation may be more appropriate for different polymers or other aspects such as yield rates. One of these is microemulsions, thermodynamically stable dispersions of two immiscible fluids stabilized by surfactant molecules at their interface. These systems are typically categorized as water-in-oil (W/O), oil-in-water (O/W), or water-in-supercritical CO_2 [92]. Microfluidic devices may also be used for microsphere synthesis and are set on similar principles, using a polymer solution as the dispersed phase and breaking it into periodic droplets using immiscible continuous-phase streams. The resulting microspheres can be precisely controlled by adjusting polymer concentrations, flow rates, and channel dimensions [93]. These devices can be constructed by fabricating a mold for the channels using techniques such as photolithography or 3D printing (depending on the necessary scale), followed by pouring PDMS solution, which is then cured and sealed to achieve the final system [94].

Magnetic nanoparticles (MNPs) can exhibit different compositions, including pure metals (like Fe or Co), noble metals (Ag, Au), iron oxides, and different metallic alloys (FeCo, Au-Fe_3O_4). Some of these materials may present cytotoxicity, which can be mitigated through surface modification using polymers such as PEG or PVA. These coatings help to improve biocompatibility and reduce opsonization (the immune process by which foreign bodies are tagged for removal by phagocytes [95]). Materials such as silica can also be used to enhance dispersibility and colloidal stability in aqueous solution [96]. Among all the magnetic properties that MNPs can possess, superparamagnetism is especially attractive for biomedical applications. It is characterized by the presence of a single magnetic domain, allowing the

NPs to be guided by an external applied magnetic field. Superparamagnetism is typically observed in MNPs in the range of 10 to 20 nm [95], and it arises when the particle size is above a critical threshold, dependent on material type and temperature. This property manifests above the so-called blocking temperature (T_B), below which the magnetic moment becomes "locked", and disappears above the Curie temperature (T_C), at which the magnetic order is lost. Notably, once the external magnetic field is removed, the residual magnetization of a superparamagnetic NP is negligible or absent. Hence, these particles exhibit no magnetic hysteresis, meaning they do not require an opposite field to demagnetize [97]. In addition to size, the shape of the MNPs also influences their saturation magnetization (M_S), which represents the maximum magnetization achievable under an external magnetic field. Generally, smaller particles have lower M_s values, although heating efficiency (under alternating magnetic fields) tends to increase with decreasing particle size [98]. When subjected to an alternating magnetic field (AMF), MNPs generate heat proportional to the field's amplitude and frequency. This phenomenon is exploited in magnetic hyperthermia, a therapeutic strategy that aims to target and destroy localized tumoral tissue via controlled heating [99].

Owing to their biocompatibility, magnetic properties, price, and colloidal stability, iron oxides have received much attention from researchers. Two of the most studied forms are magnetite (Fe_3O_4) and maghemite (γ-Fe_2O_3), both naturally occurring minerals with spinel-like crystal structures. Among them, magnetite exhibits the highest saturation magnetization at room temperature (RT) (reported up to 98 $emu.g^{-1}$, though this value can vary significantly depending on particle size, synthesis method, and oxidation susceptibility [100]. Because of this, magnetite-based MNPs are the most commonly used in biomedical applications, including imaging, drug delivery, and hyperthermia.

1.5.3. Magnetoelectric effect

MNPs can present the magnetostrictive effect, where mechanical deformation takes place when subjected to a magnetic field. When these magnetostrictive components are integrated into a piezoelectric matrix, the mechanical strain is transferred to the piezoelectric phase, which in turn converts the mechanical input into an electric signal. This coupling of magnetostriction and piezoelectricity is known as the magnetoelectric (ME) effect. Composites possessing this property, such as MNPs coated with piezoelectric polymers, can convert magnetic field energy into localized electrical stimuli, generating surface charge variation capable of promoting bone tissue regeneration and other bioelectrical effects [101]. This phenomenon is illustrated in Figure 1.2.

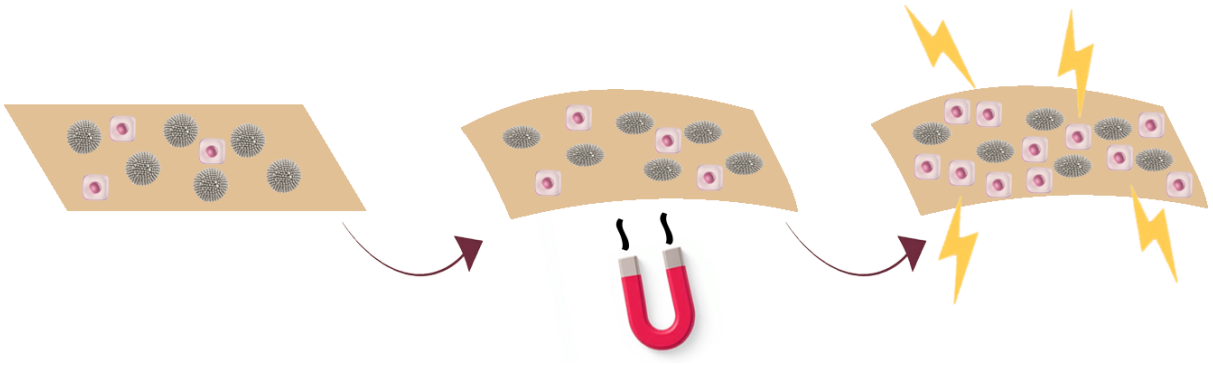


Figure 1.2. Schematic representation of the magnetoelectric effect in a composite scaffold seeded with cells. Upon application of a magnetic field, the magnetostrictive nanoparticles deform, inducing mechanical strain in the piezoelectric matrix. This deformation generates a localized electrical output, which can promote enhanced cell activity and proliferation.

Historically, 2D structures possessing the ME effect have been widely explored. Several studies have investigated the incorporation of different ferrite NPs, including $CoFe_2O_4$, $NiFe_2O_4$, and $Ni_{0.5}Zn_{0.5}Fe_2O_4$, into PVDF matrices to assess their influence on the nucleation and stabilization of the polymer's β-phase, the piezoelectric crystalline conformation essential for ME applications [102]. Similar studies have used $Zn_{0.2}Mn_{0.8}Fe_2O_4$ and Fe_3O_4 incorporated into the copolymer poly(vinylidene fluoride-*co*-trifluoroethylene) (P(VDF-TrFE)) to enhance piezoelectric and magnetoelectric performance [103]. Another example involves the combination of Terfenol-D ($Tb_xDy_{1-x}Fe_2$), a giant magnetostrictive material, with this same copolymer, which led to a ≈25% increase in MC3T3-E1 pre-osteoblast cell proliferation under magnetic stimulation [104]. With the aim of providing a more suitable microenvironment for cells to grow, and in the case of bone mimicking its porous structure, 3D scaffolds have gained more attention from researchers, even more so with the advent of 3D printing. Mushtaq *et al.* [105] designed a PLLA scaffold incorporating $CoFe_2O_4$@$BiFeO_3$ (bismuth (III) ferrite, itself also piezoelectric), using gelatin spheres as porogens. The spheres were dissolved post-fabrication to yield an interconnected, highly porous scaffold. This way, under magnetic stimulation, these 3D scaffolds showed a 134% increase in MG63 cell proliferation in comparison to non-stimulated ones. In contrast, their 2D membrane counterparts showed an increase of 43%, highlighting the added benefit of a 3D architecture. Other 3D magnetoelectric composites have been fabricated by casting PVDF/$CoFe_2O_4$ solutions into petri dishes containing layered and porous nylon meshes (≈ 100 μm pores). These structures also promoted preosteoblast proliferation under stimulation, confirming the biological relevance of ME scaffolds for TE applications [101].

1.6. Hydrogels

Hydrogels are commonly described as 3D, swellable polymer networks capable of absorbing a considerable amount of aqueous fluid. This ability is due to the hydrophilicity of the polymer backbone. Concurrently, crosslinking between polymer chains provides structural integrity and resistance to dissolution in aqueous environments [106]. Hydrogels also exhibit excellent biocompatibility due to their high water content and low surface tension, making them ideal candidates for a wide range of biomedical applications. Additionally, they have shown potential in energy storage and conversion systems. They can be classified based on various criteria, including their source (natural, synthetic, or composite), method of preparation (e. g., solution casting, free radical polymerization, among others), crosslinking mechanism (physical or chemical), ionic charge, and the type of stimuli to which they respond [107]. Recent studies have also focused on hydrogels as platforms able to simulate the tumor microenvironment. These materials can be engineered to modulate physical, chemical, and biological factors, including ECM composition, matrix remodeling dynamics, oxygen tension, pH, cytokine gradients, and mechanical stiffness [108].

Several natural polymers have been explored for developing hydrogels. For example, collagen, a major ECM protein, provides structural framework for cell growth and adhesion. However, it presents some disadvantages such as low mechanical strength and batch-to-batch variability [109]. These limitations can be addressed by using different crosslinking methods or by creating composite formulations [110]. In comparison, fibrin-based hydrogels possess specific binding domains that include integrin, heparin, and fibronectin, which have important roles in wound healing and tissue regeneration, and they allow a wider tunability of matrix mechanical properties [111]. Semi-synthetic hydrogels, derived from chemically modified natural polymers, have been developed to overcome some of the drawbacks frequently found in natural hydrogels. For instance, chitosan and hyaluronic acid have been chemically modified to adjust degradation profiles and mechanical behavior. Blending such modified polymers at different ratios has been shown to support cell adhesion and tailor functional responses [112].

Crosslinking plays a key role in hydrogel design by enhancing stability, mechanical strength, and functionality. Crosslinking approaches are generally divided into physical (e.g., ionic interactions, hydrogen bonding, crystallization) or chemical (e.g., covalent bonding via crosslinking agents) methods. However, the presence of unreacted chemical crosslinkers may raise concerns regarding cytotoxicity [113, 114]. Table 1.3 provides an overview of commonly used hydrogel crosslinking methods organized according to type and some corresponding examples.

Table 1.3. Classification of hydrogel crosslinking strategies according to physical and chemical methods, including representative techniques and examples for each category. Information compiled from [115].

Method			Examples
Physical Crosslinking	**Ionic/electrostatic Interactions** Opposite charged macromolecules interact with each other to yield polyelectrolyte complexes		Alginate crosslinked with divalent cations, such as Ca^{2+}, Ba^{2+} and Mg^{2+}
			Michael addition and ionic interaction between maleilated chitosan and thiol derivatized sodium alginate
			Formation of polyelectrolyte complexes between chitosan and polymers like polylactic acid (PLA), polyphosphoric acid (PPA) and PAA
	Hydrophobic Interactions	**Thermal induction based on Lower or Upper Critical Solution Temperature** Hydrogels thermally treated at a critical temperature for sol–gel phase transition	Amphiphilic copolymers combining hydrophilic poly(ethylene oxide) (PEO) with hydrophobic polypropylene glycol (PPG) or poly(glycolic acid) (PGA), PLA and PCL
			Methylcellulose with $CaCl_2$ and Na_2HPO_4 salts modify gelation temperature
		Ultrasonic induction Sol-gel transition driven by crosslinked β-sheet crystals promoted by ultrasound	Formation of β-sheet crystals in silk fibroin
	Crystallization Crystallites of polymer chains act as physically crosslinking sites in the network		PVA/sodium alginate fabricated by freeze-thawing technique
			PVA and a hydrophobically associated PAM by one-pot *in situ* polymerization and subsequent freeze-thawing cycling
	Hydrogen bonding Formed among themselves or by interaction with an electron donor groups		Poly(N-acryloyl glycinamide) (PNAGA) containing glycinamide-conjugated monomer with dual-amide in one side group able to reconstruct and amplify hydrogen bonding interactions between amino acid (AA) residues
	Metal coordination Metal–ligand interaction between metal ions and functional groups in polymer chains		Side-chain bipyridyl-functionalized poly(2-oxazoline)s crosslinked with Fe(II), Ru(II), Ni(II) or Co(III)
			Swelling of poly(acrylamide-*co*-acrylic acid) film in $FeCl_3$ aqueous solution

Table 1.3. (cont.) Classification of hydrogel crosslinking strategies according to physical and chemical methods, including representative techniques and examples for each category. Information compiled from [115].

Physical crosslinking		**Host-guest interactions** Molecule with a large cavity volume (host) non-covalently interacts with complementary-shaped molecule (guest)	PEG complexed with α-cyclodextrin
Chemical crosslinking		**Photopolymerization** Highly reactive double bonded carbons in unsaturated groups promote a free radical chain-growth polymerization when exposed to photo irradiation	Methacrylated γ-PGA via UV crosslinking between γ-PGA and glycidyl methacrylate
			Visible-light-mediated thiol–ene hydrogel using eosin-Y as photo-initiator
		Enzyme-catalyzed reactions Enzymes promote covalent bonding	Transglutaminase with calcium ions as cofactors
			Collagen conjugated with tyramine in the presence of horseradish peroxidase and H_2O_2
	Click chemistry	**Diels–Alder reaction** Cycloaddition between a diene and a dienophile	Furan, furan derivatives or methylfuranes that react with PEG dimaleimide
		Schiff base formation Imine linkage generated between amino and aldehyde groups	Delf-crosslinking between the amino group from acrylamide-modified chitin and dialdehyde group from oxidized alginate
		Oxime crosslink Reaction between an aminooxy/hydroxylamine group and an aldehyde or ketone	Difunctional alkoxyamines added to P(N,N-dimethylacrylamide-*stat*-diacetone acrylamide)
		Michael addition A nucleophile is added across multiple C=C bonds of an activated electrophilic olefin or alkynes	PEG diacrylate and thiolated chitosan, gelatin and heparin
		Dynamic covalent chemistry Reversible covalent bonds	Boronated PEG coupling with plant derived polyphenols such as ellagic acid, epigallocatechin gallate, tannic acid

Other techniques capable of inducing physicochemical changes in polymeric chains can facilitate or enhance subsequent hydrogel crosslinking. For example, gellan gum has been chemically modified by undergoing methacrylation, which improves its characteristics by inducing aqueous solubility, enabling liquid formulation at RT prior to injection, accelerating gelation kinetics, and increasing mechanical robustness [116]. The integration of synthetic piezoelectric polymer microspheres into hydrogels has also been explored for tissue regeneration, with demonstrated efficiency in inducing pre-osteoblast proliferation through the magnetoelectric effect or magneto-mechanical actuation [117, 118].

In both examples, composite NPs of $CoFe_2O_4$ with either PVDF or PLLA were incorporated into methacrylated gellan gum hydrogel, illustrating the versatility of this strategy. Other formulations combining magnetoelectric materials and hydrogels include the use of $CoFe_2O_4$ NPs and the piezoceramic BT, incorporated into electrospun fiber mats and subsequently embedded within collagen-based hydrogels. However, in these studies, the results regarding neuronal cell proliferation were inconclusive or showed no significant enhancement [119]. Alternatively, UV-crosslinked methacrylated gelatin hydrogels containing gold NPs have shown remarkable improvement in bone regeneration, particularly in rabbit calvaria defect models [120]. Gelatin is a widely used biomaterial in hydrogel systems and is often combined with other polymers to tailor parameters such as drug release kinetics, porosity, and biodegradation. The degree of crosslinking of gelatin and hyaluronic acid hydrogels affects the mechanical stability of the hydrogels as well as the release (and stability) of BMP-2. This affected the degree of bone formation (along other types of tissue with varying results) in mice [121].

1.7. 3D printing

3D printing has its roots in the 1980s with the development of the stereolithography (SLA) technique [122], based on the principle of vat photopolymerization. A light source with an appropriate wavelength is directed at the surface of a photopolymer resin deposit, according to a previously created computer-assisted design (CAD) model, solidifying the zone exposed to the light source. The supporting platform then moves to allow the deposition and exposure of subsequent layers. This process is repeated layer-by-layer until completion of the printed object. After, a curing process is often required involving exposure to UV light to improve the mechanical properties of the printed parts [123, 124]. Over the years, many techniques have emerged. Two-photon polymerization (2PP) improved upon SLA, which relies on single-photon absorption. The concurrent absorption of two photons released by an ultrashort pulse beam promotes polymerization in a highly localized area, allowing resolutions lower than 100 nm [123, 125]. In selective laser sintering (SLS), a similar principle is used, but instead of resin, powdered materials are

fused. The laser selectively sinters the powder, forming a solid object layer-by-layer [126]. The scanning speed of the laser affects the material's density: slower scanning speeds allow more energy to be absorbed locally, resulting in denser parts, whereas faster speeds reduce energy input, leading to more porous structures [127]. The composition of the powder used in laser-based printing techniques can vary, including thermoplastic polymers [128], ceramics [129], and metals - particularly in selective laser melting (SLM), which uses high-powered lasers to fully melt the particles [130].

It was only in the mid 2000s and early 2010s that additive manufacturing (AM), an analogous term for 3D printing, started being more commonplace. This was, in part, due to the expiration of the fused deposition modeling (FDM) patent in 2009 [131] and the rise of open-source initiatives like the RepRap project [132], which fostered the development of low-cost, self-replicating 3D printers accessible to the general public and research centers. FDM is an extrusion-based technique where a polymeric filament is inserted into a heated printing head, melted, and extruded onto a build platform. The head and platform move along the *x*, *y*, and *z* axes to create the 3D structure in successive layers [133, 134]. Common filaments include acrylonitrile butadiene styrene (ABS), polycarbonate (PC), polymethylmethacrylate (PMMA), polystyrene (PS), and PLA [20]. Additionally, water soluble filaments such as PVA and butenediol vinyl alcohol (BVOH) are also used as sacrificial support during multi-material printing [131].

Although techniques such as inkjet and laser printing are also employed [135-139], extrusion-based bioprinting remains the most frequently used method. The printing process is similar to FDM, in which the printing material is deposited layer by layer onto a build platform to construct the 3D structure. However, instead of a thermoplastic filament fed through a heated nozzle, the bioink is loaded into a syringe and extruded using a piston, screw, or pneumatic pressure system [140]. The biomaterials used in this technique are typically solutions, pastes, or dispersions, which often (although not necessarily) have the advantage of RT processing and support the incorporation and homogeneous distribution of living cells [141].

Figure 1.3 presents a conceptual extrusion-based 3D printer and illustrates different elements that can be integrated into printed hydrogels.

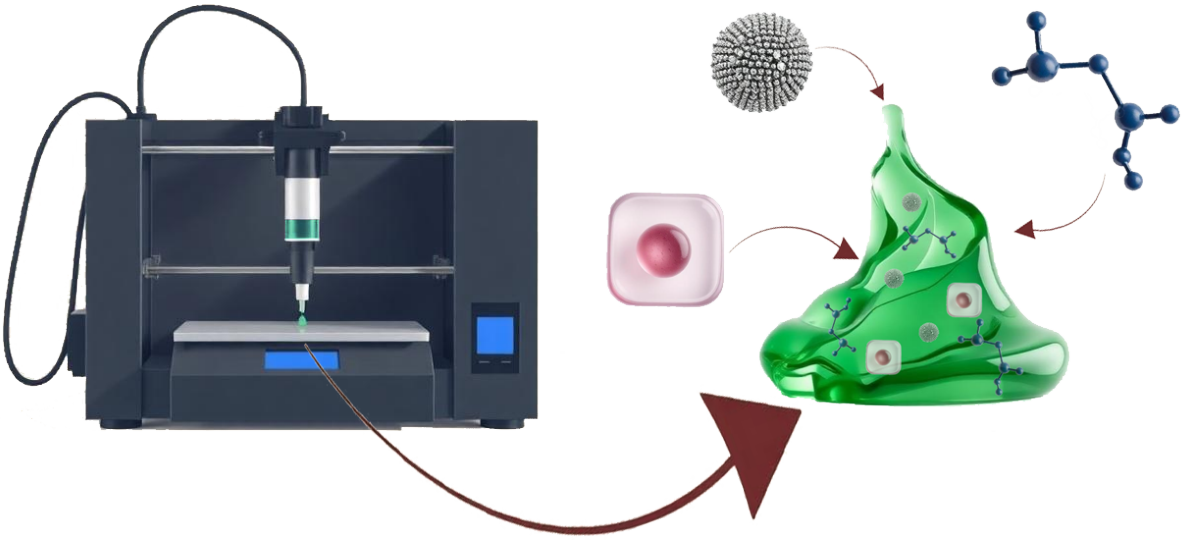


Figure 1.3. Illustration of an extrusion-based 3D printer equipped with a syringe containing a hydrogel with adequate rheological properties for printing. Hydrogels can be loaded with different elements (before or after printing), such as cells, nanoparticles, growth factors, or pharmaceutical compounds.

While conventional 3D printing can make use of the previously mentioned kinds of materials to make prosthesis or proofs of concept, these typically lack biological activity. In contrast, 3D bioprinting refers to 3D structures designed to exhibit or support biological function. Extrusion-based methods akin to the one shown in Figure 1.3 account for more than half of all bioprinting methods reported in SCOPUS records as of early 2024, much owed to their ease of use, chance to use tailored materials and a range of equipment prices with more accessible options [142]. Applications can range from drug screening platforms to implantable tissues or even organ transplantation. Because of their injectability, high water content, biocompatibility, and capacity to create a favorable microenvironment for cell encapsulation, as well as their tunable physical and chemical crosslinking mechanisms, hydrogels are considered the most attractive materials for 3D bioprinting [143]. Both natural and synthetic hydrogels have been widely used in 3D bioprinting for bone regeneration. Natural carbohydrate-based polymers, such as alginate, chitosan, agarose, hyaluronic acid, and dextran, while protein-based polymers comprise gelatin, fibrin, and collagen. Among synthetic polymers, PGA and PLA are frequently used [144]. Bioprinted methacrylated hyaluronic acid (MeHA) hydrogels have also shown the ability to induce osteogenic differentiation of mesenchymal stroma cells even in the absence of osteogenic supplements. This effect was further improved by incorporating BMP-2 into the culture medium [145]. Natural and synthetic composite hydrogels have also been explored. For instance, alginate-PVA-HA composites have shown optimal rheological properties for extrusion-based printing, achieving good shape fidelity. MC3T3-E1 were

embedded in the hydrogel before printing, allowing an optimal distribution of the cells throughout the construct. After crosslinking, cell viability decreased from 95.6% to 77.5%, showing that the crosslinking process may negatively affect encapsulated cells. However, a substantial population of viable cells may remain. Non-optimized control scaffolds presented lower cell viability, around 60%, showing that unoptimized solutions of bioprinted hydrogels containing pre-encapsulated cells may suffer increased stress during the extrusion process [146]. Synthetic hydrogels have also been widely investigated, including more unconventional material combinations. For example, 3D printed PCL/HA scaffolds treated with PEG as a plasticizer showed *in situ* ossification within the scaffold pores. However, these constructs induced an immune response, potentially due to the synthetic components used [147]. More recently, printing of PCL-metal organic framework (MOF) composites has demonstrated enhanced expression of osteogenesis-related genes and proteins, both *in vivo* and *in vitro*, improving the healing of bone defects in rabbit models [148].

These advances highlight the central role of 3D printing and bioprinting technologies in developing biomimetic scaffolds capable of supporting bone regeneration.

1.8. Objectives and methodology

The primary objective of this work was the development of multiresponsive and electroactive scaffolds for bone tissue regeneration including local electroactive response and the possibility of releasing biochemical factors over time. With the aim of developing a multipronged approach able to be built upon, a wide array of materials and types of structures were developed. There systems were evaluated for their ability to support and promote bone cell growth, both individually and in combination, as well as under magnetic stimulation. The core focus of this work lies in the design and fabrication of scaffolds and hydrogels, including hybrid systems that integrate both components. For achieving this goal, the following methodology has been implemented:

1. Development of biodegradable piezoelectric and magnetoelectric scaffolds (pure PHBV and PHBV combined with magnetostrictive Fe_3O_4 NPs) using 3D-printed sacrificial molds;
2. Development of composite magnetic and polymeric microspheres;
3. Development of different gelatin-based hydrogels using various methods of crosslinking to attain different properties and in-solution behaviors;
4. Development of non-crosslinked 3D-printed hydrogel;

5. Manipulation and processing of the hydrogels in the form of films and their loading into the polymeric scaffolds;
6. Thorough characterization of the processed materials in terms of morphology, mechanical, magnetic and overall physicochemical properties;
7. Evaluation of neat and composite scaffolds with and without loaded hydrogel for TE applications using the MC3T3-E1 preosteoblast cell line under magnetic stimuli.

1.9. Thesis structure

This document is divided into five main chapters. **Chapter 1** provides a historical context and a comprehensive literature review covering the scientific foundations relevant to this thesis, as well as the motivation, objectives, and overall structure of the work.

Chapters 2-4 are based on scientific publications either published or under submission and are arranged to progressively detail the preparation of the developed structures, their characterization, and their evaluation as TE platforms. Each chapter, except the final one, presents in-depth state-of-the-art information related to its specific topic.

Chapter 2 describes the fabrication of biodegradable and piezoelectric PHBV 3D scaffolds, produced either as pure polymer structures or as composites containing 10% Fe_3O_4 NPs. The chapter details their fabrication via 3D printing of sacrificial molds, followed by an extensive characterization of scaffold morphology, wettability, mechanical, chemical, and thermal properties. Cytotoxicity, adhesion, and proliferation of MC3T3-E1 preosteoblast were also evaluated.

Chapter 3 focuses on the synthesis of Fe_3O_4@PHBV and $CoFe_2O_4$@PHBV microspheres using an emulsion method, as well as Fe_3O_4@PVDF microspheres produced by electrospray. Different synthesis routes are compared in light of parameters affecting yield and particle quality, and size and magnetic properties characterization are systematically characterized.

Chapter 4 addresses hydrogel development and is divided into **Subchapters 4.1** and **4.2**. Subchapter 4.1 investigates the printability of a gelatin-based hydrogel blended with sericin, a natural protein derived from silk. Morphology, swelling, solubility, rheology, physicochemical properties and cytotoxicity of the hydrogel are characterized. Subchapter 4.2 evaluates different gelatin crosslinking strategies, including UV-induced crosslinking with riboflavin, fructose-mediated Maillard reaction (MR), and 1-Ethyl-3-(3-dimethylaminopropyl)carbodiimide (EDC)-N-Hydroxysuccinimide (NHS) chemical crosslinking. These hydrogels were incorporated into polymeric and composite scaffolds. Hydrogel films crosslinked with riboflavin or fructose were also developed. Optical, mechanical, and physicochemical

characterization was carried, and cytotoxicity was evaluated for all formulations. Additionally, EDC-NHS-crosslinked hydrogel-loaded scaffolds were subjected to adhesion and proliferation studies.

Chapter 5 presents the overall conclusions and outlines perspectives for future work.

References

[1] J. F. Dieffenbach, *Nonnulla de regeneratione et transplantatione: Diss. inaug*. Typis Richterianis, 1822.

[2] U. Meyer, T. Meyer, J. Handschel, and H. P. Wiesmann, *Fundamentals of tissue engineering and regenerative medicine*. Springer, pp. 5, 2009, isbn: 978-3-540-77754-0.

[3] D. P. Orgill and C. Blanco, *Biomaterials for treating skin loss*. Woodhead Publishing, pp. 3, 2009, isbn: 978-1-84569-363-3.

[4] F. Berthiaume, T. Maguire, and M. Yarmush, "Tissue engineering and regenerative medicine: history, progress, and challenges," *Annual review of chemical and biomolecular engineering,* vol. 2, no. 1, pp. 403-430, 2011, doi: https://doi.org/10.1146/annurev-chembioeng-061010-114257.

[5] S. Luo *et al.*, "Advances in electroactive biomaterials: Through the lens of electrical stimulation promoting bone regeneration strategy," *Journal of Orthopaedic Translation,* vol. 47, pp. 191-206, 2024, doi: https://doi.org/10.1016/j.jot.2024.06.009.

[6] S. Manaye *et al.*, "The Role of High-intensity and High-impact Exercises in Improving Bone Health in Postmenopausal Women: A Systematic Review," (in eng), *Cureus,* vol. 15, no. 2, p. e34644, 2023, doi: https://doi.org/10.7759/cureus.34644.

[7] Y. Han, X. You, W. Xing, Z. Zhang, and W. Zou, "Paracrine and endocrine actions of bone—the functions of secretory proteins from osteoblasts, osteocytes, and osteoclasts," *Bone Research,* vol. 6, no. 1, p. 16, 2018, doi: https://doi.org/10.1038/s41413-018-0019-6.

[8] M. Caon, "Skeleton and Joints," in *Examination Questions and Answers in Basic Anatomy and Physiology: 2400 Multiple Choice Questions*. Cham: Springer International Publishing, 2018, pp. 151-171.

[9] B. Clarke, "Normal Bone Anatomy and Physiology," *Clinical Journal of the American Society of Nephrology,* vol. 3, no. Supplement_3, pp. S131-S139, 2008, doi: https://doi.org/10.2215/cjn.04151206.

[10] Z. Yazdanpanah, J. Johnston, D. Cooper, and X. Chen, "3D Bioprinted Scaffolds for Bone Tissue Engineering: State-Of-The-Art and Emerging Technologies," *Frontiers in Bioengineering and Biotechnology,* vol. 10, p. 824156, 2022, doi: https://doi.org/10.3389/fbioe.2022.824156.

[11] Z. Li, D. Betts, G. Kuhn, M. Schirmer, R. Müller, and D. Ruffoni, "Mechanical regulation of bone formation and resorption around implants in a mouse model of osteopenic bone," *Journal of the Royal Society Interface,* vol. 16, no. 152, p. 20180667, 2019, doi: https://doi.org/10.1098/rsif.2018.0667.

[12] M. Allen and D. Burr, "Chapter 5 - Bone Growth, Modeling, and Remodeling," in *Basic and Applied Bone Biology (Second Edition)*, B. Burr and R. Allen Eds.: Academic Press, pp. 85-100, 2019, doi: https://doi.org/10.1016/B978-0-12-813259-3.00005-1.

[13] M. M. McDonald *et al.*, "Osteoclasts recycle via osteomorphs during RANKL-stimulated bone resorption," (in eng), *Cell,* vol. 184, no. 5, pp. 1330-1347.e13, 2021, doi: https://doi.org/10.1016/j.cell.2021.02.002.

[14] S. C. Manolagas, "Birth and death of bone cells: basic regulatory mechanisms and implications for the pathogenesis and treatment of osteoporosis," *Endocrine Reviews,* vol. 21, no. 2, pp. 115-137, 2000, doi: https://doi.org/10.1210/edrv.21.2.0395.

[15] C. E. Jacome-Galarza *et al.*, "Developmental origin, functional maintenance and genetic rescue of osteoclasts," *Nature,* vol. 568, no. 7753, pp. 541-545, 2019, doi: https://doi.org/10.1038/s41586-019-1105-7.

[16] T. Bellido, L. Plotkin, and A. Bruzzaniti, "Chapter 3 - Bone Cells," in *Basic and Applied Bone Biology*, D. Burr and M. Allen Eds., Second Edition ed.: Academic Press, pp. 37-55, 2019, doi: https://doi.org/10.1016/B978-0-12-813259-3.00005-1.

[17] I. Choi, A. Umemoto, M. Mizuno, and K. Park-Min, "Bone metabolism – an underappreciated player," *npj Metabolic Health and Disease,* vol. 2, no. 1, p. 12, 2024, doi: https://doi.org/10.1038/s44324-024-00010-9.

[18] F. Long, "Building strong bones: molecular regulation of the osteoblast lineage," *Nature reviews Molecular cell biology,* vol. 13, no. 1, pp. 27-38, 2012, doi: https://doi.org/10.1038/nrm3254.

[19] R. Setiawati and P. Rahardjo, "Bone development and growth," in *Osteogenesis and bone regeneration*, vol. 10, H. Yang Ed., 2019, doi: https://doi.org/10.5772/intechopen.82452.

[20] Y. Park, E. Cheong, J.-G. Kwak, R. Carpenter, J.-H. Shim, and J. Lee, "Trabecular bone organoid model for studying the regulation of localized bone remodeling," *Science Advances,* vol. 7, no. 4, p. eabd6495, 2021, doi: https://doi.org/10.1126/sciadv.abd6495.

[21] F. G. F. Tresguerres, J. Torres, J. López-Quiles, G. Hernández, J. A. Vega, and I. F. Tresguerres, "The osteocyte: A multifunctional cell within the bone," *Annals of Anatomy - Anatomischer Anzeiger,* vol. 227, p. 151422, 2020, doi: https://doi.org/10.1016/j.aanat.2019.151422.

[22] A.-M. Wu *et al.*, "Global, regional, and national burden of bone fractures in 204 countries and territories, 1990–2019: a systematic analysis from the Global Burden of Disease Study 2019," *The Lancet Healthy Longevity,* vol. 2, no. 9, pp. e580-e592, 2021, doi: https://doi.org/10.1016/S2666-7568(21)00172-0.

[23] Y. Fan *et al.*, "Sex- and Age-Specific Prevalence of Osteopenia and Osteoporosis: Sampling Survey," (in eng), *JMIR Public Health Surveill,* vol. 10, p. e48947, 2024, doi: https://doi.org/10.2196/48947.

[24] N. Chaudhary, D. Sunuwar, M. Sapkota, S. Pant, M. Pradhan, and K. Bhandari, "Prevalence of osteoporosis and associated factors among people aged 50 years and older in the Madhesh province of Nepal: a community-based cross-sectional study," *Journal of Health, Population and Nutrition,* vol. 43, no. 1, p. 100, 2024, doi: https://doi.org/10.1186/s41043-024-00591-7.

[25] M. Lorentzon *et al.*, "Osteoporosis and fractures in women: the burden of disease," *Climacteric,* vol. 25, no. 1, pp. 4-10, 2022, doi: https://doi.org/10.1080/13697137.2021.1951206.

[26] P. L. Xiao *et al.*, "Global, regional prevalence, and risk factors of osteoporosis according to the World Health Organization diagnostic criteria: a systematic review and meta-analysis," *Osteoporosis International,* vol. 33, no. 10, pp. 2137-2153, 2022, doi: https://doi.org/10.1007/s00198-022-06454-3.

[27] A. J. Mutsaers and C. R. Walkley, "Cells of origin in osteosarcoma: Mesenchymal stem cells or osteoblast committed cells?," *Bone,* vol. 62, pp. 56-63, 2014, doi: https://doi.org/10.1016/j.bone.2014.02.003.

[28] A. Abarrategi *et al.*, "Osteosarcoma: Cells-of-Origin, Cancer stem cells, and targeted therapies," *Stem Cells International,* vol. 2016, no. 1, 2016, Art no. 3631764, doi: https://doi.org/10.1155/2016/3631764.

[29] M. E. Anderson, "Update on survival in osteosarcoma," *Orthopedic Clinics,* vol. 47, no. 1, pp. 283-292, 2016, doi: https://doi.org/10.1016/j.ocl.2015.08.022.

[30] N. M. Bernthal *et al.*, "Long-term results (> 25 years) of a randomized, prospective clinical trial evaluating chemotherapy in patients with high-grade, operable osteosarcoma," *Cancer,* vol. 118, no. 23, pp. 5888-5893, 2012, doi: https://doi.org/10.1002/cncr.27651.

[31] R. L. Siegel, T. B. Kratzer, A. N. Giaquinto, H. Sung, and A. Jemal, "Cancer statistics, 2025," (in eng), *CA: A Cancer Journal for Clinicians,* vol. 75, no. 1, pp. 10-45, 2025, doi: https://doi.org/10.3322/caac.21871.

[32] M. Li *et al.*, "Trends and hotspots in research on osteoporosis and nutrition from 2004 to 2024: a bibliometric analysis," *Journal of Health, Population and Nutrition,* vol. 43, 2024, Art no. 204, doi: https://doi.org/10.1101/2024.04.14.24305794.

[33] T. Funck-Brentano, M. C. Zillikens, G. Clunie, H. Siggelkow, N. M. Appelman-Dijkstra, and M. Cohen-Solal, "Osteopetrosis and related osteoclast disorders in adults: A review and knowledge gaps On behalf of the European calcified tissue society and ERN BOND," *European Journal of Medical Genetics,* vol. 69, p. 104936, 2024, doi: https://doi.org/10.1016/j.ejmg.2024.104936.

[34] F. Liu, X. Wang, Y. He, R. Han, T. Wang, and Y. Guo, "Jaw osteoporosis: Challenges to oral health and emerging perspectives of treatment," *Biomedicine & Pharmacotherapy,* vol. 177, p. 116995, 2024, doi: https://doi.org/10.1016/j.biopha.2024.116995.

[35] S. Liu, Y. L. Wong, and A. Walkden, "Current Perspectives on Corneal Transplantation," *Clinical Ophthalmology,* vol. 16, pp. 631-646, 2022, doi: https://doi.org/10.2147/OPTH.S289359.

[36] A. H. Schmidt, "Autologous bone graft: Is it still the gold standard?," *Injury,* vol. 52, pp. S18-S22, 2021, doi: https://doi.org/10.1016/j.injury.2021.01.043.

[37] N. Xue *et al.*, "Bone Tissue Engineering in the Treatment of Bone Defects," (in eng), *Pharmaceuticals (Basel),* vol. 15, no. 7, 2022, doi: https://doi.org/10.3390/ph15070879.

[38] C. Xu *et al.*, "Bone tissue engineering scaffold materials: Fundamentals, advances, and challenges," *Chinese Chemical Letters,* vol. 35, no. 2, p. 109197, 2024, doi: https://doi.org/10.1016/j.cclet.2023.109197.

[39] M. L. Raffa, V. H. Nguyen, P. Hernigou, C. H. Flouzat-Lachaniette, and G. Haiat, "Stress shielding at the bone-implant interface: Influence of surface roughness and of the bone-implant contact ratio," (in eng), *Journal of Orthopaedic Tesearch,* vol. 39, no. 6, pp. 1174-1183, 2021, doi: https://doi.org/10.1002/jor.24840.

[40] J. Maitra and V. K. Shukla, "Cross-linking in hydrogels-a review," *American Journal of Polymer Science,* vol. 4, no. 2, pp. 25-31, 2014, doi: https://doi.org/10.5923/j.ajps.20140402.01.

[41] M. J. Javid-Naderi, J. Behravan, N. Karimi-Hajishohreh, and S. Toosi, "Synthetic polymers as bone engineering scaffold," *Polymers for Advanced Technologies,* vol. 34, no. 7, pp. 2083-2096, 2023, doi: https://doi.org/10.1002/pat.6046.

[42] J. Ni *et al.*, "Three-dimensional printing of metals for biomedical applications," *Materials Today Bio,* vol. 3, p. 100024, 2019, doi: https://doi.org/10.1016/j.mtbio.2019.100024.

[43] W. Weng, W. Wu, M. Hou, T. Liu, T. Wang, and H. Yang, "Review of zirconia-based biomimetic scaffolds for bone tissue engineering," *Journal of Materials Science,* vol. 56, pp. 8309-8333, 2021, doi: https://doi.org/10.1007/s10853-021-05824-2.

[44] C. Ribeiro, V. Sencadas, D. M. Correia, and S. Lanceros-Méndez, "Piezoelectric polymers as biomaterials for tissue engineering applications," *Colloids and Surfaces B: Biointerfaces,* vol. 136, pp. 46-55, 2015, doi: https://doi.org/10.1016/j.colsurfb.2015.08.043.

[45] M. Shahrezaie, A. Zamanian, M. Sahranavard, and M. H. Shahrezaee, "A critical review on the 3D bioprinting in large bone defects regeneration," *Bioprinting,* vol. 37, p. e00327, 2024, doi: https://doi.org/10.1016/j.bprint.2023.e00327.

[46] A. Sola *et al.*, "Development of solvent-casting particulate leaching (SCPL) polymer scaffolds as improved three-dimensional supports to mimic the bone marrow niche," *Materials Science and Engineering: C,* vol. 96, pp. 153-165, 2019, doi: https://doi.org/10.1016/j.msec.2018.10.086.

[47] J. Grenier, H. Duval, F. Barou, P. Lv, B. David, and D. Letourneur, "Mechanisms of pore formation in hydrogel scaffolds textured by freeze-drying," *Acta Biomaterialia,* vol. 94, pp. 195-203, 2019, doi: https://doi.org/10.1016/j.actbio.2019.05.070.

[48] M. Yamamoto, Y. Ikada, and Y. Tabata, "Controlled release of growth factors based on biodegradation of gelatin hydrogel," *Journal of Biomaterials Science, Polymer Edition,* vol. 12, no. 1, pp. 77-88, 2001, doi: https://doi.org/10.1163/156856201744461.

[49] D. H. R. Kempen *et al.*, "Effect of local sequential VEGF and BMP-2 delivery on ectopic and orthotopic bone regeneration," *Biomaterials,* vol. 30, no. 14, pp. 2816-2825, 2009, doi: https://doi.org/10.1016/j.biomaterials.2009.01.031.

[50] J. R. García, A. Y. Clark, and A. J. García, "Integrin-specific hydrogels functionalized with VEGF for vascularization and bone regeneration of critical-size bone defects," *Journal of biomedical materials research Part A,* vol. 104, no. 4, pp. 889-900, 2016, doi: https://doi.org/10.1002/jbm.a.35626.

[51] G. Gronowicz, E. Jacobs, T. Peng, L. Zhu, M. Hurley, and L. T. Kuhn, "Calvarial bone regeneration is enhanced by sequential delivery of FGF-2 and BMP-2 from layer-by-layer coatings with a biomimetic calcium phosphate barrier layer," *Tissue Engineering Part A,* vol. 23, no. 23-24, pp. 1490-1501, 2017, doi: https://doi.org/10.1089/ten.tea.2017.0111.

[52] J. L. Crane and X. Cao, "Function of matrix IGF-1 in coupling bone resorption and formation," *Journal of Molecular Medicine,* vol. 92, pp. 107-115, 2014, doi: https://doi.org/10.1007/s00109-013-1084-3.

[53] T.-M. De Witte, L. E. Fratila-Apachitei, A. A. Zadpoor, and N. A. Peppas, "Bone tissue engineering via growth factor delivery: from scaffolds to complex matrices," *Regenerative Biomaterials,* vol. 5, no. 4, pp. 197-211, 2018, doi: https://doi.org/10.1093/rb/rby013.

[54] D. H. Kempen *et al.*, "Retention of in vitro and in vivo BMP-2 bioactivities in sustained delivery vehicles for bone tissue engineering," *Biomaterials,* vol. 29, no. 22, pp. 3245-3252, 2008, doi: https://doi.org/10.1016/j.biomaterials.2008.04.031.

[55] M. Kalantarmahdavi, A. Salari, Z. Pasdar, and M. R. Amiryousefi, "Edible hyaluronic acid-rich burger separator discs prepared from slaughterhouse waste," *Food Science & Nutrition,* vol. 10, no. 10, pp. 3515-3526, 2022, doi: https://doi.org/10.1002/fsn3.2954.

[56] K. E. Engel, P. A. Kilmartin, and O. Diegel, "Recent advances in the 3D printing of ionic electroactive polymers and core ionomeric materials," *Polymer Chemistry,* vol. 13, no. 4, pp. 456-473, 2022, doi: https://doi.org/10.1039/D1PY01297E.

[57] K. J. Kim and S. Tadokoro, "Electroactive polymers for robotic applications," *Artificial Muscles and Sensors,* vol. 23, p. 291, 2007, doi: https://doi.org/10.1007/978-1-84628-372-7.

[58] A. Saal, T. Hagemann, and U. S. Schubert, "Polymers for battery applications—active materials, membranes, and binders," *Advanced Energy Materials,* vol. 11, no. 43, p. 2001984, 2021, doi: https://doi.org/10.1002/aenm.202001984.

[59] T. Wang *et al.*, "Electroactive polymers for sensing," *Interface focus,* vol. 6, no. 4, p. 20160026, 2016, doi: https://doi.org/10.1098/rsfs.2016.0026.

[60] P.-H. Ducrot, I. Dufour, and C. Ayela, "Optimization of PVDF-TrFE processing conditions for the fabrication of organic MEMS resonators," *Scientific reports,* vol. 6, no. 1, p. 19426, 2016, doi: https://doi.org/10.1038/srep19426.

[61] J. Hlavay and G. Guilbault, "Applications of the piezoelectric crystal detector in analytical chemistry," *Analytical chemistry,* vol. 49, no. 13, pp. 1890-1898, 1977, doi: https://doi.org/10.1021/ac50021a007.

[62] J. A. Harvey, "Smart Materials," in *Handbook of Materials Selection*, pp. 401-418, 2002, doi: https://doi.org/10.1002/9780470172551.ch13.

[63] C. Ribeiro *et al.*, "Electroactive poly(vinylidene fluoride)-based structures for advanced applications," *Nature Protocols,* vol. 13, no. 4, pp. 681-704, 2018, doi: https://doi.org/10.1038/nprot.2017.157.

[64] R. S. Dahiya and M. Valle, *Robotic tactile sensing: technologies and system*. Springer, 2013.

[65] A. Hänninen, E. Sarlin, I. Lyyra, T. Salpavaara, M. Kellomäki, and S. Tuukkanen, "Nanocellulose and chitosan based films as low cost, green piezoelectric materials," *Carbohydrate polymers,* vol. 202, pp. 418-424, 2018, doi: https://doi.org/10.1016/j.carbpol.2018.09.001.

[66] C. C. Silva *et al.*, "Effect of the pH on the piezoelectric properties of collagen films," *Materials Science and Engineering: B,* vol. 83, no. 1, pp. 165-172, 2001, doi: https://doi.org/10.1016/S0921-5107(01)00520-7.

[67] V. Sencadas, C. Garvey, S. Mudie, J. J. K. Kirkensgaard, G. Gouadec, and S. Hauser, "Electroactive properties of electrospun silk fibroin for energy harvesting applications," *Nano Energy,* vol. 66, p. 104106, 2019, doi: https://doi.org/10.1016/j.nanoen.2019.104106.

[68] A. Kholkin, N. Amdursky, I. Bdikin, E. Gazit, and G. Rosenman, "Strong piezoelectricity in bioinspired peptide nanotubes," *ACS nano,* vol. 4, no. 2, pp. 610-614, 2010, doi: https://doi.org/10.1021/nn901327v.

[69] X. Hu, M. You, N. Yi, X. Zhang, and Y. Xiang, "Enhanced piezoelectric coefficient of PVDF-TrFE films via in situ polarization," *Frontiers in Energy Research,* vol. 9, p. 621540, 2021, doi: https://doi.org/10.3389/fenrg.2021.621540.

[70] P. Frubing, A. Kremmer, W. Neumann, R. Gerhard-Multhaupt, and I. L. Guy, "Dielectric relaxation in piezo-, pyro- and ferroelectric polyamide 11," *IEEE Transactions on Dielectrics and Electrical Insulation,* vol. 11, no. 2, pp. 271-279, 2004, doi: https://doi.org/10.1109/TDEI.2004.1285897.

[71] Y. Tajitsu, "Development of environmentally friendly piezoelectric polymer film actuator having multilayer structure," *Japanese Journal of Applied Physics,* vol. 55, no. 4S, p. 04EA07, 2016, doi: https://doi.org/10.7567/JJAP.55.04EA07.

[72] S. N. Gorodzha *et al.*, "A comparison study between electrospun polycaprolactone and piezoelectric poly(3-hydroxybutyrate-co-3-hydroxyvalerate) scaffolds for bone tissue engineering," *Colloids and Surfaces B: Biointerfaces,* vol. 160, pp. 48-59, 2017, doi: https://doi.org/10.1016/j.colsurfb.2017.09.004.

[73] T. Kimura, Q. Dong, S. Yin, T. Hashimoto, A. Sasaki, and T. Sato, "Synthesis and piezoelectric properties of Li-doped BaTiO3 by a solvothermal approach," *Journal of the European Ceramic*

Society, vol. 33, no. 5, pp. 1009-1015, 2013, doi: https://doi.org/10.1016/j.jeurceramsoc.2012.11.007.

[74] W. Chen, Z. Yu, J. Pang, P. Yu, G. Tan, and C. Ning, "Fabrication of biocompatible potassium sodium niobate piezoelectric ceramic as an electroactive implant," *Materials,* vol. 10, no. 4, p. 345, 2017, doi: https://doi.org/10.3390/ma10040345.

[75] S. Pang *et al.*, "Multifunctional ZnO/TiO_2 nanoarray composite coating with antibacterial activity, cytocompatibility and piezoelectricity," *Ceramics International,* vol. 45, no. 10, pp. 12663-12671, 2019, doi: https://doi.org/10.1016/j.ceramint.2019.03.076.

[76] C. Ribeiro, V. Sencadas, A. C. Areias, F. M. Gama, and S. Lanceros-Méndez, "Surface roughness dependent osteoblast and fibroblast response on poly(*l*-lactide) films and electrospun membranes," *Journal of Biomedical Materials Research Part A,* vol. 103, no. 7, pp. 2260-2268, 2015, doi: https://doi.org/10.1002/jbm.a.35367.

[77] M. Krukemeyer, V. Krenn, F. Huebner, W. Wagner, and R. Resch, "History and possible uses of nanomedicine based on nanoparticles and nanotechnological progress," *Journal of Nanomedicine & Nanotechnology,* vol. 6, no. 6, p. 336, 2015, doi: https://doi.org/10.4172/2157-7439.1000336.

[78] J. Kreuter, "Nanoparticles—a historical perspective," *International journal of pharmaceutics,* vol. 331, no. 1, pp. 1-10, 2007, doi: https://doi.org/10.1016/j.ijpharm.2006.10.021.

[79] N. Campbell, *Biology concepts & connections.*, p. 850, 2006, isbn: 9781292401348.

[80] A. Nasir, A. Kausar, and A. Younus, "A review on preparation, properties and applications of polymeric nanoparticle-based materials," *Polymer-Plastics Technology and Engineering,* vol. 54, no. 4, pp. 325-341, 2015, doi: https://doi.org/10.1080/03602559.2014.958780.

[81] G. Li, "Properties of high-volume fly ash concrete incorporating nano-SiO_2," *Cement and Concrete research,* vol. 34, no. 6, pp. 1043-1049, 2004, doi: https://doi.org/10.1016/j.cemconres.2003.11.013.

[82] Y. Paz, Z. Luo, L. Rabenberg, and A. Heller, "Photooxidative self-cleaning transparent titanium dioxide films on glass," *Journal of Materials Research,* vol. 10, no. 11, pp. 2842-2848, 1995, doi: https://doi.org/10.1557/JMR.1995.2842.

[83] I. Kovalenko *et al.*, "A major constituent of brown algae for use in high-capacity Li-ion batteries," *Science,* vol. 334, no. 6052, pp. 75-79, 2011, doi: https://doi.org/10.1126/science.1209150.

[84] A. Anwunobi and M. Emeje, "Recent applications of natural polymers in nanodrug delivery," *Journal of Nanomedicine & Nanotechnoly,* vol. 4, no. 002, 2011, doi: https://doi.org/10.4172/2157-7439.S4-002.

[85] T. A. Ahmed and M. Khalid, "Development of alginate-reinforced chitosan nanoparticles utilizing W/O nanoemulsification/internal crosslinking technique for transdermal delivery of rabeprazole," *Life sciences,* vol. 110, no. 1, pp. 35-43, 2014, doi: https://doi.org/10.1016/j.lfs.2014.06.019.

[86] Y. L. Li *et al.*, "Reversibly stabilized multifunctional dextran nanoparticles efficiently deliver doxorubicin into the nuclei of cancer cells," *Angewandte Chemie,* vol. 121, no. 52, pp. 10098-10102, 2009, doi: https://doi.org/10.1002/anie.200904260.

[87] F. Laffleur, F. Hintzen, G. Shahnaz, D. Rahmat, K. Leithner, and A. Bernkop-Schnürch, "Development and in vitro evaluation of slippery nanoparticles for enhanced diffusion through native mucus," *Nanomedicine,* vol. 9, no. 3, pp. 387-396, 2014, doi: https://doi.org/10.2217/nnm.13.26.

[88] F. Danhier, E. Ansorena, J. M. Silva, R. Coco, A. Le Breton, and V. Préat, "PLGA-based nanoparticles: an overview of biomedical applications," *Journal of controlled release,* vol. 161, no. 2, pp. 505-522, 2012, doi: https://doi.org/10.1016/j.jconrel.2012.01.043.

[89] I. Ortega-Oller, M. Padial-Molina, P. Galindo-Moreno, F. O'Valle, A. B. Jódar-Reyes, and J. M. Peula-García, "Bone Regeneration from PLGA Micro-Nanoparticles," *BioMed Research International,* vol. 2015, p. 18, 2015, Art no. 415289, doi: https://doi.org/10.1155/2015/415289.

[90] D. M. Correia *et al.*, "Electrosprayed poly (vinylidene fluoride) microparticles for tissue engineering applications," *RSC Advances,* vol. 4, no. 62, pp. 33013-33021, 2014, doi: https://doi.org/10.1039/C4RA04581E.

[91] J. Doshi and D. H. Reneker, "Electrospinning process and applications of electrospun fibers," *Journal of Electrostatics,* vol. 35, no. 2, pp. 151-160, 1995, doi: https://doi.org/10.1016/0304-3886(95)00041-8.

[92] T. Aubert *et al.*, "Functional silica nanoparticles synthesized by water-in-oil microemulsion processes," *Journal of Colloid and Interface Science,* vol. 341, no. 2, pp. 201-208, 2010, doi: https://doi.org/10.1016/j.jcis.2009.09.064.

[93] D. N. Breslauer, S. J. Muller, and L. P. Lee, "Generation of Monodisperse Silk Microspheres Prepared with Microfluidics," *Biomacromolecules,* vol. 11, no. 3, pp. 643-647, 2010, doi: https://doi.org/10.1021/bm901209u.

[94] C.-H. Choi, J.-H. Jung, T.-S. Hwang, and C.-S. Lee, "In situ microfluidic synthesis of monodisperse PEG microspheres," *Macromolecular research,* vol. 17, no. 3, pp. 163-167, 2009, doi: https://doi.org/10.1007/bf03218673.

[95] C. C. Berry and A. S. G. Curtis, "Functionalisation of magnetic nanoparticles for applications in biomedicine," *Journal of Physics D: Applied Physics,* vol. 36, no. 13, p. R198, 2003, doi: https://doi.org/10.1088/0022-3727/36/13/203.

[96] N. Tran and T. J. Webster, "Magnetic nanoparticles: biomedical applications and challenges," *Journal of Materials Chemistry,* vol. 20, no. 40, pp. 8760-8767, 2010, doi: https://doi.org/10.1039/C0JM00994F.

[97] A.-H. Lu, E. L. Salabas, and F. Schüth, "Magnetic Nanoparticles: Synthesis, Protection, Functionalization, and Application," *Angewandte Chemie,* vol. 46, no. 8, pp. 1222-1244, 2007, doi: https://doi.org/10.1002/anie.200602866.

[98] A. G. Roca, L. Gutiérrez, H. Gavilán, M. E. Fortes Brollo, S. Veintemillas-Verdaguer, and M. d. P. Morales, "Design strategies for shape-controlled magnetic iron oxide nanoparticles," *Advanced Drug Delivery Reviews,* vol. 138, pp. 68-104, 2019, doi: https://doi.org/10.1016/j.addr.2018.12.008.

[99] D. Ortega and Q. A. Pankhurst, "Magnetic hyperthermia," *Nanoscience,* vol. 1, no. 60, p. e88, 2013, doi: https://doi.org/10.1039/9781849734844-00060.

[100] T. Carvalho, P. Torres, J. Belo, J. Mano, and S. Olhero, "Bioactive Magnetic Materials in Bone Tissue Engineering: A Review of Recent Findings in CaP-Based Particles and 3D-Printed Scaffolds," *Advanced NanoBiomed Research,* vol. 3, no. 9, p. 2300035, 2023, doi: https://doi.org/10.1002/anbr.202300035.

[101] M. M. Fernandes, D. M. Correia, C. Ribeiro, N. Castro, V. Correia, and S. Lanceros-Mendez, "Bioinspired Three-Dimensional Magnetoactive Scaffolds for Bone Tissue Engineering," *ACS Applied Materials & Interfaces,* vol. 11, no. 48, pp. 45265-45275, 2019, doi: https://doi.org/10.1021/acsami.9b14001.

[102] P. Martins, C. Costa, J. Ferreira, and S. Lanceros-Mendez, "Correlation between crystallization kinetics and electroactive polymer phase nucleation in ferrite/poly (vinylidene fluoride)

magnetoelectric nanocomposites," *The Journal of Physical Chemistry B,* vol. 116, no. 2, pp. 794-801, 2012, doi: https://doi.org/10.1021/jp210493t.

[103] P. Martins, Y. V. Kolen'ko, J. Rivas, and S. Lanceros-Mendez, "Tailored magnetic and magnetoelectric responses of polymer-based composites," *ACS applied materials & interfaces,* vol. 7, no. 27, pp. 15017-15022, 2015, doi: https://doi.org/10.1021/acsami.5b04102.

[104] C. Ribeiro, V. Correia, P. Martins, F. M. Gama, and S. Lanceros-Mendez, "Proving the suitability of magnetoelectric stimuli for tissue engineering applications," *Colloids and Surfaces B: Biointerfaces,* vol. 140, pp. 430-436, 2016, doi: https://doi.org/10.1016/j.colsurfb.2015.12.055.

[105] F. Mushtaq *et al.*, "Magnetoelectric 3D scaffolds for enhanced bone cell proliferation," *Applied Materials Today,* vol. 16, pp. 290-300, 2019, doi: https://doi.org/10.1016/j.apmt.2019.06.004.

[106] W. F. Lai and Z. D. He, "Design and fabrication of hydrogel-based nanoparticulate systems for in vivo drug delivery," (in eng), *Journal of Controlled Release,* vol. 243, pp. 269-282, 2016, doi: https://doi.org/10.1016/j.jconrel.2016.10.013.

[107] S. Bashir *et al.*, "Fundamental concepts of hydrogels: Synthesis, properties, and their applications," *Polymers,* vol. 12, no. 11, p. 2702, 2020, doi: https://doi.org/10.3390/polym12112702.

[108] K. M. Park, D. Lewis, and S. Gerecht, "Bioinspired hydrogels to engineer cancer microenvironments," *Annual review of biomedical engineering,* vol. 19, pp. 109-133, 2017, doi: https://doi.org/10.1146/annurev-bioeng-071516-044619.

[109] K. E. Kadler, C. Baldock, J. Bella, and R. P. Boot-Handford, "Collagens at a glance," *Journal of Cell Science,* vol. 120, no. 12, pp. 1955-1958, 2007, doi: https://doi.org/10.1242/jcs.03453.

[110] J. M. Orban, L. B. Wilson, J. A. Kofroth, M. S. El-Kurdi, T. M. Maul, and D. A. Vorp, "Crosslinking of collagen gels by transglutaminase," *Journal of biomedical materials research Part A,* vol. 68, no. 4, pp. 756-762, 2004, doi: https://doi.org/10.1002/jbm.a.20110.

[111] P. J. Hogg and C. M. Jackson, "Fibrin monomer protects thrombin from inactivation by heparin-antithrombin III: implications for heparin efficacy," *Proceedings of the National Academy of Sciences,* vol. 86, no. 10, pp. 3619-3623, 1989, doi: https://doi.org/10.1073/pnas.86.10.3619.

[112] H. Tan, C. R. Chu, K. A. Payne, and K. G. Marra, "Injectable *in situ* forming biodegradable chitosan–hyaluronic acid based hydrogels for cartilage tissue engineering," *Biomaterials,* vol. 30, no. 13, pp. 2499-2506, 2009, doi: https://doi.org/10.1016/j.biomaterials.2008.12.080.

[113] J. Berger, M. Reist, J. M. Mayer, O. Felt, and R. Gurny, "Structure and interactions in chitosan hydrogels formed by complexation or aggregation for biomedical applications," *European Journal of Pharmaceutics and Biopharmaceutics,* vol. 57, no. 1, pp. 35-52, 2004, doi: https://doi.org/10.1016/S0939-6411(03)00160-7.

[114] M. Liu *et al.*, "Injectable hydrogels for cartilage and bone tissue engineering," *Bone Research,* vol. 5, no. 1, p. 17014, 2017, doi: https://doi.org/10.1038/boneres.2017.14.

[115] W. Hu, Z. Wang, Y. Xiao, S. Zhang, and J. Wang, "Advances in crosslinking strategies of biomedical hydrogels," *Biomaterials science,* vol. 7, no. 3, pp. 843-855, 2019, doi: https://doi.org/10.1039/C8BM01246F.

[116] C. A. Vilela *et al.*, "*In vitro* and *in vivo* performance of methacrylated gellan gum hydrogel formulations for cartilage repair*," *Journal of Biomedical Materials Research Part A,* vol. 106, no. 7, pp. 1987-1996, 2018, doi: https://doi.org/10.1002/jbm.a.36406.

[117] B. Hermenegildo *et al.*, "Hydrogel-based magnetoelectric microenvironments for tissue stimulation," *Colloids and Surfaces B: Biointerfaces,* vol. 181, pp. 1041-1047, 2019, doi: https://doi.org/10.1016/j.colsurfb.2019.06.023.

[118] E. O. Carvalho, C. Ribeiro, D. M. Correia, G. Botelho, and S. Lanceros-Mendez, "Biodegradable hydrogels loaded with magnetically responsive microspheres as 2D and 3D scaffolds," *Nanomaterials,* vol. 10, no. 12, p. 2421, 2020, doi: https://doi.org/10.3390/nano10122421.

[119] N. D. Ferson, A. M. Uhl, and J. S. Andrew, "Piezoelectric and magnetoelectric scaffolds for tissue regeneration and biomedicine: A review," *IEEE transactions on ultrasonics, ferroelectrics, and frequency control,* vol. 68, no. 2, pp. 229-241, 2020, doi: https://doi.org/10.1109/tuffc.2020.3020283.

[120] D. N. Heo *et al.*, "Enhanced bone regeneration with a gold nanoparticle–hydrogel complex," *Journal of Materials Chemistry B,* vol. 2, no. 11, pp. 1584-1593, 2014, doi: https://doi.org/10.1039/C3TB21246G.

[121] S. Stenfelt *et al.*, "Pre-incubation of chemically crosslinked hyaluronan-based hydrogels, loaded with BMP-2 and hydroxyapatite, and its effect on ectopic bone formation," *Journal of Materials Science: Materials in Medicine,* vol. 25, no. 4, pp. 1013-1023, 2014, doi: https://doi.org/10.1007/s10856-014-5147-y.

[122] C. W. Hull, "The birth of 3D printing," *Research-Technology Management,* vol. 58, no. 6, pp. 25-30, 2015, doi: https://doi.org/10.5437/08956308X5806067.

[123] F. P. Melchels, J. Feijen, and D. W. Grijpma, "A review on stereolithography and its applications in biomedical engineering," *Biomaterials,* vol. 31, no. 24, pp. 6121-6130, 2010, doi: https://doi.org/10.1016/j.biomaterials.2010.04.050.

[124] J. Z. Manapat, Q. Chen, P. Ye, and R. C. Advincula, "3D Printing of Polymer Nanocomposites via Stereolithography," *Macromolecular Materials and Engineering,* vol. 302, no. 9, p. 1600553, 2017, doi: 10.1002/mame.201600553.

[125] K.-S. Lee, R. H. Kim, D.-Y. Yang, and S. H. Park, "Advances in 3D nano/microfabrication using two-photon initiated polymerization," *Progress in Polymer Science,* vol. 33, no. 6, pp. 631-681, 2008, doi: https://doi.org/10.1016/j.progpolymsci.2008.01.001.

[126] E. Sachs, M. Cima, P. Williams, D. Brancazio, and J. Cornie, "Three dimensional printing: rapid tooling and prototypes directly from a CAD model," *CIRP Annals*, vol. 39, no. 1, pp. 201-204, 1990, doi: https://doi.org/10.1016/S0007-8506(07)61035-X.

[127] F. L. Amorim, A. Lohrengel, V. Neubert, C. F. Higa, and T. Czelusniak, "Selective laser sintering of Mo-CuNi composite to be used as EDM electrode," *Rapid Prototyping Journal,* vol. 20, no. 1, pp. 59-68, 2014, doi: https://doi.org/10.1108/RPJ-04-2012-0035.

[128] U. Ajoku, N. Hopkinson, and M. Caine, "Experimental measurement and finite element modelling of the compressive properties of laser sintered Nylon-12," *Materials Science and Engineering: A,* vol. 428, no. 1-2, pp. 211-216, 2006, doi: https://doi.org/10.1016/j.msea.2006.05.019.

[129] S. F. S. Shirazi *et al.*, "A review on powder-based additive manufacturing for tissue engineering: selective laser sintering and inkjet 3D printing," *Science and technology of advanced materials,* vol. 16, no. 3, p. 033502, 2015, doi: https://doi.org/10.1088/1468-6996/16/3/033502.

[130] T. Traini, C. Mangano, R. Sammons, F. Mangano, A. Macchi, and A. Piattelli, "Direct laser metal sintering as a new approach to fabrication of an isoelastic functionally graded material for manufacture of porous titanium dental implants," *Dental materials,* vol. 24, no. 11, pp. 1525-1533, 2008.

[131] P. Siemiński, "Chapter 7 - Introduction to fused deposition modeling," in *Additive Manufacturing*, J. Pou, A. Riveiro, and J. P. Davim Eds.: Elsevier, pp. 217-275, 2021, doi: https://doi.org/10.1016/j.dental.2008.03.029.

[132] R. Jones *et al.*, "RepRap–the replicating rapid prototyper," *Robotica,* vol. 29, no. 1, pp. 177-191, 2011, doi: https://doi.org/10.1017/S026357471000069X.

[133] E. Gkartzou, E. P. Koumoulos, and C. A. Charitidis, "Production and 3D printing processing of bio-based thermoplastic filament," *Manufacturing Review,* vol. 4, p. 1, 2017, doi: https://doi.org/10.1051/mfreview/2016020.

[134] A. C. de Leon, Q. Chen, N. B. Palaganas, J. O. Palaganas, J. Manapat, and R. C. Advincula, "High performance polymer nanocomposites for additive manufacturing applications," *Reactive and Functional Polymers,* vol. 103, pp. 141-155, 2016, doi: https://doi.org/10.1016/j.reactfunctpolym.2016.04.010.

[135] N. Bhattacharjee, A. Urrios, S. Kang, and A. Folch, "The upcoming 3D-printing revolution in microfluidics," *Lab on a Chip,* vol. 16, no. 10, pp. 1720-1742, 2016, doi: https://doi.org/10.1039/C6LC00163G.

[136] R. E. Saunders and B. Derby, "Inkjet printing biomaterials for tissue engineering: bioprinting," *International Materials Reviews,* vol. 59, no. 8, pp. 430-448, 2014, doi: https://doi.org/10.1179/1743280414y.0000000040.

[137] X. Li *et al.*, "Inkjet Bioprinting of Biomaterials," *Chemical Reviews,* vol. 120, no. 19, pp. 10793-10833, 2020, doi: https://doi.org/10.1021/acs.chemrev.0c00008.

[138] C. Dou, V. Perez, J. Qu, A. Tsin, B. Xu, and J. Li, "A state-of-the-art review of laser-assisted bioprinting and its future research trends," *ChemBioEng Reviews,* vol. 8, no. 5, pp. 517-534, 2021, doi: https://doi.org/10.1002/cben.202000037.

[139] A. Zennifer, A. Subramanian, and S. Sethuraman, "Design considerations of bioinks for laser bioprinting technique towards tissue regenerative applications," *Bioprinting,* vol. 27, p. e00205, 2022, doi: https://doi.org/10.1016/j.bprint.2022.e00205.

[140] O. Alheib, L. da Silva, Y. Youn, I. Kwon, R. Reis, and V. Correlo, "Chapter 19 - 3D bioprinting: a step forward in creating engineered human tissues and organs," in *Additive Manufacturing*, J. Pou, A. Riveiro, and J. P. Davim Eds.: Elsevier, pp. 599-633, 2021, doi: https://doi.org/10.1016/B978-0-12-818411-0.00016-1.

[141] J. Li, M. Chen, X. Fan, and H. Zhou, "Recent advances in bioprinting techniques: approaches, applications and future prospects," *Journal of Translational Medicine,* vol. 14, no. 1, p. 271, 2016, doi: https://doi-org/10.1186/s12967-016-1028-0.

[142] I. Holland, "Extrusion bioprinting: meeting the promise of human tissue biofabrication?," (in eng), *Progress in biomedical engineering,* vol. 7, no. 2, 2025, doi: https://doi.org/10.1088/2516-1091/adb254.

[143] J. Choi *et al.*, "Preparation and characterization of an injectable dexamethasone-cyclodextrin complexes-loaded gellan gum hydrogel for cartilage tissue engineering," *Journal of Controlled Release,* vol. 327, pp. 747-765, 2020, doi: https://doi.org/10.1016/j.jconrel.2020.08.049.

[144] P. Abdollahiyan, F. Oroojalian, A. Mokhtarzadeh, and M. de la Guardia, "Hydrogel-Based 3D Bioprinting for Bone and Cartilage Tissue Engineering," *Biotechnology Journal,* vol. 15, no. 12, p. 2000095, 2020, doi: https://doi.org/10.1002/biot.202000095.

[145] M. T. Poldervaart *et al.*, "3D bioprinting of methacrylated hyaluronic acid (MeHA) hydrogel with intrinsic osteogenicity," *PloS one,* vol. 12, no. 6, p. e0177628, 2017, doi: https://doi.org/10.1371/journal.pone.0177628.

[146] S. T. Bendtsen, S. P. Quinnell, and M. Wei, "Development of a novel alginate-polyvinyl alcohol-hydroxyapatite hydrogel for 3D bioprinting bone tissue engineered scaffolds," *Journal of Biomedical Materials Research Part A,* vol. 105, no. 5, pp. 1457-1468, 2017, doi: https://doi.org/10.1002/jbm.a.36036.

[147] C. Cao, P. Huang, A. Prasopthum, A. Parsons, F. Ai, and J. Yang, "Characterisation of bone regeneration in 3D printed ductile PCL/PEG/hydroxyapatite scaffolds with high ceramic microparticle concentrations," *Biomaterials Science,* vol. 10, no. 1, pp. 138-152, 2022, doi: https://doi.org/10.1039/D1BM01645H.

[148] L. Zhong *et al.*, "3D printing of metal–organic framework incorporated porous scaffolds to promote osteogenic differentiation and bone regeneration," *Nanoscale,* vol. 12, no. 48, pp. 24437-24449, 2020, doi: https://doi.org/10.1039/D0NR06297A.

CHAPTER 2

3D poly(3-hydroxybutyrate-*co*-3-hydroxyvalerate) scaffolds

Based on the following publication (under submission):

3D magnetoelectric polymer composite scaffolds for tissue engineering

André S Macedo, Ricardo Brito-Pereira, Diana Bogas, Clarisse Ribeiro, Senentxu Lanceros-Méndez

2.1. Introduction

As 3D printing, also known as AM, becomes more accessible, new avenues are opened to more researchers, specifically those who do not have access to the latest top tier technology. According to both American Society for Testing and Materials (ASTM) and International Organization for Standardization (ISO), it can be classified into seven types: material extrusion, directed energy deposition, binder jetting, sheet lamination, powder bed fusion, material jetting, and vat photopolymerization [1]. FDM, an example of the first type, consists of melting and depositing a thermoplastic filament, through a nozzle, and onto a printing bed according to a previously designed CAD software file to build a 3D structure. With printer models in affordable ranges and often inexpensive filaments, it has had wide-ranging impact, producing 3D-printed parts as diverse as molds for turbine blade production, downhill bike rockers, suspension parts for a lunar rover [2]; the creation of patient-specific implants and prosthetics [1]; a number of military applications ranging from biomedical to lighter parts for unmanned airborne vehicles, aiding the conceptualization and design processes through the fabrication of functional prototypes to end-use parts [3]; or, in the pharmaceutical industry, the tuning of rate of drug release from a structure by the choice of material used to print it [4]. Also, in a world where environmental consciousness is prevalent, filaments can be produced from recycling of common plastics such as PLA, ABS, polyethylene terephthalate (PET), high-density polyethylene (HDPE), polypropylene (PP), PS, and high impact PS (HIPS). Natural fibers derived from hemp or kenaf have also been combined with other polymers, such as the aforementioned ones, to produce composites with improved properties [5]. Other filaments may exhibit different properties that can be exploited. PVA and BVOH are both water-soluble polymers, which allows them to act as sacrificial molds – a technique where a mold is filled with a polymeric solution and after solidifying or curing, is typically immersed in water or other target solvent to completely wash away the mold, leaving a scaffold composed only of the previously injected polymer [6]. Since scaffolds play a crucial role in TE, this is an area where FDM has also made a significant impact. The architecture and composition of the cellular microenvironment influence cell behavior and can either promote or inhibit cell growth.

As cells respond to different stimuli, growth can be further promoted by taking advantage of a material's intrinsic properties such as piezoelectricity, the ability of a material to convert mechanical deformation into an electric stimulus or vice-versa. As bone tissue is also inherently piezoelectric, electromechanical effects can play a role in bone cell behavior and thus their growth can be modulated through the application of this kind of stimulus [7]. The piezoelectric effect can also be coupled with magnetostriction, a phenomenon in which mechanical deformation occurs when a magnetic field is

applied, forming the magnetoelectric effect, defined as dielectric polarization of a material under an applied magnetic field or an induced magnetization under an external electric field [8].

PHBV is a piezoelectric polymer of the polyhydroxyalkanoates (PHAs) family, a group of biodegradable polyesters that are intracellularly synthesized as an energy reserve by various bacteria, and thus represent a promising candidate to replace petroleum-based plastics. PHBV is a thermoplastic polyester composed of hydroxybutyrate (HB) units with approximately 0 - 24% of hydroxyvalerate (HV) units randomly interspersed throughout the polymer chain [9]. The introduction of HV improves the polymer's mechanical flexibility/ductility while lowering its melting point [10]. To provide the magnetostrictive element, MNPs are often introduced into piezoelectric matrices or composite structures [11-13]. The magnetoelectric effect has been extensively researched in TE using different piezoelectric polymers such as PVDF and PLLA combined with MNPs composed of iron oxide or cobalt ferrite [14], as well as silk fibroin films and electrospun membranes [15]. The effect of PHBV and cobalt ferrite microspheres on *in vitro* neuronal and glial response has also been evaluated [16]. Other researchers have found success using core/shell structured Fe_3O_4@$BaTiO_3$ MNP-loaded hyaluronan/collagen hydrogels in nerve regeneration [17].

In this study, we present pure and Fe_3O_4-loaded PHBV scaffolds designed for bone TE. The scaffolds were fabricated using a soluble 3D-printed sacrificial mold. Morphological and physicochemical characterization was carried out to assess structural precision and the resulting material properties. The scaffold's influence on the biocompatibility, attachment and proliferation of MC3T3-E1 preosteoblast was also evaluated.

2.2. Materials and methods

2.2.1. Materials

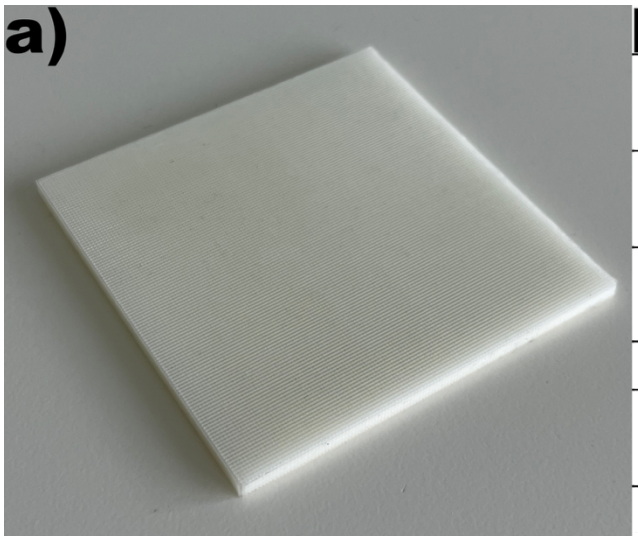
3D printing BVOH 1.75 mm Natural (part Number 55903) filament was acquired from Verbatim (Verbatim GmbH, Eschborn, Germany). PHBV (1.24 $g.cm^{-3}$ density; HV mole fraction of 3%; >98% purity) with product reference PHI 003 was supplied from NaturePlast (Mondeville, France). Iron(II,III) oxide (Fe_3O_4, 99%, 30 nm) NPs were acquired from Nanoamor. Chloroform (99% purity) and dimethyl sulfoxide (DMSO), resazurin sodium salt, and formaldehyde solution (37 wt.% in H_2O, solution, ACS reagent grade, 10-15% methanol) were acquired from Merck (Merck KGaA, Darmstadt, Germany). 0.25% trypsin–ethylenediaminetetraacetic acid (trypsin–EDTA, Biochrom), Dulbecco's Modified Eagle Medium (DMEM) low glucose (1 $g.L^{-1}$) was supplemented with 10% fetal bovine serum (FBS) (both acquired from

PAN-Biotech (PAN-Biotech GmbH, Aidenbach, Bayern, Germany)) and penicillin/streptomycin (P/S),was acquired from Biochrom (Harvard Bioscience, Inc., Massachusetts, USA). 4′,6-diamidino-2-phenylindole (DAPI) and fluorescein isothiocyanate (FITC) were acquired from Hello Bio (Hello Bio Inc, Bristol, United Kingdom).

2.2.2. 3D Printing of sacrificial molds

Printing was carried out using a Prusa i3 MK3 (Prusa Research, Prague, Czechia) model with a 0.25 mm nozzle. The 72.2x72.2x3.2 mm grid sacrificial mold illustrated in Figure 2.1a) was printed using the settings in Figure 2.1b). These settings were selected to ensure dimensional precision, adequate filament adhesion, and complete removal during dissolution.

a)



b)

Parameter	Value
Layer Height	0.2 mm (first layer) 0.15 mm (ensuing layers)
Fill Density and Pattern	20% Grid
Printing Speed	30 $mm.s^{-1}$ (perimeter) 45 $mm.s^{-1}$ (infill)
Filament Diameter	1.75 mm
Nozzle Temperature	215 °C (first layer) 210 °C (ensuing layers)
Bed Temperature	60 °C

Figure 2.1. a) BVOH 3D-printed sacrificial mold and corresponding **b)** printing parameters.

2.2.3. Preparation of 3D PHBV scaffolds

For magnetoelectric samples, depending on the desired amount, 10 or 20% (w/w) Fe_3O_4 of the polymer mass was dispersed in the chloroform solution in an FB 15056 (Fisher Scientific, Hampton, New Hampshire, United States of America) ultrasonic bath for 20 min. Subsequently, PHBV (10% w/v) was dissolved under mechanical stirring (≈1500 rpm) on a heating plate (Hei-PLATE Mix 'n' Heat Core+, Heidolph Instruments, Schwabach, Germany) at 50 °C for 5 min. Aluminum foil was wrapped around the stirring shaft to cover the beaker and minimize solution evaporation. After this period, the solution was removed from the plate to cool down while stirring was maintained.

Beforehand, the printed BVOH mold was cut into four pieces of identical size. Each piece was placed in a petri dish, and the solution was poured on top until it was almost completely submerged, then gently swirled to facilitate solution penetration into the mold cavities. The mold was then transferred to a glass substrate, and each surface was scraped to remove excess solution and to prevent the formation of a film over the structure. The samples were left to dry overnight. Afterwards, they were immersed in 1 L of deionized H_2O (diH_2O) to wash out the sacrificial BVOH mold for 24 h, then further rinsed with diH_2O using a wash bottle, and finally cut into 1x1x0.3 cm cuboids for characterization and cell studies.

2.2.4. Morphological and physicochemical characterization

To assess the morphology of the scaffolds, stereo microscopy analysis was done using a Leica S Apo stereomicroscope (Leica Microsystems, Wetzlar, Germany) with a built-in camera system. Images were captured using the Leica Application Suite (LAS version 4.12.0).

For scanning electron microscopy (SEM) and energy-dispersive X-ray (EDX) analysis, samples were previously coated with a thin gold layer by magnetron sputtering using a Polaron SC502 (Quorum Technologies Ltd, Lewes, East Sussex, England). Morphology was examined with a Hitachi S-4800 (Hitachi High-Technologies Corporation, Tokyo, Japan) at 5 kV beam acceleration voltage. ImageJ software (version 1.54g) was used to measure the area, perimeter and circularity of the scaffolds' pores, with results expressed as the mean ± standard deviation (SD) of 50 measurements per sample. For the elemental composition analysis, a Carl Zeiss EVO 40 (Oberkochen, Germany) SEM equipped with an EDS Oxford Instrument X-Max (Abingdon, UK) EDX detector was used.

Surface topology and local piezoelectric response of the scaffolds were analyzed using piezoresponse force microscopy (PFM). A Nano-Observer atomic force microscope (AFM) from Concept Scientific Instruments (Les Ulis, France), equipped with a high voltage amplifier, was used in piezo response mode at RT. Pt/Ir-coated N-type Si tips from the AppNano (Applied NanoStructures, Inc., California, United States of America) ANSCM series were used, with a nominal spring constant of 3 $N.m^{-1}$, an intrinsic resonance frequency of 60 kHz, and a tip radius of 30 nm. After calibration with the spectroscopy curve, the voltage set point was selected so that the force exerted on the sample was around 10 nN. The AC voltage applied had an amplitude of 4 V. An area of 10 μm^2 was scanned with a resolution of 256 × 256 points at a scan rate of 1 Hz. To characterize switching behavior, DC voltage varying from -100 to 100 V was applied to the tip while measuring the piezoelectric response. The images obtained from the microscope were treated with Gwyddion software (version 2.66).

Fourier transform infrared (FTIR) spectroscopy was performed at RT from 4000 to 600 cm^{-1} using a Spectrum spectrometer (PerkinElmer, Inc., Waltham, Massachusetts, United States of America) linked with an attenuated total reflectance (ATR) PerkinElmer single reflection diamond accessory. Spectra were recorded with 64 scans at a resolution of 4 cm^{-1}.

For differential scanning calorimetry (DSC), approximately 3 mg pieces of each sample were placed into 50 µL aluminum pans and thermally analyzed with a PerkinElmer DSC 6000 apparatus. Samples were heated at a rate of 10 °C.min^{-1} between 30 and 200 °C. The crystallinity degree (X_C) percentage of each sample was calculated using Equation 2.1:

$$X_C(\%) = \frac{\Delta H_f}{\Delta \mathrm{H}_f{}^{\mathrm{o}}} \times \frac{100}{W} \quad \textbf{(2.1)}$$

where ΔH_f corresponds to the experimental enthalpy of fusion and $\Delta \mathrm{H}_f{}^{\mathrm{o}}$ to a value of 109 $J.g^{-1}$ corresponding to 100% crystalline PHBV [18], and W the polymer weight fraction in the sample.

The mechanical measurements of the scaffolds were performed at RT using a Shimadzu AD-IS universal testing setup in compression mode. Three cuboid samples with a height of 3 mm and surface area of 1 cm^2 were analyzed using a 500 N load cell. The modulus of elasticity (*E*), or Young's modulus, was determined from the linear zone of elasticity.

Vibrating sample magnetometry (VSM) was carried out using a MicroSense EZ7 (KLA Corporation, Lowel, Massachusetts, United States of America) magnetometer. An applied field from -20 to 20 kOe allowed the measurement of the magnetic hysteresis loop until magnetization saturation. Fe_3O_4 filler content in the scaffolds was determined according to Equation 2.2:

$$NP\ filler\ wt\% = \frac{M_{scaffold}}{M_{NP}} \times 100 \quad \textbf{(2.2)}$$

where $M_{scaffold}$ corresponds to the magnetization measured for each sample and M_{NP} to the magnetization of the pure Fe_3O_4 NPs.

Water contact angle (WCA) measurements were performed using an Ossila Contact Angle Goniometer (Sheffield, United Kingdom). A 3 µL drop of diH_2O was deposited on the surface of the scaffold using a microsyringe. Three measurements were performed in different locations on each type of scaffold and are presented as mean and corresponding SD.

Scaffold porosity was determined using the liquid displacement technique in a pycnometer. Absolute ethanol was used to fill the apparatus and the total weight (W_1) was measured. Each sample was also weighed (W_S), individually, put in the pycnometer, then immersed and saturated with ethanol until fully infiltrated. The apparatus was weighed (W_2), the sample extracted and the pycnometer's weight measured again (W_3). The porosity of each scaffold was calculated according to Equation 2.3. Three measurements were performed for each type of scaffold and are presented as mean ± SD.

$$\varepsilon = \frac{W_2 - W_3 - W_S}{W_1 - W_3} \quad \textbf{(2.3)}$$

For the degradation studies, samples were placed in 24-well tissue culture polystyrene (TCPS) plates containing 500 µL of phosphate-buffered saline (PBS, 1×) or Dulbecco's DMEM containing 1 $g.L^{-1}$ glucose. To better assess structural degradation, images were taken at two different timepoints, 30 and 40 days, under both static and dynamic conditions. The dynamic condition was performed using a home-made magnetic bioreactor system. Samples were subjected to magnetic stimulation following a 1 h on/11 h off cycle at a frequency of 0.3 Hz. A 16 mm displacement of the permanent magnets below the wells caused a maximum magnetic field variation from 0.23 to -0.23 T at the bottom of the wells.

2.2.5. Cell studies

Before any assay, scaffolds were sterilized by overnight immersion and stirring in 70% ethanol, dried for 24 h, UV-irradiated on both sides for 1 h, and aseptically stored until use. MC3T3-E1 preosteoblast cells (RIKEN Cell Bank, Japan) were used for cytotoxicity and proliferation tests. Cells were cultured in previously supplemented DMEM at 37 °C, in 95% humidified air containing 5% CO_2. Growth medium was replaced every three days, and when cells reached 60–70% confluence, they were detached using trypsin-EDTA and used in the following assays.

2.2.6. Cytotoxicity

Scaffold cytotoxicity was evaluated using an adaptation of the ISO 10993-5 standard test protocol. Scaffolds were placed in a 24-well TCPS plates and incubated with DMEM (700 µL per well). MC3T3-E1 cells were simultaneously seeded in a 96-well TCPS plate at a density of 3×10^4 $cells.mL^{-1}$ (100 µL per well). Both plates were then incubated for 24 h. After this period, medium of the 96-well plates was replaced with scaffold-conditioned medium (100 µL per well). DMSO (20% v/v) and fresh DMEM were

used as positive and negative controls, respectively, with DMSO also being added at this stage. The plate was then incubated for an additional 72 h, and cell viability was evaluated using a resazurin assay. For this, fresh medium containing 10% (v/v) resazurin solution was added to each well. After 2 h of incubation, the fluorescence was measured with fluorescence excitation at 560 nm and emission at 590 nm using a microplate reader (Tecan Infinite M Nano+, Tecan Trading AG, Switzerland). The number of flashes was set to 25, and manual gain to 75. Results are presented as the average cell viability ± SD and were calculated according to Equation 2.4:

$$Cell\ viability\ (\%) = \frac{ABS_{sample}}{ABS_{negative\ control}} \times 100 \quad \textbf{(2.4)}$$

2.2.7. Cell proliferation

PHBV scaffolds (pure, 10% Fe_3O_4, 20% Fe_3O_4) were placed in 24-well TCPS plates. Cell adhesion was assessed after 24 h of cell seeding (T_0), and cell proliferation was evaluated after 7 days (T_1) under both static and dynamic culture conditions. A total of 5 samples of each type of scaffold were evaluated for each experimental condition. The dynamic culture was performed using a home-made bioreactor system applying magnetic stimulation following a 1 h on/11 h off cycle at a frequency of 0.3 Hz. A 16 mm displacement of the permanent magnets below the wells generated a magnetic field variation from 0.23 to -0.23 T at the bottom of the wells.

Cells were seeded directly onto the samples by putting 120 µL of cell suspension (21×10^4 cells.mL^{-1}) on the top surface of each sample, followed by a 40 min incubation period. Afterwards, 480 µL of DMEM was added to each well to completely submerge the sample, and the plates were incubated under standard culture conditions for 24 h.

After 1 and 7 days (corresponding to T_0 and T_1, respectively), samples were transferred to new wells for the evaluation of cell adhesion (T_0) and proliferation (T_1). A resazurin solution (10% v/v relative to DMEM) was added to each well. After an incubation period of 3 h, three 100 µL from each well were transferred to a 96-well plate and analyzed using a multiplate reader under the same conditions previously mentioned. Results are presented as the average proliferation ± SD and calculated according to Equation 2.5:

$$Fold\ change = \frac{ABS_{T_1}}{ABS_{T_0}} \quad \textbf{(2.5)}$$

2.2.8. Fluorescence microscopy

During the cell proliferation assay, two additional samples of each type of scaffold were reserved for immunofluorescence staining to allow subsequent fluorescence microscopy analysis. The culture medium was removed from each well, and the samples were washed twice with PBS solution. Then, 500 µL of 4% formaldehyde was added, and the samples were incubated for 10 min, after which they were again washed with PBS. For the staining process, 500 µL of FITC diluted 1:100 in PBS were added to stain the cell cytoskeleton for 45 min. Samples were then washed twice with PBS, and the nuclei were stained by adding 500 µL of DAPI diluted 1:1000 ratio in PBS for 5 min, in the dark. After one last wash with PBS, the samples were observed in an Olympus BX51 (Olympus Corporation, Tokyo, Japan) fluorescence microscope.

2.2.9. Statistical analysis

The data were subjected to two-way analysis of variance (ANOVA) using OriginPro 2024 SR1 software version 10.1.0.178. Post hoc multiple comparisons were determined by Tukey's test, with the level of significance set at $p < 0.05$. Statistical differences are presented with different numbers of * according to this level.

2.3. Results and discussion

2.3.1. Morphology, topology and piezoelectric response of the scaffolds

To confirm the porous structure of the synthesized scaffolds, which is essential for cell infiltration and proliferation within the 3D architecture, microscopy analyses were performed. Stereo microscopy and SEM images are presented in Figure 2.2.

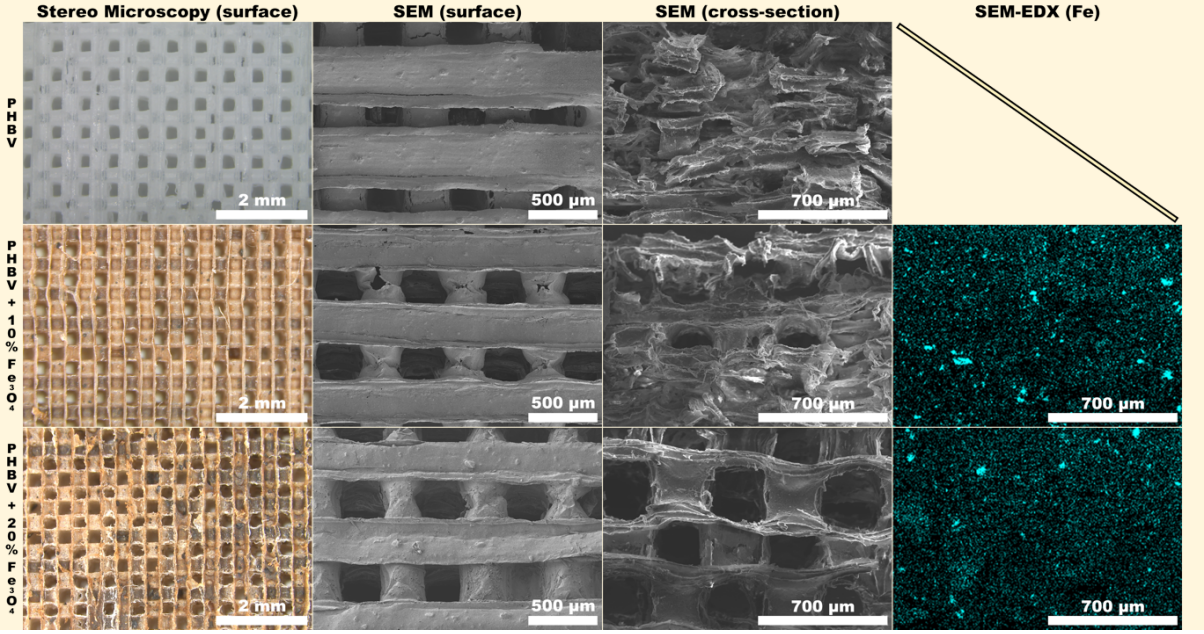


Figure 2.2. Representative images of the surface, cross-section and elemental composition of the pure and composite PHBV scaffolds via stereo microscopy, SEM, and SEM-EDX.

The images overall confirm the successful formation of a well-defined structure in all samples. The cross-sections of pure and 10% scaffolds collapsed while sectioning, as the 20% sample shows the porous structure well preserved. Quantitative measurements obtained from the stereo microscopy images are presented in Table 2.1.

Table 2.1. Measurements of the areas, perimeter and circularity of the pores of the 3D pure and composite PHBV scaffolds.

	Area (µm²)	**Perimeter (µm)**	**Circularity**
PHBV	46.0 ± 9.9	824.6 ± 84.9	0.84 ± 0.0
PHBV 10% Fe_3O_4	69.6 ± 18.2	1029.8 ± 123.2	0.82 ± 0.1
PHBV 20% Fe_3O_4	68.0 ± 15.9	983.2 ± 111.0	0.87 ± 0.0

Although pure PHBV scaffolds appear to exhibit slightly lower average pore area and perimeter, these values remain within the SD range of the composite scaffolds. As NP dispersion is not ideal, their presence may induce minor irregularities in the filament layers. The overall SD of the average pore area and perimeter, as well as the presence of partially obstructed pores, are likely the result of different factors. The printing of the mold was done at the limit of the printer's resolution, where the natural variability in the filament's melting and solidification process may cause partial obstruction of some pores or generate slightly thicker or thinner filaments relative to the design, which, at the micrometer scale,

can lead to considerable differences. These small defects may be further amplified during the mold submersion and filling process, where the interstices may not be perfectly filled by the solution, either due to already-obstructed pores or by the progressive and rapid evaporation of the solvent. This evaporation leads to an increase in viscosity that may prevent the solution of reaching some spaces. Although hollow spaces resulting from incomplete filling are not visible, SEM images also show the odd tear in the polymer strip. This can either come as a consequence of some partial filling of the pores or from the subsequent synthesis process, consistent with PHBV's inherently low mechanical strength [19].

Stereo microscopy images of the composite scaffolds show zones with different shades of brown, suggesting particle dispersion is not completely homogeneous. This is more apparent in the 20% sample, where the right half is noticeably darker than the other half. Fewer, smaller spots of NP aggregates are also visible throughout. Some aggregation is to be expected as a result of changes in rate of dispersion of the polymeric solution through the mold as the solvent evaporates, as chloroform is extremely volatile. This may cause NPs to become gradually trapped in different zones and aggregate while the solution is completely evaporated, leading to uneven distribution. SEM-EDX for Fe content provides a clearer picture: although the smaller, denser aggregates are still visible, the overall NP distribution is much more homogeneous than that suggested by stereo microscopy. This difference is due to the latter only captures the surface morphology, whereas EDX probes the elemental composition throughout the scaffold's depth.

Representative images of PFM analysis of the pure PHBV scaffolds are presented in Figure 2.3.

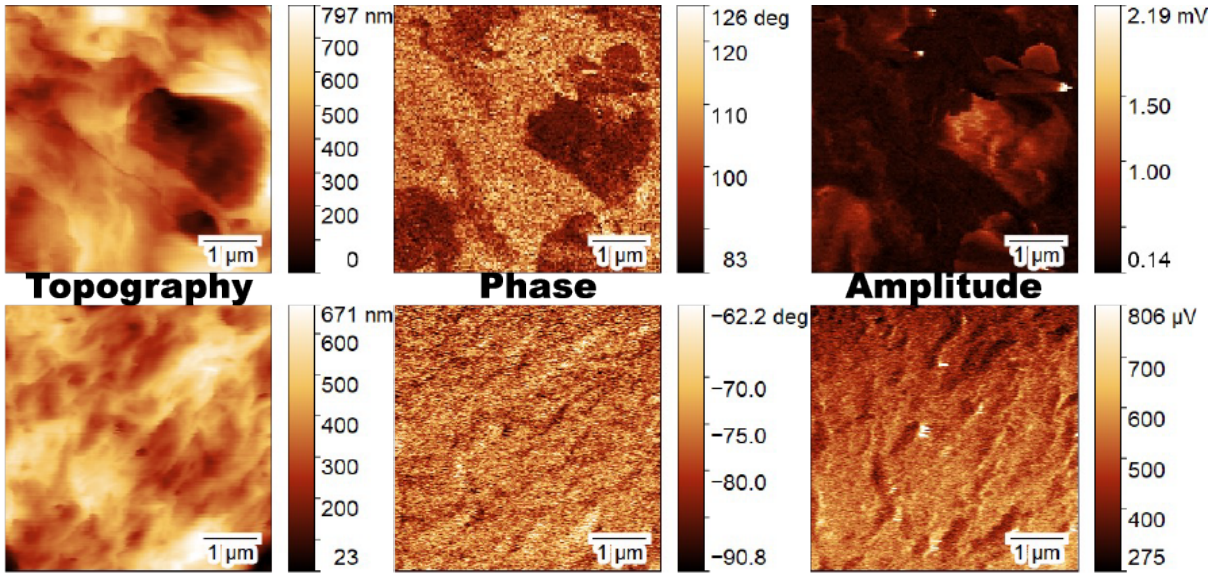


Figure 2.3. Representative piezoresponse force microscopy images of the topography, phase and amplitude maps of two pure PHBV scaffolds.

The topography maps show considerable surface variation, with the sample from the first row in Figure 2.3 exhibiting values ranging from below 100 to above 700 nm. The second sample presents similar topographical variations. This reveals a finely textured surface, at a smaller scale than the observed in the SEM images. Such texture may result from the presence of crystalline grains and from the rapid and heterogeneous evaporation of the polymeric solution during processing.

Comparing the topography and amplitude maps, some correlation between them can be observed. Both rows correspond to different regions of the same pure PHBV scaffold. In the first sample, the correlation appears negative, the center-right region, which has a lower height, still exhibits signal, whereas in the second sample, a positive correlation is noted. This suggests that the observed signal is mainly influenced by surface roughness rather than by the intrinsic piezoelectric properties of the material. Although a detectable signal is present, the limited sensitivity of the equipment to weak piezoelectric responses (techniques such as Dual AC Resonance Tracking (DART)-PFM could potentially provide clearer results) and the fragile nature of the scaffold does not allow for definitive confirmation of piezoelectricity. The low signal intensity (below 2 mV) and the lack of consistent phase contrast further support this interpretation. As some degree of surface charge distribution is present, but not organized into stable, aligned dipolar domains, any piezoelectric response would likely occur only at the molecular level, consistent with the low polar crystallinity of PHBV.

2.3.2. Physical and chemical characterization

Figure 2.4 presents results obtained for DSC, FTIR-ATR, mechanical compression and VSM analysis.

Figure 2.4a) presents the DSC thermograms of the pure and Fe_3O_4-loaded PHBV scaffolds. Melting temperature (T_m) and the enthalpy associated with each endothermic peak are presented in Table 2.2. The main melting peak appears slightly above 177 °C for the pure PHBV samples and slightly below this value for the composite samples. PHB has a melting point close to 180 °C, and the introduction of the HV comonomer tends to lower this value [20], with melting points in the range of 170-176 °C reported in the literature for 3 mol% HV [21], as well as in the supplier's datasheet. Small variations can be expected, as the same polymer from the same manufacturer has been reported by other authors to exhibit a T_m of 174.3 °C [22].

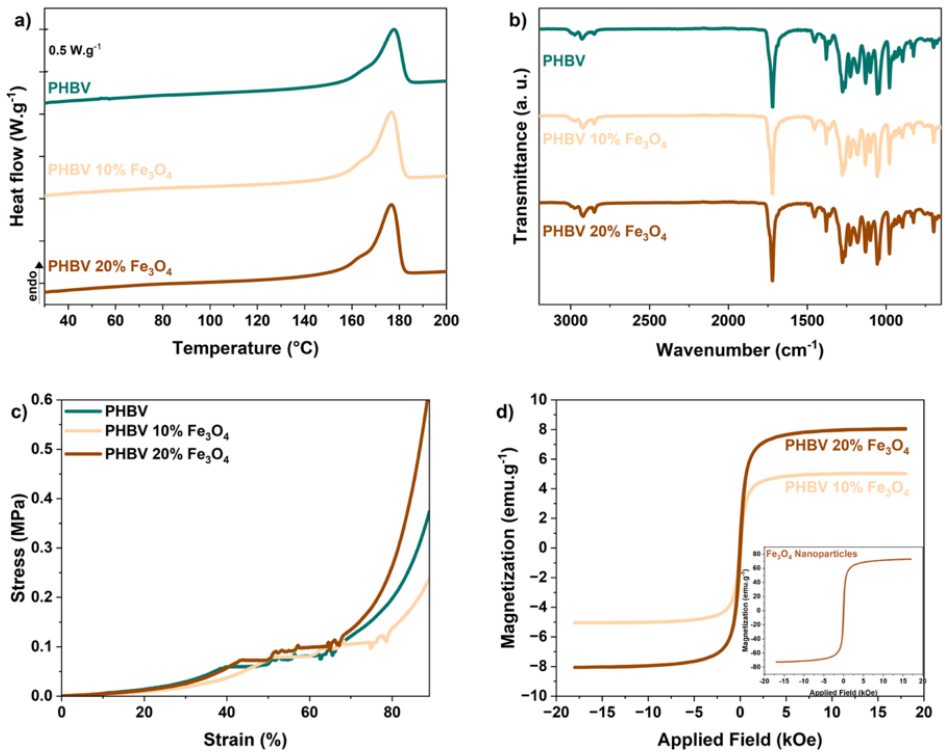


Figure 2.4. a) DSC scans, **b)** FTIR-ATR spectra, **c)** mechanical compression stress-strain curves, and **d)** VSM hysteresis curves of the pure and composite PHBV scaffolds.

The crystallinity degree (X_c) for each sample, calculated from Equation 2.1 as previously mentioned, is also presented in Table 2.2.

Table 2.2. Crystallinity degree of the pure and composite PHBV scaffolds.

Sample	X_C (%)
PHBV	57.9
PHBV + 10% Fe_3O_4	61.5
PHBV + 20% Fe_3O_4	55.6

Higher crystallinity has been observed in composite samples which may be due to the role of Fe_3O_4 NPs as effective nucleating agents for PHBV crystallization, a phenomenon previously reported in the literature for different types of NPs [23-25]. Although the 10% sample has a 3.4% higher crystallinity than the pure polymer sample, the 20% scaffold has a slightly lower value than the 10% composite. Hence, NP integration does not appear to significantly affect X_C.

FTIR-ATR spectra (Figure 2.4b)) are nearly identical for all three samples, showing the typical absorption profile of PHBV [26]. A small peak in the region of 2900 cm^{-1}, attributed to C–H stretching bonds, is observed, while the most intense band around 1724 cm^{-1} corresponds to the C=O stretching

vibration of ester functional groups, characteristic of the PHB component [27]. A series of peaks of moderate to high intensity are observed from around 1450 to 900 cm^{-1}; associated mainly with C–O stretching vibrations at 1183, 1057, 1133 cm^{-1}, while the peaks that bookend this middle zone can be attributed to C–H stretching of methyl (CH_3) and methylene (CH_2) deformations [28, 29]. A small band appearing around 600 cm^{-1}, which is slightly more pronounced in the composite scaffolds, can be attributed to the intrinsic vibration of the bond between the tetrahedral Fe-O of the iron oxide NPs [30].

Compression tests for the scaffolds, presented in Figure 2.4c), revealed an initial elastic behavior until 24.4 ± 6.1%, 24.6 ± 3.6%, and 22.81 ± 5.9% strain, followed by a plastic deformation region extending to 44.55 ± 6.8%, 54.75 ± 4.6% and 49.69 ± 7.1% until structural collapse for the pure PHBV, 10% and 20% Fe_3O_4 scaffolds, respectively, presenting only small differences among them. The corresponding Young's modulus values were 0.74 ± 0.04, 0.55 ± 0.08, and 0.54 ± 0.07 kPa, showing that the pure PHBV scaffolds exhibit slightly higher mechanical stiffness than their composite counterparts. This reduction in stiffness may arise from the heterogeneous distribution of Fe_3O_4 NPs, which can introduce microstructural discontinuities and weak interfacial adhesion between the polymer and magnetic NPs.

For the VSM measurements (Figure 2.4 d)), two samples of each composite scaffold were analyzed to evaluate possible variations in NP concentration between different syntheses. The hysteresis curves present the typical superparamagnetic behavior, with magnetization increasing with the applied magnetic field until saturation. Pure Fe_3O_4 NPs (shown in the inset) possess a saturation magnetization (M_s) of 72.8 $emu.g^{-1}$ at 17 kOe, while the scaffolds present approximate values of 5.1 $emu.g^{-1}$ (10% Fe_3O_4 scaffold samples) and 8.1 $emu.g^{-1}$ (20% Fe_3O_4 scaffold samples) at the same applied field value. While slight variations between samples of the same concentration are normal, the measurable Fe_3O_4 content in the composites was found to be 6.9 ± 0.5% and 11.1 ± 0.4%, respectively. This difference may be explained by the non-homogeneous dispersion of the NPs as seen in Figure 2.2, as well as potential NP loss during processing.

Figure 2.5 presents the data from contact angle and porosity analysis.

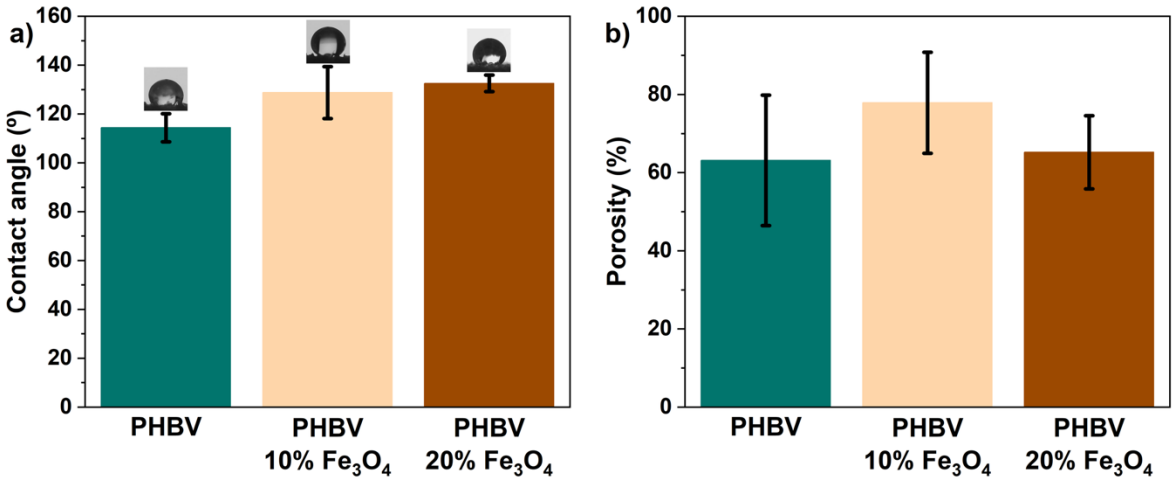


Figure 2.5. a) Contact angle and **b)** porosity values of the pure and composite PHBV scaffolds.

WCA measurements were performed to evaluate the hydrophobicity of the scaffolds, which reflects their surface wettability, a parameter that plays a vital role in cell adhesion, proliferation and differentiation [31]. The results are presented in Figure 2.5a). All samples exhibit hydrophobic behavior, as the measured contact angles exceed 90° (hydrophilic surfaces correspond to CA lower than 90°) [32]. Although some variability was observed, likely due to small irregularities of the surface caused by the deposition of the filament during the printing of the mold, higher WCA values were observed for the composite scaffolds. Specifically, values of 128.8 ± 10.6° and 132.5 ± 3.4° were obtained for the 10 and 20% NP loaded samples, respectively, both higher than the pure PHBV scaffolds. These higher values on the composites are commonly observed in the literature, as the inclusion of NPs can induce changes in surface morphology and enhance surface roughness, leading to higher contact angles [33].

Figure 2.5b) presents the porosity values obtained for the different scaffolds, which were 63.1 ± 16.7%, 77.9 ± 12.9%, and 65.2 ± 9.4% for the PHBV, 10% and 20% Fe_3O_4 PHBV scaffolds, respectively. Hence, the presence of NPs does not seem to particularly affect the overall scaffolds' porosity. The observed variability is likely due to minor differences in structural integrity, such as samples having a slightly higher number of obstructed pores than others.

2.3.3. Degradation studies

Figure 2.6 presents the results of scaffold degradation under static and dynamic conditions after 30 and 40 days.

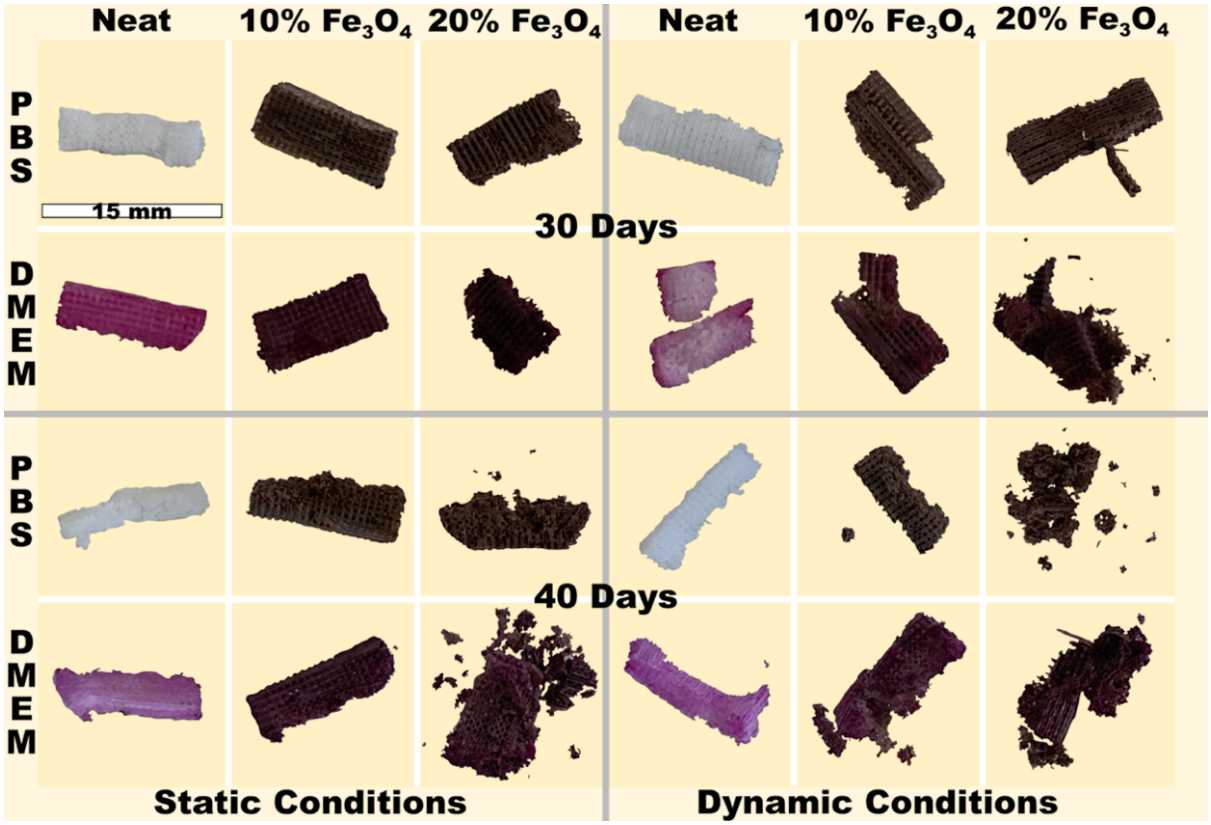


Figure 2.6. Representative images of the degradation suffered by the pure and composite PHBV scaffolds under static and dynamic conditions and when submerged in PBS and DMEM after 30 and 40 days.

Samples incubated in DMEM exhibited slightly higher degradation, likely due to the presence of additional organic and ionic compounds capable of chemically interacting with the scaffold material over time. The inclusion of NPs also appears to accelerate structural disintegration, as the pure PHBV scaffolds were overall less affected, while the addition of NPs progressively promoted higher breakdown of the structures over time. Moreover, structural breakdown seems to be aggravated under dynamic conditions, supporting the hypothesis that the incorporation of NPs can introduce localized mechanical weakness, which can make the scaffolds more susceptible to mechanical stress induced by the magnetic stimulation cycles.

2.3.4. Cell studies

2.3.4.1. Cytotoxicity studies

Indirect cytotoxicity studies of the scaffolds are presented in Figure 2.7. The results show that all PHBV scaffolds exhibited cell viability above the 70% threshold outlined by the ISO 10993-5 standard,

with values of 91.3 ± 1.4%, 87.0 ± 2.4% and 93.5 ± 3.4% for the pure, 10% and 20% Fe_3O_4 composite PHBV scaffolds, respectively. No statistically significant differences were detected between groups ($p > 0.05$). This result was anticipated, given that the constituent materials of these scaffolds had previously been shown to be biocompatible, although they were evaluated in film form rather than three-dimensional structures [34]. Thus, these results confirm that neither the materials nor the processing of the scaffolds induce cytotoxicity, further supporting their suitability for biomedical applications.

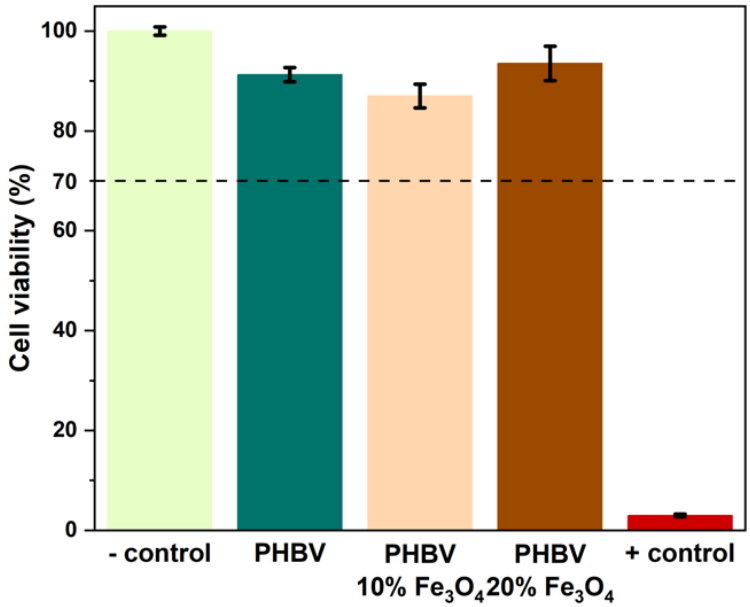


Figure 2.7. Indirect cytotoxicity assay of MC3T3-E1 preosteoblasts in contact with the pure and composite PHBV scaffolds.

2.3.4.2. Proliferation studies

Adhesion and proliferation under static and dynamic conditions were evaluated to assess the effect of magnetic stimulation on cell growth. Results are presented in Figure 2.8.

Cell proliferation was observed in all samples, under both static or dynamic conditions and despite NP content. The introduction of 10% Fe_3O_4 had little to no negative effect on cell proliferation, as average values under static conditions were similar to those of the pure scaffolds. In contrast, the 20% NP fraction scaffold presented lower proliferation compared with both the pure and 10% scaffolds, indicating that higher NP content may impair biological performance.

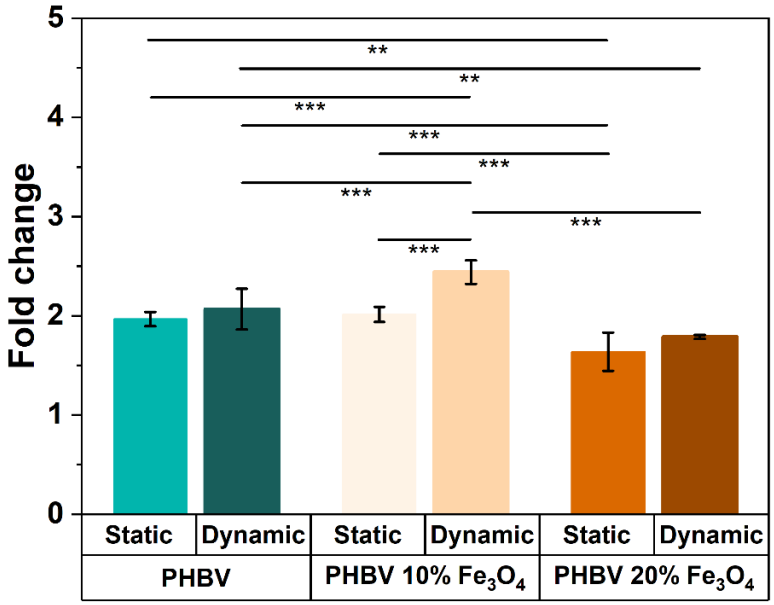


Figure 2.8. Cell proliferation of MC3T3-E1 preosteoblast culture after 7 days under static and dynamic conditions. The cell proliferation values of the pure and composite PHBV scaffolds were determined regarding the cells adhered on the material after 24 h adhesion, just before the first magnetic stimulus. The results are expressed as mean ± SD. **$p < 0.01$, ***$p < 0.001$.

The application of magnetic stimulation had a clear beneficial effect on the 10% Fe_3O_4 scaffolds, as proliferation values were significantly higher than those observed under static conditions, making this group the best-performing overall. In contrast, the 20% Fe_3O_4 scaffolds did not show significant differences between static and dynamic culture. Although proliferation did occur, its magnitude was considerably lower than in the other groups. This reduced performance may be due to increased susceptibility to environmental and interfacial stress at the NP/polymer boundary, as previously discussed. Microscopic structural damage may have already occurred after prolonged immersion in DMEM, weakening the scaffold and contributing to partial cell detachment, which would explain the lower proliferation observed for this formulation.

Pure PHBV scaffolds showed intermediate proliferation values, suggesting that their better structural integrity compared with the 20% composite scaffold supports moderate cell growth. However, they did not benefit from magnetic stimulation to the same extent as the 10% composite. Overall, these results indicate that moderate NP loading (10%) combined with magnetic stimulation most effectively enhances preosteoblast proliferation, highlighting its potential for bone regeneration applications.

To further verify the cells grew on the scaffolds, fluorescence microscopy images were acquired at T_0 and T_1 and are presented in Figure 2.9. The patterns described above are generally reflected in the

microscopy images: the 10% Fe_3O_4 samples show the clearest cell distribution in both conditions, as well as an overall increase in cell presence from the first timepoint to the last timepoint. Notably, the 20% sample under dynamic conditions shows evident cell presence at T_1, which may reflect sample-to-sample variability, as previously discussed, but also indicates that some 20% scaffolds may retain sufficient structural integrity to support cell growth. This observation suggests that the performance of the 20% group may be more heterogeneous than that of the other formulations.

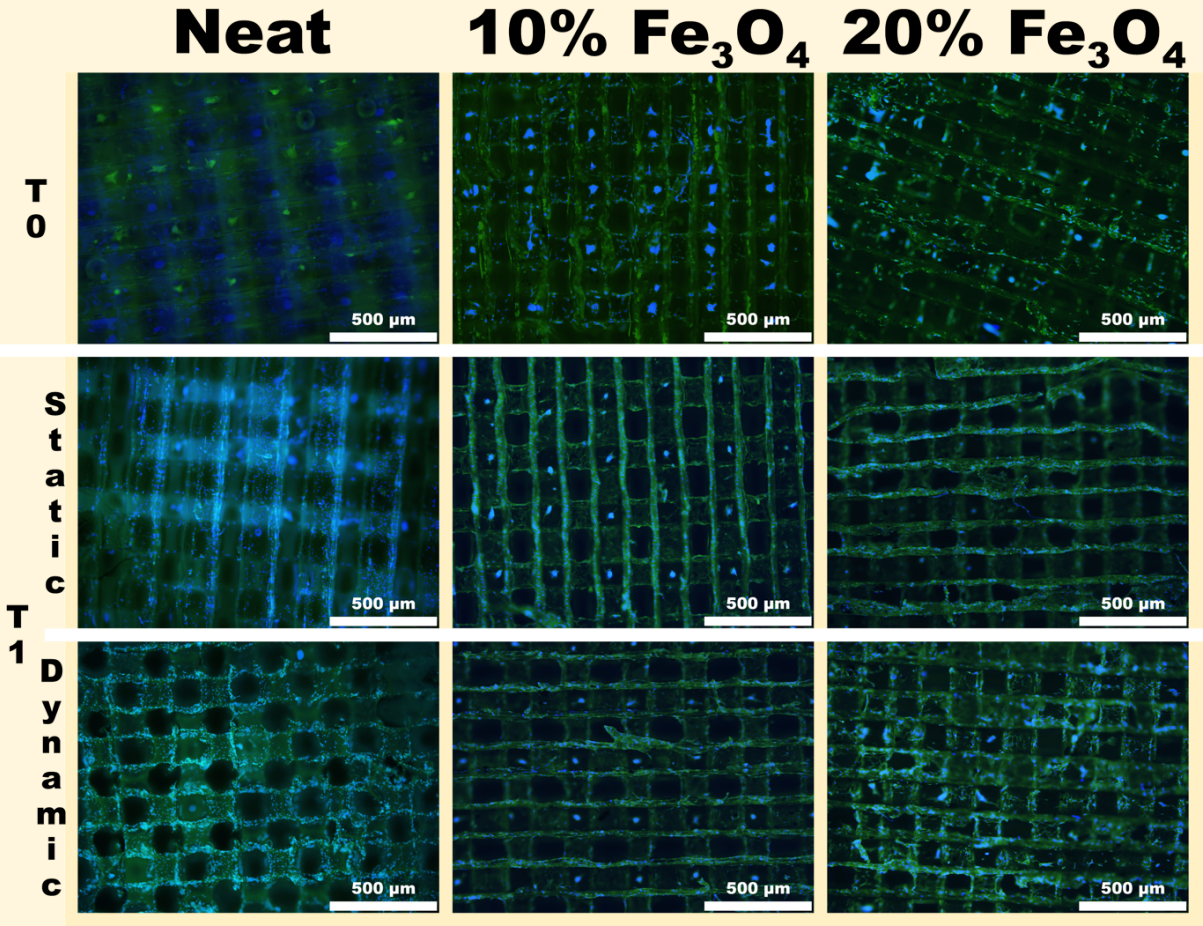


Figure 2.9. Fluorescence microscopy images of MC3T3-E1 cells adhered on the pure and composite PHBV scaffolds under static and dynamic conditions after 1 (T_0) and 7 days (T_1).

2.4. Conclusions

This study demonstrates the suitability of PHBV and PHBV composite scaffolds as electroactive microenvironments for MC3T3-E1 preosteoblast adhesion and proliferation, providing both proof of concept and the foundational basis for the development of multiresponsive scaffolds for bone TE.

The different scaffold formulations were thoroughly characterized regarding their physicochemical and mechanical properties. SEM and stereo microscopy imaging revealed well-defined structures across all samples, despite the less-than-ideal Fe_3O_4 NP dispersion. NP integration may have contributed to slightly higher pore area and perimeter, although squareness of the pores remained consistently high. Occasional pore obstruction seems to result from minor defects in the 3D-printed sacrificial molds, combined with the rapid evaporation of chloroform, which can cause nonhomogeneous infiltration of the polymer solution. DSC and FTIR-ATR analysis revealed the expected behavioral differences between pure and composite scaffolds, while mechanical testing indicated a slight reduction in Young's modulus values for the NP-loaded scaffolds, suggesting that the NP integration introduces microstructural discontinuities that weaken resistance to compressive loads. These mechanical differences are consistent with the degradation studies, which showed progressive structural breakdown in PBS and DMEM solutions over 30 and 40 days. Degradation seems to be more accentuated in the samples containing NPs and under magnetic stimulation, indicating that both NP-induced interfacial stress and cyclic magnetic actuation contribute to accelerated structural deterioration.

Cell studies revealed that all scaffold variations are non-cytotoxic and support preosteoblast proliferation. Although proliferation occurred across all groups, the 20% NP scaffolds consistently presented slightly lower performance than the other scaffolds, reinforcing the hypothesis that higher NP content compromises structural integrity and, consequently, cell adhesion and proliferation. Nevertheless, fluorescence microscopy images indicated some sample-to-sample variability, with clear presence still observed in the 20% dynamic group. The application of magnetic stimulus significantly enhanced cell proliferation in the 10% Fe_3O_4 scaffolds, making this formulation the most biologically responsive and the best-performing overall. Together, these results demonstrate that moderate NP loading (10%) combined with magnetic stimulation creates a favorable electroactive 3D microenvironment for bone-relevant cells, establishing a promising platform for the future development of multiresponsive, multifunctional scaffolds incorporating additional bioactive or actuation elements.

References

[1] S. Kumar *et al.*, "A comprehensive review of FDM printing in sensor applications: Advancements and future perspectives," *Journal of Manufacturing Processes,* vol. 113, pp. 152-170, 2024, doi: https://doi.org/10.1016/j.jmapro.2024.01.030.

[2] S. Li *et al.*, "Advances in hybrid fibers reinforced polymer-based composites prepared by FDM: A review on mechanical properties and prospects," *Composites Communications,* vol. 40, p. 101592, 2023, doi: https://doi.org/10.1016/j.coco.2023.101592.

[3] B. Mallikarjuna, P. Bhargav, S. Hiremath, K. G. Jayachristiyan, and N. Jayanth, "A review on the melt extrusion-based fused deposition modeling (FDM): background, materials, process parameters and military applications," *International Journal on Interactive Design and Manufacturing,* vol. 19, pp. 651–665, 2023, doi: https://doi.org/10.1007/s12008-023-01354-0.

[4] H. Iqbal, Q. Fernandes, S. Idoudi, R. Basineni, and N. Billa, "Status of Polymer Fused Deposition Modeling (FDM)-Based Three-Dimensional Printing (3DP) in the Pharmaceutical Industry," *Polymers,* vol. 16, no. 3, p. 386, 2024, doi: https://doi.org/10.3390/polym16030386.

[5] H. J. Aida, R. Nadlene, M. T. Mastura, L. Yusriah, D. Sivakumar, and R. A. Ilyas, "Natural fibre filament for Fused Deposition Modelling (FDM): a review," *International Journal of Sustainable Engineering,* vol. 14, no. 6, pp. 1988-2008, 2021, doi: https://doi.org/10.1080/19397038.2021.1962426.

[6] S. Nagarajan *et al.*, "Sacrificial mold-assisted 3D printing of stable biocompatible gelatin scaffolds," *Bioprinting,* vol. 22, p. e00140, 2021, doi: https://doi.org/10.1016/j.bprint.2021.e00140.

[7] B. Tandon, J. J. Blaker, and S. H. Cartmell, "Piezoelectric materials as stimulatory biomedical materials and scaffolds for bone repair," *Acta Biomaterialia,* vol. 73, pp. 1-20, 2018, doi: https://doi.org/10.1016/j.actbio.2018.04.026.

[8] G. Srinivasan, "Magnetoelectric Composites," *Annual Review of Materials Research,* vol. 40, no. 1, pp. 153-178, 2010, doi: https://doi.org/10.1146/annurev-matsci-070909-104459.

[9] S. Singh, A. K. Mohanty, T. Sugie, Y. Takai, and H. Hamada, "Renewable resource based biocomposites from natural fiber and polyhydroxybutyrate-co-valerate (PHBV) bioplastic," *Composites Part A: Applied Science and Manufacturing,* vol. 39, no. 5, pp. 875-886, 2008, doi: https://doi.org/10.1016/j.compositesa.2008.01.004.

[10] M. Avella, E. Martuscelli, and M. Raimo, "Review Properties of blends and composites based on poly(3-hydroxy)butyrate (PHB) and poly(3-hydroxybutyrate-hydroxyvalerate) (PHBV) copolymers," *Journal of Materials Science,* vol. 35, no. 3, pp. 523-545, 2000, doi: https://doi.org/10.1023/A:1004740522751.

[11] S. V. Chong and G. V. M. Williams, "Magnetoelectric effect in magnetostrictive-piezoelectric composites containing magnetite nanoparticles," *Sensors and Actuators A: Physical,* vol. 288, pp. 101-106, 2019, doi: https://doi.org/10.1016/j.sna.2019.02.003.

[12] L.-M. Wang *et al.*, "Magnetoelectric coupling in iron oxide nanoparticle—barium titanate composites," *Journal of Physics D: Applied Physics,* vol. 52, no. 6, p. 065301, 2019, doi: https://doi.org/10.1088/1361-6463/aaf13e.

[13] D. Erdem *et al.*, "Nanoparticle-Based Magnetoelectric $BaTiO_3$–$CoFe_2O_4$ Thin Film Heterostructures for Voltage Control of Magnetism," *ACS Nano,* vol. 10, no. 11, pp. 9840-9851, 2016, doi: https://doi.org/10.1021/acsnano.6b05469.

[14] C. Ribeiro, D. Correia, S. Ribeiro, M. Fernandes, and S. Lanceros-Mendez, "Piezo-and magnetoelectric polymers as biomaterials for novel tissue engineering strategies," *Mrs Advances,* vol. 3, pp. 1671-1676, 2018, doi: https://doi.org/10.1557/adv.2018.223.

[15] A. Reizabal *et al.*, "Silk fibroin magnetoactive nanocomposite films and membranes for dynamic bone tissue engineering strategies," *Materialia,* vol. 12, p. 100709, 2020, doi: https://doi.org/10.1016/j.mtla.2020.100709.

[16] T. S. Pinho *et al.*, "In vitro neuronal and glial response to magnetically stimulated piezoelectric poly(hydroxybutyrate-co-hydroxyvalerate) (PHBV)/cobalt ferrite (CFO) microspheres," *Biomaterials Advances,* Article vol. 159, 2024, Art no. 213798, doi: https://doi.org/10.1016/j.bioadv.2024.213798.

[17] Y. Zhang *et al.*, "Magnetoelectric Nanoparticles Incorporated Biomimetic Matrix for Wireless Electrical Stimulation and Nerve Regeneration," *Advanced Healthcare Materials,* vol. 10, no. 16, p. 2100695, 2021, doi: https://doi.org/10.1002/adhm.202100695.

[18] C. Bonnenfant, N. Gontard, and C. Aouf, "PHBV-based polymers as food packaging: Physical-chemical and structural stability under reuse conditions," *Polymer,* vol. 270, p. 125784, 2023, doi: https://doi.org/10.1016/j.polymer.2023.125784.

[19] L. N. Carli, J. S. Crespo, and R. S. Mauler, "PHBV nanocomposites based on organomodified montmorillonite and halloysite: The effect of clay type on the morphology and thermal and

mechanical properties," *Composites Part A: Applied Science and Manufacturing,* vol. 42, no. 11, pp. 1601-1608, 2011, doi: https://doi.org/10.1016/j.compositesa.2011.07.007.

[20] L. M. W. K. Gunaratne and R. A. Shanks, "Multiple melting behaviour of poly(3-hydroxybutyrate-co-hydroxyvalerate) using step-scan DSC," *European Polymer Journal,* vol. 41, no. 12, pp. 2980-2988, 2005, doi: https://doi.org/10.1016/j.eurpolymj.2005.06.015.

[21] V. Jost and H.-C. Langowski, "Effect of different plasticisers on the mechanical and barrier properties of extruded cast PHBV films," *European Polymer Journal,* vol. 68, pp. 302-312, 2015, doi: https://doi.org/10.1016/j.eurpolymj.2015.04.012.

[22] J. Bossu, N. Le Moigne, P. Dieudonné-George, L. Dumazert, V. Guillard, and H. Angellier-Coussy, "Impact of the processing temperature on the crystallization behavior and mechanical properties of poly[R-3-hydroxybutyrate-*co*-(R-3-hydroxyvalerate)]," *Polymer,* vol. 229, p. 123987, 2021, doi: https://doi.org/10.1016/j.polymer.2021.123987.

[23] H.-y. Yu, Z.-y. Qin, and Z. Zhou, "Cellulose nanocrystals as green fillers to improve crystallization and hydrophilic property of poly(3-hydroxybutyrate-co-3-hydroxyvalerate)," *Progress in Natural Science: Materials International,* vol. 21, no. 6, pp. 478-484, 2011, doi: https://doi.org/10.1016/S1002-0071(12)60086-0.

[24] W. Noohom, K. S. Jack, D. Martin, and M. Trau, "Understanding the roles of nanoparticle dispersion and polymer crystallinity in controlling the mechanical properties of HA/PHBV nanocomposites," *Biomedical Materials,* vol. 4, no. 1, p. 015003, 2009, doi: https://doi.org/10.1088/1748-6041/4/1/015003.

[25] K. C. C. C. Benini *et al.*, "Novel biodegradable composites based on PHBV: Effect of nanocellulose incorporation on the non-isothermal crystallization kinetic and structural parameters," *Polymer Composites,* vol. 40, no. 8, pp. 3156-3165, 2019, doi: https://doi.org/10.1002/pc.25164.

[26] S. Raho *et al.*, "Production of the Polyhydroxyalkanoate PHBV from Ricotta Cheese Exhausted Whey by Haloferax mediterranei Fermentation," *Foods*, vol. 9, no. 10, 2020, doi: https://doi.org/10.3390/foods9101459.

[27] A. Aramvash, S. Hajizadeh-Turchi, F. Moazzeni-zavareh, N. Gholami-Banadkuki, N. Malek-sabet, and Z. Akbari-Shahabi, "Effective enhancement of hydroxyvalerate content of PHBV in Cupriavidus necator and its characterization," *International Journal of Biological Macromolecules,* vol. 87, pp. 397-404, 2016, doi: https://doi.org/10.1016/j.ijbiomac.2016.03.002.

[28] M. Kansiz, H. Billman-Jacobe, and D. McNaughton, "Quantitative Determination of the Biodegradable Polymer Poly(β-hydroxybutyrate) in a Recombinant Escherichia coli Strain by Use of Mid-Infrared Spectroscopy and Multivariative Statistics," *Applied and Environmental Microbiology,* vol. 66, no. 8, pp. 3415-3420, 2000, doi: https://doi.org/10.1128/AEM.66.8.3415-3420.2000.

[29] G. M. Kim, G. H. Michler, S. Henning, H. J. Radusch, and A. Wutzler, "Thermal and spectroscopic characterization of microbial poly(3-hydroxybutyrate) submicrometer fibers prepared by electrospinning," *Journal of Applied Polymer Science,* vol. 103, no. 3, pp. 1860-1867, 2007, doi: https://doi.org/10.1002/app.25348.

[30] S. Husain, M. Irfansyah, N. Haryanti, S. Suryajaya, S. Arjo, and A. Maddu, "Synthesis and characterization of Fe_3O_4 magnetic nanoparticles from iron ore," in *Journal of Physics: Conference Series*, vol. 1242, no. 1: IOP Publishing, p. 012021, 2019, doi: https://doi.org/10.1088/1742-6596/1242/1/012021.

[31] S. Cai, C. Wu, W. Yang, W. Liang, H. Yu, and L. Liu, "Recent advance in surface modification for regulating cell adhesion and behaviors," *Nanotechnology Reviews,* vol. 9, no. 1, pp. 971-989, 2020, doi: https://doi.org/10.1515/ntrev-2020-0076.

[32] N. R. Visaveliya *et al.*, "Surface wrinkling and porosity of polymer particles toward biological and biomedical applications," *Advanced Materials Interfaces,* vol. 4, no. 24, p. 1700929, 2017, doi: https://doi.org/10.1002/admi.201700929.

[33] P. N. Manoudis and I. Karapanagiotis, "Modification of the wettability of polymer surfaces using nanoparticles," *Progress in Organic Coatings,* vol. 77, no. 2, pp. 331-338, 2014, doi: https://doi.org/10.1016/j.porgcoat.2013.10.007.

[34] T. Marques-Almeida, V. Correia, E. Fernández Martín, A. García Díez, C. Ribeiro, and S. Lanceros-Mendez, "Piezoelectric and Magnetically Responsive Biodegradable Composites with Tailored Porous Morphology for Biotechnological Applications," *ACS Applied Polymer Materials,* vol. 4, no. 12, pp. 8750-8763, 2022, doi: https://doi.org/10.1021/acsapm.2c01114.

CHAPTER 3

Magnetically responsive electroactive polymer composite microspheres

Based on the following publication (under submission):

Synthesis strategies for the development of piezoelectric and magnetoelectric microspheres

André S Macedo, Daniela M Correia, Clarisse Ribeiro, Senentxu Lanceros-Méndez

3.1. Introduction

Microspheres and NPs have been widely researched due to their diverse properties that depend on size and composition, with many industrial applications. Sunscreens contain titanium dioxide (TiO_2) and zinc oxide (ZnO) NPs, as they are colorless and have the ability to reflect or scatter UV light more efficiently than other particles [1]. Ferrofluids are very stable suspensions of MNPs in a liquid, creating a liquid phase behavior with superparamagnetic properties. When a magnetic field is applied, the magnetic moment of the NPs becomes aligned with the magnetic field direction leading to a macroscopic magnetization of the liquid. By controlling the flow properties of a ferrofluid and its position inside a device, applications such as dynamic seals and dampers have been developed based on these magnetically responsive suspensions [2].

The integration of NPs in hydrogels is also widely researched. For example, integration of Ag NPs into hydrogels of polymers such as PVA or PAA has been explored for use as antimicrobial coatings [3]. MNPs based on cobalt (Co) or nickel (Ni) have also been incorporated into hydrogels to form soft, magnetic field driven actuators for muscle-like applications, showing the magnetic properties of these NPs can be explored while being integrated into a hydrogel matrix [4].

Several methods can be employed for microsphere synthesis. Electrospraying allows the creation of microspheres from a polymer solution in a conductive solvent. By manipulating solution properties such as concentration, viscosity and surface tension, as well as processing parameters like flow rate, needle diameter, distance to the collector surface and the voltage applied, a continuous jet is formed, which subsequently breaks into droplets, resulting in microspheres with tunable size distributions [5]. Nanoprecipitation is based on the interfacial deposition of a solvent phase in a non-solvent phase leading to two unequilibrated liquid phases. As the solvent phase slowly mixes with the non-solvent phase below it, surface tension plays a role in sphere formation by affecting the diffusion rate of the polymer from one phase to the other [6]. Micro-sized particles can also be prepared by the related sol–gel method, which employs an oil/polymer solution emulsion with the aid of a surfactant, similarly using solvent and non-solvent phases. The type of non-solvent, surfactant, polymer concentration, and solution ratio influence the size and shape of the particles obtained [7].

Two of these methods were used to prepare microspheres with different combinations of polymers and MNPs.

3.2. Materials and methods

3.2.1. Materials

PVDF product reference Solef 1010 was acquired from Solvay (Solvay NV/SA, Brussels, Belgium). PHBV product reference PHI 003 was the same used in the previous chapter. Dimethylformamide (DMF), tetrahydrofuran (THF) and chloroform were all acquired from Merck (Merck KGaA, Darmstadt, Germany). Iron(II,III) oxide (Fe_3O_4, 30 nm) and cobalt ferrite ($CoFe_2O_4$, 35-55 nm) NPs were purchased from Nanoamor (Nanostructured & Amorphous Materials, Inc., Katy, TX, USA).

3.2.2. Morphological and magnetic properties characterization

For SEM analysis, samples were previously coated with a thin gold layer by magnetron sputtering using a Polaron SC502 (Quorum Technologies Ltd, Lewes, East Sussex, England). Morphology was observed using a Hitachi S-4800 (Hitachi High-Technologies Corporation, Tokyo, Japan) with a 5 kV beam acceleration voltage. ImageJ software was used to determine the diameters of the microspheres, which are reported in the form of histograms or as the mean ± SD of 100 measurements from each sample.

VSM was carried out using a MicroSense EZ7 (KLA Corporation, Lowel, Massachusetts, United States of America) magnetometer. An applied field from -20 to 20 kOe allowed the measurement of the magnetic hysteresis loop until magnetization saturation. $CoFe_2O_4$ filler content in the microspheres was determined using Equation 2.2 from Chapter 2, section 2.2.4.

3.2.3. PHBV, Fe_3O_4@PHBV and $CoFe_2O_4$@PHBV microsphere preparation

PHBV and Fe_3O_4@PHBV microspheres were produced based on an oil-in-water emulsion method [8]. PHBV was dissolved in chloroform at a concentration of 5% (w/v) using magnetic stirring at 60 °C. For Fe_3O_4@PHBV, 10% (w/w) Fe_3O_4 NPs were dispersed in chloroform using ultrasound for 1 h, then mixed and added to a previously dissolved 1% (w/v) PVA solution in ultrapure (UP) H_2O at a v/v ratio of 1:10 in a volumetric flask. The suspension was mechanically stirred at 1000 rpm for 24 h at RT to allow the solvent to evaporate and stabilize the emulsion. After this period, the same amount of UP H_2O was added to wash the microspheres, stirring for an additional 2 h. The suspension was then transferred to a beaker and left undisturbed for 24 h for the microspheres to precipitate, excess solution was discarded, and the remnant was dried for 48 h in a drying oven at 37 °C to recover the microspheres.

3.2.4. Fe_3O_4@PVDF microsphere preparation

PVDF 1010 was dissolved in DMF at a concentration of 5% w/v under mechanical stirring. A 10% (w/w) fraction of Fe_3O_4 NPs was dispersed using ultrasound for 1 h in THF at a volume corresponding to the final solution ratio (85:15 DMF/THF v/v), which was then added to the dissolved PVDF solution and stirred for 10 min. The solution was then transferred to a plastic syringe capped with a 22-gauge needle with an inner diameter of 0.5 mm, placed in a syringe pump with the tip positioned at 20 cm distance from the collector. Flow rate was set at 0.3 $mL.h^{-1}$ and a voltage of 18 kV was used.

3.3. Results and discussion

3.3.1. PHBV and Fe_3O_4@PHBV microspheres

Figure 3.1 shows SEM images of the PHBV and Fe_3O_4@PHBV emulsion samples.

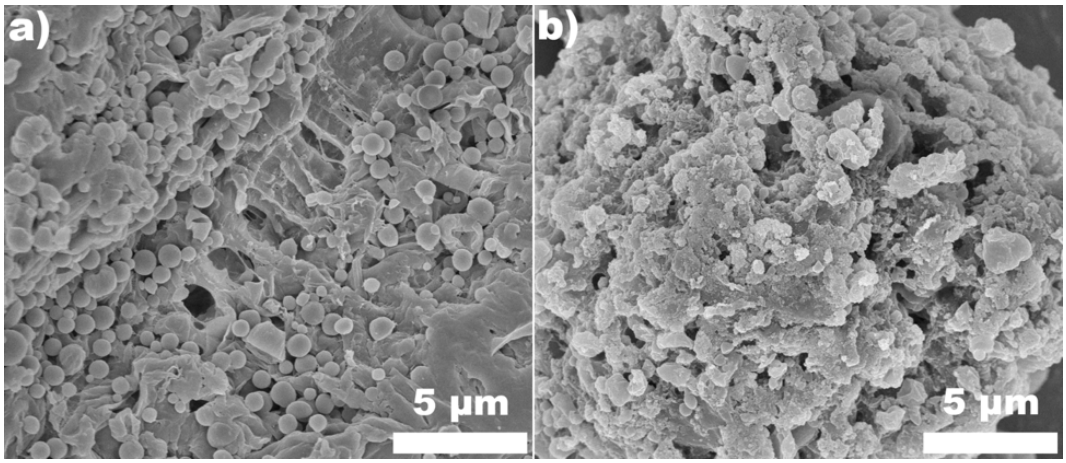


Figure 3.1. SEM images of **a)** PHBV and **b)** Fe_3O_4@PHBV microspheres prepared using an emulsion technique.

Figure 3.1a) shows successful PHBV microsphere formation with an average diameter of 583 ± 167 nm, although many appear encrusted in what might be debris of PVA. Repeated washing might remove these debris, freeing the microspheres. Fe_3O_4@PHBV microspheres (Figure 3.1b)) did not fully form or disperse properly, with only minor sphere formation embedded in large aggregates. This method was adapted from a previously developed protocol, and while using higher PHBV (compared to 3%) and PVA (compared to 0.5%) concentrations did produce smaller aggregates (not illustrated), proper microsphere formation was not achieved. The use of an adequate surfactant could help stabilize the emulsion and improve results.

3.3.2. $CoFe_2O_4$@PHBV microspheres

In Figure 3.2, and although slight aggregation is present, microsphere formation is successfully achieved. Diameters range roughly from 500 nm to 1 μm, with average diameters of 793 ± 250 nm. While roundish, many appear to have collapsed to different degrees. Again, further washing could help release the spheres and remove excess PVA matrix.

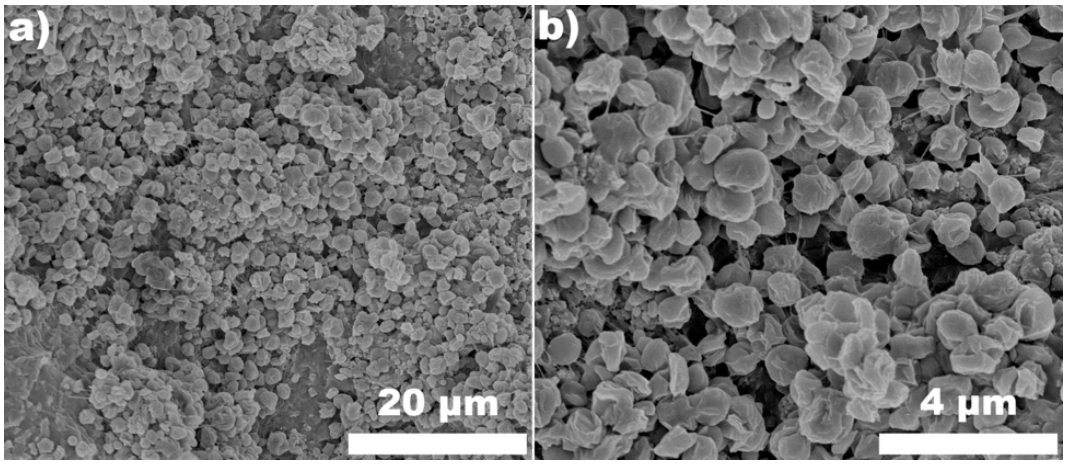


Figure 3.2. SEM images of $CoFe_2O_4$@PHBV microspheres prepared using an emulsion technique.

Figure 3.3 illustrates the analysis of the magnetic properties of the $CoFe_2O_4$@PHBV microspheres.

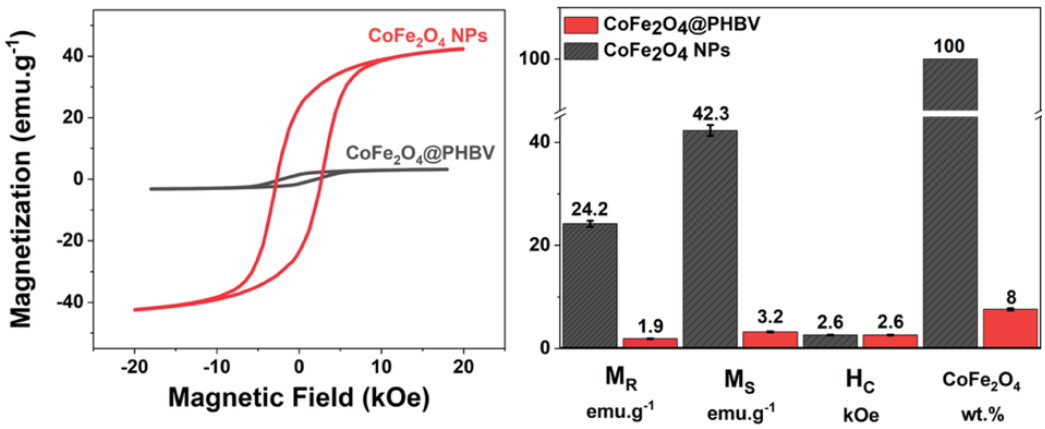


Figure 3.3. a) Room-temperature magnetic hysteresis cycles for the $CoFe_2O_4$@PHBV microspheres and $CoFe_2O_4$ nanoparticle and **b)** magnetic remanence (M_R), saturation magnetization (M_S), coercivity (H_C) and $CoFe_2O_4$ wt.% for the different samples.

Magnetic property evaluation shows both $CoFe_2O_4$ NPs and $CoFe_2O_4$@PHBV microspheres exhibit ferromagnetism at RT with blocked magnetic moments (Figure 3a)). The pure NPs present saturation

magnetization (M_s) of 42.3 emu.g^{-1} and 24.2 emu.g^{-1} remanence (M_r), while values of M_s of 3.2 emu.g^{-1} and 1.9 emu.g^{-1} M_r for the composite microspheres were obtained. Coercivity values are preserved (Figure 3.3b)), meaning the magnetic behavior of the magnetostrictive filler is preserved through the synthesis process. A degree of NP loss is expected during the synthesis due to aggregation and precipitation, which justifies the 8% w/w of $CoFe_2O_4$ determined for the composite microsphere sample.

3.3.3. Fe_3O_4@PVDF microspheres

SEM images of the electrosprayed microspheres are shown in Figure 3.4.

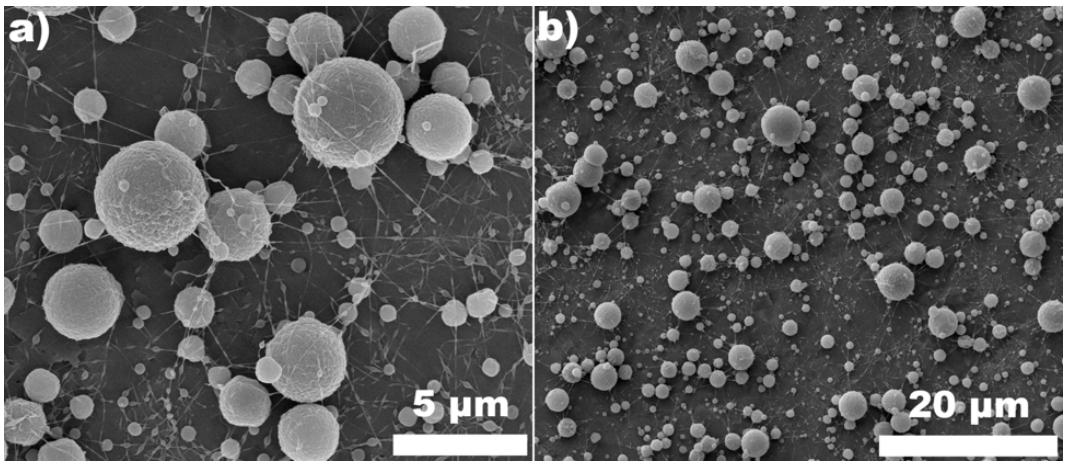


Figure 3.4. SEM images of Fe_3O_4@PVDF microspheres prepared using the electrospray technique.

The images show successful and homogeneously round microsphere formation. Fibers interconnecting the microspheres are also visible and are a consequence of the method used. When conditions are on the threshold of forming fibers or microspheres, both may occur. Size polydispersity is somewhat expected when using this technique, as vaporization of the solution at the Taylor cone is susceptible to surface tension interactions and droplets of different sizes can be formed. Hence, to better assess sample polydispersity, size data are presented in histogram form in Figure 3.5, showing that 80% of the sample had diameters under 1 µm and 60% (not shown) under 500 nm.

Fiber formation could potentially be minimized by carefully reducing the flow rate; however, the operational window for stable electrospray is often narrow. In addition, filtration may be employed to remove residual fibers and to enable size-based separation of the resulting samples.

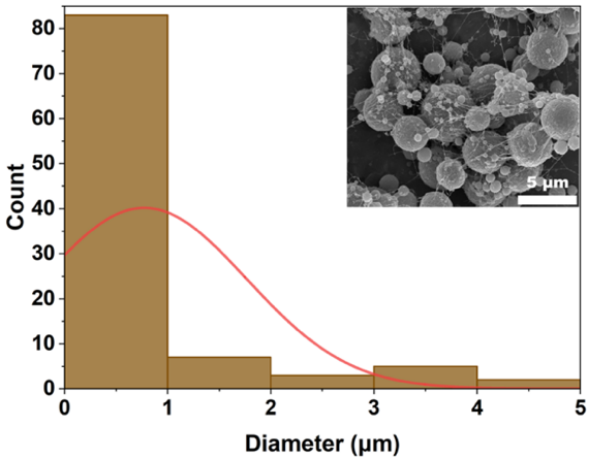


Figure 3.5. Histogram of Fe_3O_4@PVDF microsphere diameter by count.

3.4. Conclusions

Round, spherical Fe_3O_4@PVDF microspheres were successfully obtained using the electrospray technique. Although the resulting population is somewhat polydisperse, around 80% of the microspheres exhibit diameters below 1 μm, while a minority reaches sizes up to 5 μm; simple post-processing strategies, such as filtration or size-selective sedimentation, could effectively narrow this distribution. $CoFe_2O_4$@PHBV microspheres were also synthetized using an emulsion method and clear microsphere formation was achieved, although aggregation and partial embedding within residual PVA indicate that the emulsion requires further optimization, particularly regarding surfactant choice and washing efficiency. In contrast, Fe_3O_4@PHBV microspheres produced using the same protocol did not form properly, yielding predominantly large aggregates rather than defined spheres, highlighting that polymer–NP compatibility and emulsion stability must be reconsidered for this system. Despite these challenges, the successful fabrication of Fe_3O_4@PVDF microspheres provides a robust and reproducible platform that can be readily integrated into electroactive and magneto-responsive TE systems. These results establish a solid starting point for the development of multifunctional magneto-polymeric components, while identifying critical parameters that require refinement for PHBV-based formulations.

References

[1] G. J. Nohynek, J. Lademann, C. Ribaud, and M. S. Roberts, "Grey Goo on the skin? Nanotechnology, cosmetic and sunscreen safety," *Critical Reviews in Toxicology,* Review vol. 37, no. 3, pp. 251-277, 2007, doi: https://doi.org/10.1080/10408440601177780.

[2] G. Berselli, R. Vertechy, and G. Vassura, *Smart actuation and sensing systems: recent advances and future challenges*. Intech, p. 730, 2012, doi: https://doi.org/10.5772/2760.

[3] P. Thoniyot, M. J. Tan, A. A. Karim, D. J. Young, and X. J. Loh, "Nanoparticle–Hydrogel Composites: Concept, Design, and Applications of These Promising, Multi-Functional Materials," *Advanced Science,* vol. 2, no. 1-2, p. 1400010, 2015, doi: https://doi.org/10.1002/advs.201400010.

[4] R. Fuhrer, E. K. Athanassiou, N. A. Luechinger, and W. J. Stark, "Crosslinking metal nanoparticles into the polymer backbone of hydrogels enables preparation of soft, magnetic field-driven actuators with muscle-like flexibility," *Small,* vol. 5, no. 3, pp. 383-388, 2009, doi: https://doi.org/10.1002/smll.200801091.

[5] D. M. Correia *et al.*, "Electrosprayed poly (vinylidene fluoride) microparticles for tissue engineering applications," *RSC Advances,* vol. 4, no. 62, pp. 33013-33021, 2014, doi: https://doi.org/10.1039/C4RA04581E.

[6] A. S. Macedo *et al.*, "Tailoring electroactive poly(vinylidene fluoride-*co*-trifluoroethylene) microspheres by a nanoprecipitation method," *Materials Letters,* vol. 261, p. 127018, 2020, doi: https://doi.org/10.1016/j.matlet.2019.127018.

[7] D. M. Correia *et al.*, "Ionic Liquid-Based Materials for Biomedical Applications," *Nanomaterials,* vol. 11, no. 9, p. 2401, 2021, doi: https://doi.org/10.3390/nano11092401.

[8] L. Amaro *et al.*, "Tailored biodegradable and electroactive poly (hydroxybutyrate-*co*-hydroxyvalerate) based morphologies for tissue engineering applications," *International Journal of Molecular Sciences,* vol. 19, no. 8, p. 2149, 2018, doi: https://doi.org/10.3390/ijms19082149.

CHAPTER 4

Hydrogels

SUBCHAPTER 4.1

3D-printed hydrogels

Based on the following submitted publication:

Engineering Crosslinker-Free Sericin–Gelatin Hydrogels with Tunable Rheology for 3D Printing Applications

André S Macedo, Alaitz Etxabide, Teresa Carranza, Ricardo Brito-Pereira, Clarisse Ribeiro, Pedro Guerrero, Koro de la Caba, Senentxu Lanceros-Méndez

4.1.1. Introduction

Forty years after the first 3D printed part and thirty-seven years after the introduction of the first commercial stereolithography printer, the 3D Systems SLA 1 [1], 3D printing technologies have branched into a multitude of techniques. These range from the most common and affordable methods, like FDM, to more complex techniques able to achieve lower resolutions, such as two-photon polymerization (2PP), as well as those that use materials like metals or ceramics, which include selective laser sintering or melting [2]. Extrusion-based printing is one of the most widely used 3D printing techniques. The apparatus typically consists of one or more printing heads, which facilitate the combination of different materials within the same structure if desired. These heads can move along the *x*, *y*, and *z* axes while the dispenser extrudes the material in a controlled manner. Optional features may include the ability to heat or cool the material or printing bed during the process, as well as light sources for curing the printed structure [3]. These printed structures have found numerous biomedical applications, ranging from bone [4], skeletal muscle [5], and skin [6] regeneration to cancer research [7], the creation of 3D models for surgical preparation [8], and printable electronics [9]. In bioprinting, a solution composed of one or more biomaterials may be combined with living cells (commonly referred to as bioink) to construct 3D structures such as tissue scaffolds and implants, cells, organoids for 3D biological models, micro-organ chips for microphysiological platforms, and engineered living systems such as cellular machining and biorobots [10]. Moreover, one of the biggest challenges when devising 3D printing ink formulations is ensuring green part strength, which alludes to the integrity of bonded powders or plates before sintering or firing in ceramic processing. This demands the execution of a specific protocol, typically referred to as curing, during or after printing in order to achieve stable and functional structures, often through some form of crosslinking [11].

Gelatin is a protein derived from the partial hydrolysis of collagen. It is primarily obtained from bovine or porcine sources but can also be extracted from fish and, to an even lesser degree, other sources such as poultry. While it has applications in fields like cosmetics and forensic science, its most common use is as a gelling agent, thickener, stabilizer, or protective coating in the food industry [12]. Gelatin possesses the ability to form gels depending on parameters such as concentration and pH, and presents thermal reversibility: at 37 °C, the triple helix conformation of mammalian gelatin returns to a coiled state, converting the gel into the liquid state. To achieve more stable hydrogels, crosslinking is often employed [13]. As a hydrogel, gelatin has excellent hydrophilicity, biocompatibility, and biological fluid absorption

ability, making it valuable for various biomedical fields, such as drug release, wound dressing, cell culture, and scaffolds for TE [14].

Sericin and fibroin are the two composing proteins of silk, which are traditionally extracted from the cocoons of *Bombyx mori* (*B. mori*, commonly known as the silkworm, the larva of the silk moth). However, silk is also produced by specialized epithelial cells that line the glands of other members of the Lepidoptera order and Arachnida class [15]. Structurally, sericin presents as a sheath wrapped around the fibroin fibril, which comprises 15-35% of the silk fiber. It can be divided into outer, middle, and inner layers according to their water solubility. This is owed to a gradual decrease in hydrophilic AAs further inwards into the fiber. This composition makes the outer layers water soluble, allowing extraction by dissolution in hot water [16]. This extraction, typically referred to as degumming, may also involve acidic or basic solutions [17]. In the processing of silk in textile industries, degumming is usually employed to improve the spinning and dyeing processes. Hence, use of hot water degumming and the repurposing of sericin can have a major impact in terms of waste reduction, sustainability, and circular economy [18, 19]. Sericin also possesses great biocompatibility and biodegradability and has shown auspicious results in TE, supporting cell adhesion, promoting proliferation, preventing apoptosis, and even suppressing tumor activity [20]. Additionally, it has applications in drug release and as an antimicrobial agent [21].

This study aimed to develop 3D printable, biocompatible, and biodegradable hydrogels combining gelatin and sericin at different ratios to tune their printability and physicochemical properties. To achieve this, AA composition and rheological properties were first evaluated to assess the ability of the materials to gel and hence their printability. Printed samples were subjected to optical evaluation through image processing and data measurement acquisition to assess print quality and morphology. Further, interactions between the two proteins were evaluated, as well as the hydrogels' swelling and stability in PBS solution. To our knowledge, this is the first time these proteins have been combined to produce a 3D printable hydrogel without the use of crosslinkers or plasticizers, which previous studies have typically relied upon [22, 23].

4.1.2. Materials and methods

4.1.2.1. Materials

B. mori cocoons were supplied by APPACDM (Castelo Branco, Portugal). Type A porcine skin gelatin (strength ≈270 bloom) was supplied by Sancho de Borja (Zaragoza, Spain). Type II water was obtained from an Autwomatic Plus 1 + 2, Wasserlab (Navarre, Spain).

4.1.2.2. Silk sericin extraction

B. mori cocoons were opened, cleaned, and cut into 1 cm^2 pieces. They were then put in a deionized water (diH_2O) solution at a concentration of 20 $g.L^{-1}$ and heated in an autoclave (AMARO 5000 HORIZONTAL, AJ Costa (Irmãos), Cacém, Portugal) at 120 °C for a 150 min cycle to dissolve the sericin. This sericin solution was extracted, frozen and freeze-dried (CHRIST Alpha 1–2 LDplus, Martin Christ, Germany) to achieve the sericin powder.

4.1.2.3. Hydrogel preparation

Sericin and gelatin hydrogels were prepared in three different sericin concentrations (0.75, 2.00 and 3.25% w/v), while gelatin concentration was 2% w/v for all samples. Hereafter, these samples will be referred to as SerGe1, SerGe2, and SerGe3, respectively. Both proteins were dissolved in water by heating at 60 °C for 30 min with stirring at 300 rpm. After, the sericin solution was then ultrasonicated (Model 3000513 from JP Selecta, Barcelona, Spain) for 15 min. Following this, the solutions were then mixed and magnetically stirred at 300 rpm and 60 °C for an additional 15 min, and then transferred to a 10 mL syringe. The mixture was stored at 4 °C until used.

4.1.2.4. Rheological assessment

A Thermo Scientific HAAKE RheoStress1 (Thermo Fisher Scientific Inc., Massachusetts, USA) was employed for the rheological measurements. A stainless-steel measuring plate P35 (ø 35 mm) was used, with a 0.1 mm gap between the stationary and rotating plates. The temperature was set at 21 °C, which was the same used later for 3D printing.

Shear stress sweeps from 0 to 1000 Pa were conducted at 1 Hz to assess the trends in the storage (G') and loss (G'') moduli to determine the linear viscoelastic region (LVR) of the hydrogels. A shear stress (τ_0) value of 0.2 Pa was used for subsequent rheological assessments of all samples.

Shear rate sweeps from 0.01 to 100 s^{-1} were conducted to analyze the apparent viscosity of the hydrogels. The obtained data were fitted to the power law model (Equation 4.1), frequently used to predict the printability of materials [24]:

$$\eta = K\dot{\gamma}^{n-1} \quad \textbf{(4.1)}$$

where η is viscosity, K the consistency index, $\dot{\gamma}$ the shear rate and n the flow index. A temperature sweep from 12 to 27 °C at a heating rate of 0.5 °C.min^{-1} was performed to analyze the viscosity of the hydrogels.

4.1.2.5. 3D printing

The 3D model, a cylindrical shape with a diameter of 19 mm and height of 1 mm, was created using Solid Edge software (Siemens, Munich, Germany). Ultimaker Cura 5.2.2 software (Ultimaker, Utrecht, The Netherlands) was used to slice the digital structures into G-Code files for printing. A conical 20G plastic nozzle with an inner diameter of 0.60 mm was used, with the printing bed temperature set at 15 °C and the layer height to 0.2 mm. For the SerGe1 and SerGe2 samples, a print speed of 5.5 mm.s^{-1} was applied, while for SerGe3, the print speed was set to 15mm.s^{-1}.

Before printing, the hydrogels were taken out from the refrigerator and left to warm up for 1 h until they reached RT. They were then loaded into the syringe extruder of a domoBIO 2A printer (DomoTek, Tolosa, Spain) and printed. After printing, the samples were left to dry overnight and then put in a dry oven at 37 °C to ensure complete water evaporation.

4.1.2.6. Morphological and physicochemical characterization

AA composition of the extracted sericin was determined in a Biochrom 30+ Amino Acid analyzer (Harvard Bioscience, Inc., Massachusetts, USA) physiological system.

Digital images were acquired using a setup composed of an Olympus Tough TG-6 camera (Olympus Corporation, Tokyo, Japan) and a PULUZ LED ring light studio box using a green background and the highest dimming setting (Dongguan Puluz Technology Limited, Guangdong, China). A millimetric ruler was used as a scale, while image processing and data measurement acquisition were carried out using ImageJ software to assess printing quality.

SEM was carried using a Hitachi S-4800 scanning electron microscope (Hitachi, Ltd., Tokyo, Japan) with an acceleration voltage of 5.0 kV was used to visualize the cross-sections of the printed samples. Prior to imaging, the samples were cut, mounted on metallic stubs, and coated with gold under vacuum in an argon atmosphere using a JFC-1100 fine-coat ion sputter (JEOL Ltd., Tokyo, Japan).

FTIR spectroscopy spectra of the hydrogels were obtained using an ALPHA II FTIR spectrometer (Bruker, Massachusetts, USA) equipped with an ATR crystal (ZnSe). A total of 32 scans were performed at 4 cm^{-1} resolution, with measurements recorded between 4000 and 750 cm^{-1}. Results are presented as wavenumber ± SD from three different measurements (n=3).

X-ray Diffraction (XRD) measurements were performed using a diffraction unit PANalytical X'pert PRO (Malvern Panalytical Ltd., Almelo, Netherlands), operating at 40 kV and 40 mA. The radiation was generated from a Cu-Kα source (λ = 1.5418 Å). The diffraction data were collected from 2θ values ranging from 1° to 50°, where θ represents the angle of incidence of the X-ray beam on the sample.

The swelling ratio was determined gravimetrically. Three samples from each ratio were weighed (DW) and placed in 2 mL of PBS solution (according to ASTM F-1635 standard) on a heating plate (IKA RO 15, IKA-Werke GmbH & Co. KG, Staufen, Germany) at 37 °C, using a covered 12-well multiwell plate. At 5, 10, 15, 30, 60 and 120 min, each sample was removed from the solution, drained of excess PBS, and weighed (SW) before reimmersion in PBS. The swelling ratio was calculated using Equation 4.2.

$$Swelling\ ratio\ (\%) = \frac{(SW - DW)}{DW} \times 100 \quad \textbf{(4.2)}$$

For degradation studies, the initial dry weight (W_I) of each sample was measured before immersion in 2 mL of PBS in a covered 12-well multiwell plate for 24 h at 37 °C. After this period, the samples were removed, dried, and weighed again (W_F). The remaining weight after degradation was calculated using Equation 4.3.

$$Remaining\ sample\ (\%) = \frac{W_F}{W_I} \times 100 \quad \textbf{(4.3)}$$

4.1.2.7. Cytotoxicity

Cytotoxicity evaluation was conducted using the same adaptation of the ISO 10993-5 standard test method previously described in Chapter 2, section 2.2.6. Three samples of SerGe3 were used.

4.1.3. Results and discussion

4.1.3.1. Amino acid composition

AA composition significantly influences the physicochemical properties of proteins, including their structure, water stability, and solubility. This is because some AAs are inherently hydrophobic, while others are hydrophilic [25]. The composition of the gelatin and sericin proteins utilized in the preparation of the hydrogels is shown in Table 4.1.

Table 4.1. Amino acid composition of the gelatin and sericin samples used for preparation of the hydrogels.

Amino acid	Gelatin (%)	Sericin (%)
Ala	11.55	5.30
Arg	5.19	3.00
Asp	4.74	16.38
Cys	0.14	0.45
Glu	7.94	4.39
Gly	29.21	15.76
His	0.48	1.26
Ile	0.88	0.54
Leu	2.51	1.25
Lys	2.93	2.61
Met	0.62	0.17
OHLys	0.70	0.01
OHPro	10.04	-
Phe	1.65	0.55
Pro	13.47	0.67
Ser	3.75	33.01
Thr	1.77	8.47
Tyr	0.45	3.25
Val	1.99	2.95

Regarding sericin, serine is the most abundant AA, closely followed by aspartic acid and glycine, which have similar concentrations. Together, serine and aspartic acid, both hydrophilic, constitute nearly 50% of the extracted sericin. When considering all hydrophilic AAs, they account for a total of 88.58%, while non-polar AAs make up 11.42% of the total composition. Additionally, the extraction method, as well as the origin and variety of cocoon, affects AA composition and consequently protein size [26]. Our results are similar to those of other authors that have previously used the same extraction method, resulting in low molecular weight sericin (≈12.0 kDa) [27]. In contrast, gelatin contains a higher proportion of hydrophilic AAs. Glycine alone constitutes nearly 30% of the protein, followed by hydroxyproline at 10%, resulting in a total of 57.30% hydrophilic AAs. Notably, hydroxyproline is the only AA that is not present in sericin, while all other AAs are held in common by both proteins. In addition to glycine and hydroxyproline, the AAs found in higher amounts in gelatin are proline, alanine, and glutamic acid. Glycine and alanine typically compose between a third and half of the AA composition of gelatin [28], with our sample totaling 40.76%. Taking the above into consideration, various inter- and intra-molecular

interactions can occur during protein folding, with the most common being hydrophobic interactions, electrostatic forces, van der Waals forces, and hydrogen bonding [29, 30].

4.1.3.2. Rheological properties of the hydrogels

Rheology studies provide information that allows a better understanding of a gel ability to be used as a 3D printing ink. The decrease in viscosity with increasing shear rates is known as shear thinning, which indicates the ability of a material to be extruded [31]. This behavior is observed in the shear rate sweeps (Figure 4.1a)) of all samples. Power law fittings with high correlation coefficients are presented alongside the data, with key values summarized in Table 4.2. No significant differences were found between the groups ($p > 0.05$). The fittings reveal that at lower shear rates, higher sericin concentrations in the samples correspond to higher viscosities, with values of approximately 77, 88 and 103 Pa.s for SerGe1, SerGe2 and SerGe3, respectively, at a shear rate of 0.04 s^{-1}. After this, the fittings for SerGe1 and SerGe2 start to converge as shear rates rise, with a viscosity of ≈0.3 Pa.s around 22 s^{-1}. At 100 s^{-1}, the viscosities of SerGe1 and SerGe2 are of approximately 0.08 Pa.s (although at this point, they begin to diverge again due to SerGe2's more accentuated slope), while SerGe3 exhibits a value of ≈0.17 Pa.s. Regarding the values of the fitting parameters, all samples possess *n* values between 0 and 1, which is another indicator of shear thinning behavior. Complex viscosity as a function of temperature, shown in Figure 4.1b), demonstrates that higher sericin content leads to increased viscosity but also greater sensitivity to temperature changes, as SerGe3 shows a more pronounced decrease in viscosity with rising temperatures. Nonetheless, all samples possess higher complex viscosity values at temperatures around 14-16 °C, peaking at values of approximately 15, 26 and 56 Pa.s.

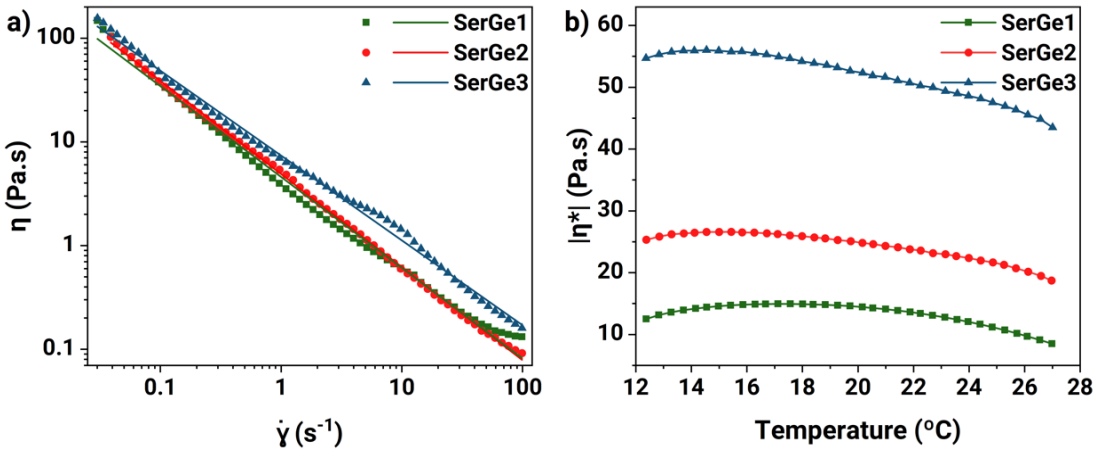


Figure 4.1. a) Shear rate and **b)** temperature sweeps of the 3D printed samples at different sericin:gelatin ratios.

Table 4.2. n (flow index) and K (consistency index) fitting parameters of the power law model applied. Values are presented as mean ± SD.

	n	K	R^2
SerGe1	0.062 ± 0.004	9.666 ± 4.502	0.988 ± 0.005
SerGe2	0.064 ± 0.000	6.436 ± 1.188	0.997 ± 0.001
SerGe3	0.110 ± 0.051	8.994 ± 1.325	0.996 ± 0.001

4.1.3.3. Morphology of the 3D printed samples

Images from each of the printed samples are presented in Figure 4.2. Although all samples show overall good definition, confirming the printability of all formulations, SerGe2 samples seem to show the best shape fidelity.

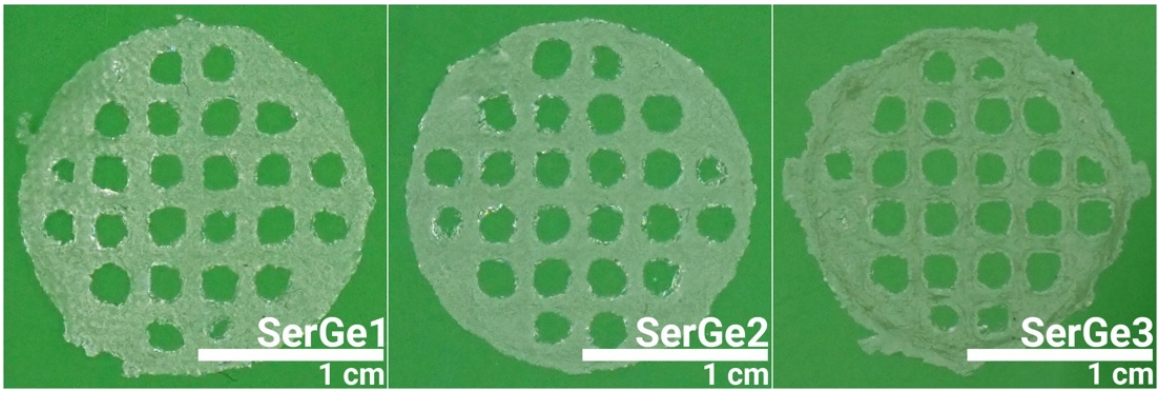


Figure 4.2. Digital photography images of the hydrogels at different sericin:gelatin ratios.

The corresponding average values for the void and line widths are presented in Table 4.3. As can be seen, the void areas and the line width of the samples were affected due to the action of surface tension of the water in the hydrogel, with SerGe2 samples showing the highest void area and the lowest line width.

Table 4.3. Averages for the areas of the central voids and the width of the printed lines in-between at different ratios of composition (sericin:gelatin) and corresponding values of the printable design (for comparison). Values are presented as mean ± SD.

Sample	Average void area (μm²)	Average line width (μm)
SerGe1	242 ± 68	1205 ± 257
SerGe2	285 ± 54	989 ± 169
SerGe3	252 ± 70	1187 ± 289

SEM images of the cross-sections of 3D printed samples are presented in Figure 4.3. As can be seen, all samples show rough flake-like but homogenous structure, indicating a good compatibility between both proteins, as previously observed at macroscopic scale.

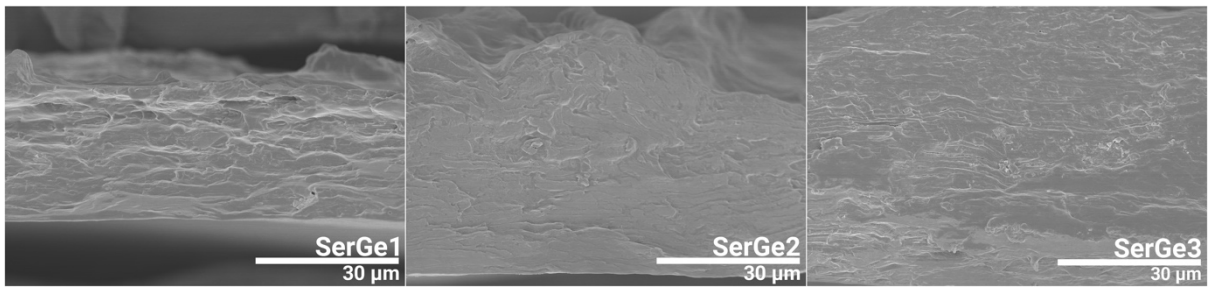


Figure 4.3. SEM images of the cross-section of the 3D printed samples with different sericin:gelatin ratios.

4.1.3.4. Physicochemical properties

FTIR and XRD analyses were carried out (Figure 4.4) to better understand the interactions between the two proteins, as well as the nature of the hydrogels in terms of crystallinity. FTIR spectra are presented in Figure 4a), where neat proteins are also shown. A wide band was observed between 3282-3272 cm^{-1}, associated with N–H stretching (amide A), which also overlaps with the O–H stretching band typically located in the same region. The band at 1628-1618 cm^{-1} corresponds to the stretching of C=O (amide I), while around 1538-1514 cm^{-1} N–H bending (amide II) is confirmed and amide III represents the C–N stretching at 1237-1235 cm^{-1} [32-35]. In the FTIR spectra of neat gelatin and sericin, the most apparent difference is the relative intensity between amide I and amide II bands, with higher peak intensity for amide I in the gelatin spectra. This trend can also be observed for SerGe1, while the difference between relative intensity of amide I and II decreases as sericin content increases, reaching a similar value for SerGe3. As for amide III band, this is wider in sericin than in gelatin, following also this trend in the 3D printed samples, where the widest amide III band is observed for SerGe3 samples.

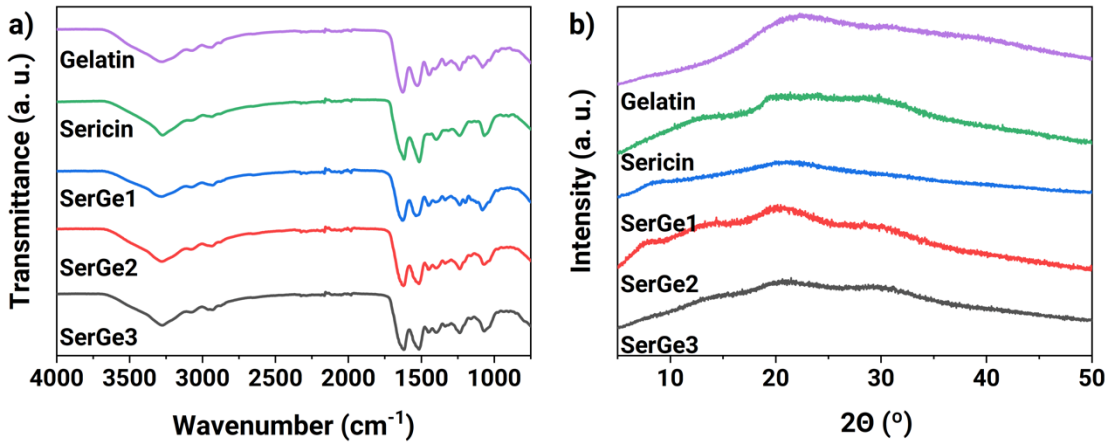


Figure 4.4. a) FTIR spectra and **b)** XRD patterns of neat proteins and 3D printed samples with different sericin:gelatin ratios.

Mean values for the frequency at which amide bands occur and their corresponding SDs are presented in Table 4.4. All bands, except amide III, arise at slightly higher frequency values in gelatin when compared to sericin. Consequently, as the sericin content increases in 3D printed samples, the frequency of amide bands decreases, except in the case of amide III band, where no significant difference is observed. These shifts happen as a consequence of interactions between the polar groups of both proteins, mainly by hydrogen bonding [36].

Table 4.4. Frequency values for amide A, I, II and III bands in the FTIR spectra of neat proteins and 3D printed samples with different sericin:gelatin ratios. Values are presented as mean ± SD.

Sample	Amide A (cm^{-1})	Amide I (cm^{-1})	Amide II (cm^{-1})	Amide III (cm^{-1})
Gelatin	3277.3 ± 1.2	1627.0 ± 0.0	1527.7 ± 1.2	1237.3 ± 0.5
Sericin	3272.7 ± 0.5	1618.7 ± 1.7	1514.0 ± 1.4	1237.7 ± 1.2
SerGe1	3282.0 ± 1.6	1626.3 ± 1.7	1537.7 ± 0.5	1235.7 ± 0.5
SerGe2	3279.3 ± 3.8	1622.0 ± 0.0	1516.0 ± 0.8	1236.3 ± 0.9
SerGe3	3276.3 ± 1.2	1619.3 ± 2.4	1515.3 ± 0.5	1236.3 ± 0.9

The XRD patterns in Figure 4.4b) show the amorphous character of neat proteins and 3D printed samples. As can be seen, there is a wide peak at 22.2° for gelatin, which becomes wider for sericin, presenting smaller shoulders at both lower and higher 2θ values. This wide peak with shoulders is also observed in the 3D printed samples. This amorphous nature is consistent with previous reports [37, 38].

4.1.3.5. Swelling and degradation studies

The swelling behavior (Figure 4.5) and degradation rate of the 3D printed samples were studied in PBS solution at 37 °C. The swelling behavior varies depending on the sericin content of the sample. In the first 10 min, SerGe1 and SerGe2 samples show similar swelling ability (≈ 1200%), while swelling for SerGe3 is considerably lower (less than 800%) and immediately reaches a plateau, where the swelling remains relatively stable until the end of the test (120 min). For SerGe2, swelling stabilizes after 15 min, maintaining the structure for 60 min before disintegration begins. SerGe1 samples, however, show a swelling over 1500% at 30 min but disintegrate shortly thereafter. These results suggest that SerGe3 provides 3D printed samples with higher stability and more controlled swelling, which would be favorable for a more sustained release of drugs or other bioactive compounds in biomedical applications.

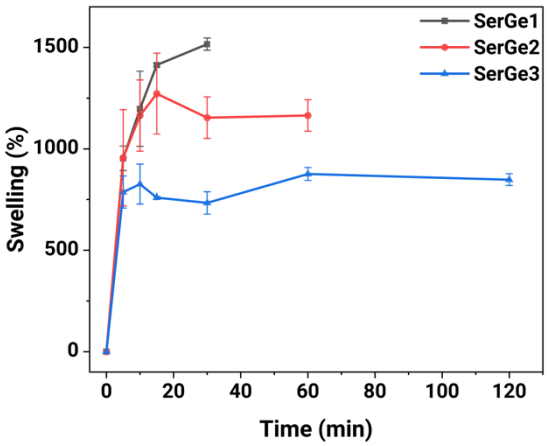


Figure 4.5. Swelling behavior of the 3D printed samples at different sericin:gelatin ratios when immersed in PBS solution at 37 °C.

Regarding the degradation studies in PBS solution, it was observed that after 24 h, SerGe1 and SerGe2 samples lost integrity and could not be properly recovered for weighing. In contrast, the SerGe3 samples lost 42.6 ± 6.5% of their initial mass, showing that a higher sericin content enhances the stability of the 3D printed samples. This finding agrees with the swelling results, where SerGe3 showed lower swelling ability while retaining its structure throughout the test. This behavior can be associated with the occurrence of hydrogen bonding [39] between the polar groups of both proteins, as shown by FTIR results, allowing SerGe3 to remain structurally stable for a longer period.

4.1.3.6. Cytotoxicity studies

Since SerGe3 demonstrates more controlled swelling and higher structural stability in solution, making it more promising for biological applications, this sample was chosen for the indirect cytotoxicity assays. These results are presented in Figure 4.6.

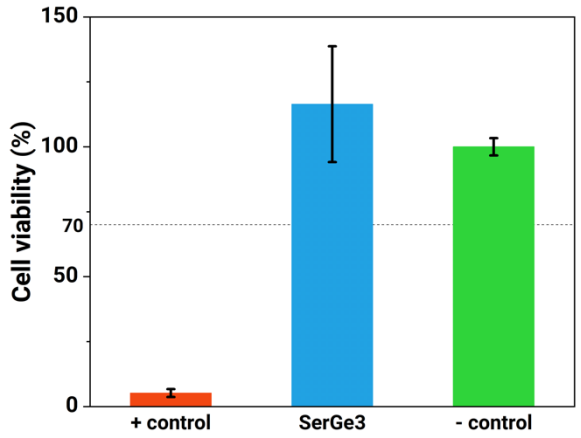


Figure 4.6. Indirect cytotoxicity assay of MC3T3-E1 preosteoblasts in contact with as-prepared extraction exposed to the SerGe3 hydrogel.

The results show that the SerGe3 sample exhibited cell viability above the 70% threshold outlined by the ISO 10993-5 standard, with a value of 116.4 ± 25.6%. The relatively high SD value may be attributed to impurities in the cocoon that resisted the extraction process. Nonetheless, these results confirm that the hydrogel does not induce cytotoxicity, thus demonstrating its suitability for biomedical applications.

4.1.4. Conclusions

Gelatin and sericin were combined to create hydrogels for 3D printing without any need of crosslinkers. Sericin concentrations of 0.75, 2 and 3.25% w/v and a gelatin concentration of 2% w/v were used to prepare the hydrogels. Generally, higher sericin content resulted in higher viscosity values, while all samples showed the shear thinning behavior needed for extrusion during 3D printing. The 3D printing accuracy was similar for all samples, with the best shape fidelity achieved for SerGe3 samples. XRD analysis showed that the 3D printed samples were amorphous, consistent with the structures of the neat proteins. FTIR analysis revealed some differences in the relative intensity between the amide I and II bands, as well as some frequency shifts in comparison to the FTIR spectra of neat proteins, indicating the formation of new interactions between gelatin and sericin. These interactions affect the swelling and

degradation behavior of the 3D printed samples, with SerGe3 samples showing the lowest swelling values and the highest structural integrity. As the sample with best integrity in solution, SerGe3 was selected for indirect cytotoxicity studies, which confirmed its non-cytotoxicity. This study shows that the combination of gelatin and sericin resulted in homogeneous and biocompatible hydrogels, with sericin promoting physical interactions with gelatin that enhance stability in 3D printed samples. Therefore, sericin content can be optimized to tailor the properties of the 3D printed structures for specific applications, including those in the biomedical field.

Although printing of the hydrogel was successful, attempts at using the hydrogel by itself, using higher masses and other methods (creating cylindrical hydrogels by casting the solution in a TCPS place is one example), were unsuccessful. A slow aggregation of sericin seemed to occur during drying, which took considerably longer in these bulk samples due to their reduced surface area to volume ratio. This aggregation may have caused a partial separation between gelatin and sericin, negating the intermolecular interactions that are expected to stabilize the network. Consequently, once these samples were placed in PBS at 37 °C, they quickly dissolved. Therefore, other gelatin-based hydrogel alternatives were explored, as detailed in the next subchapter.

References

[1] C. W. Hull, "The birth of 3D printing," *Research-Technology Management,* vol. 58, no. 6, pp. 25-30, 2015, doi: https://doi.org/10.5437/08956308X5806067.

[2] J. Li, C. Wu, P. K. Chu, and M. Gelinsky, "3D printing of hydrogels: Rational design strategies and emerging biomedical applications," *Materials Science and Engineering: R: Reports,* vol. 140, p. 100543, 2020, doi: https://doi.org/10.1016/j.mser.2020.100543.

[3] S. V. Murphy and A. Atala, "3D bioprinting of tissues and organs," *Nature Biotechnology,* vol. 32, no. 8, pp. 773-785, 2014, doi: https://doi.org/10.1038/nbt.2958.

[4] N. Ashammakhi *et al.*, "Advancing Frontiers in Bone Bioprinting," *Advanced Healthcare Materials,* vol. 8, no. 7, p. 1801048, 2019, doi: https://doi.org/10.1002/adhm.201801048.

[5] S. Ostrovidov *et al.*, "3D bioprinting in skeletal muscle tissue engineering," *Small,* vol. 15, no. 24, p. 1805530, 2019, doi: https://doi.org/10.1002/smll.201805530.

[6] A. Smandri, A. Nordin, N. M. Hwei, K.-Y. Chin, I. Abd Aziz, and M. B. Fauzi, "Natural 3D-printed bioinks for skin regeneration and wound healing: A systematic review," *Polymers,* vol. 12, no. 8, p. 1782, 2020, doi: https://doi.org/10.3390/polym12081782.

[7] R. Augustine *et al.*, "3D Bioprinted cancer models: Revolutionizing personalized cancer therapy," *Translational Oncology,* vol. 14, no. 4, p. 101015, 2021, doi: https://doi.org/10.1016/j.tranon.2021.101015.

[8] X. Xu *et al.*, "Multifunctional high-simulation 3D-printed hydrogel model manufacturing engineering for surgical training," *International Journal of Bioprinting,* vol. 9, no. 5, 2023, doi: https://doi.org/10.18063/ijb.766.

[9] H. Yuk, B. Lu, and X. Zhao, "Hydrogel bioelectronics," *Chemical Society Reviews,* vol. 48, no. 6, pp. 1642-1667, 2019, doi: https://doi.org/10.1039/C8CS00595H.

[10] W. Sun *et al.*, "The bioprinting roadmap," *Biofabrication,* vol. 12, no. 2, p. 022002, 2020, doi: https://doi.org/10.1088/1758-5090/ab5158.

[11] X. Xu *et al.*, "Additive manufacturing solidification methodologies for ink formulation," *Additive Manufacturing,* vol. 56, p. 102939, 2022, doi: https://doi.org/10.1016/j.addma.2022.102939.

[12] S. Sultana, M. E. Ali, and M. N. U. Ahamad, "11 - Gelatine, collagen, and single cell proteins as a natural and newly emerging food ingredients," in *Preparation and Processing of Religious and Cultural Foods*, M. E. Ali and N. N. A. Nizar Eds.: Woodhead Publishing, pp. 215-239, 2018, doi: https://doi.org/10.1016/B978-0-08-101892-7.00011-0.

[13] J. Alipal *et al.*, "A review of gelatin: Properties, sources, process, applications, and commercialisation," *Materials Today: Proceedings,* vol. 42, pp. 240-250, 2021, doi: https://doi.org/10.1016/j.matpr.2020.12.922.

[14] B. Salahuddin, S. Wang, D. Sangian, S. Aziz, and Q. Gu, "Hybrid Gelatin Hydrogels in Nanomedicine Applications," *ACS Applied Bio Materials,* vol. 4, no. 4, pp. 2886-2906, 2021, doi: https://doi.org/10.1021/acsabm.0c01630.

[15] C. Vepari and D. L. Kaplan, "Silk as a biomaterial," *Progress in Polymer Science,* vol. 32, no. 8, pp. 991-1007, 2007, doi: https://doi.org/10.1016/j.progpolymsci.2007.05.013.

[16] J. Liu *et al.*, "Silk sericin-based materials for biomedical applications," *Biomaterials,* vol. 287, p. 121638, 2022, doi: https://doi.org/10.1016/j.biomaterials.2022.121638.

[17] T. Jia *et al.*, "Moisture Sensitive Smart Yarns and Textiles from Self-Balanced Silk Fiber Muscles," *Advanced Functional Materials,* vol. 29, no. 18, p. 1808241, 2019, doi: https://doi.org/10.1002/adfm.201808241.

[18] A. Gaviria, N. Jaramillo-Quiceno, A. Motta, and A. Restrepo-Osorio, "Silk wastes and autoclaved degumming as an alternative for a sustainable silk process," *Scientific Reports,* vol. 13, no. 1, p. 15296, 2023, doi: https://doi.org/10.1038/s41598-023-41762-6.

[19] S. R. Vaishnav and S. A. Singh, "Chapter 14 - Sericin, a by-product of the silk industry: extraction and applications," in *Value-Addition in Agri-food Industry Waste Through Enzyme Technology*, M. Kuddus and P. Ramteke Eds.: Academic Press, 2023, pp. 199-208.

[20] H. Xie *et al.*, "A Silk Sericin/Silicone Nerve Guidance Conduit Promotes Regeneration of a Transected Sciatic Nerve," *Advanced Healthcare Materials,* vol. 4, no. 15, pp. 2195-2205, 2015, doi: https://doi.org/10.1002/adhm.201500355.

[21] M. Shitole, S. Dugam, R. Tade, and S. Nangare, "Pharmaceutical applications of silk sericin," *Annales Pharmaceutiques Françaises,* vol. 78, no. 6, pp. 469-486, 2020, doi: https://doi.org/10.1016/j.pharma.2020.06.005.

[22] M. Jang, B. K. Park, J. S. Huh, and J. O. Lim, "Evaluation of Sericin Containing Gel as a Photoinitiator-Free Printable Biomaterial," *3D Printing and Additive Manufacturing,* vol. 6, no. 5, pp. 238-244, 2019, doi: https://doi.org/10.1089/3dp.2019.0044.

[23] C.-S. Chen *et al.*, "Three-Dimensionally Printed Silk-Sericin-Based Hydrogel Scaffold: A Promising Visualized Dressing Material for Real-Time Monitoring of Wounds," *ACS Applied Materials & Interfaces,* vol. 10, no. 40, pp. 33879-33890, 2018, doi: https://doi.org/10.1021/acsami.8b10072.

[24] Y. Hong *et al.*, "Additive Manufacturing of Shape Memory Thermoset Composites with Directional Thermal Conductivity," *Advanced Functional Materials,* vol. 34, no. 9, p. 2311193, 2024, doi: https://doi.org/10.1002/adfm.202311193.

[25] A. S. Silva *et al.*, "Silk Sericin: A Promising Sustainable Biomaterial for Biomedical and Pharmaceutical Applications," *Polymers,* vol. 14, no. 22, p. 4931, 2022, doi: https://doi.org/10.3390/polym14224931.

[26] R. I. Kunz, R. M. C. Brancalhão, L. d. F. C. Ribeiro, and M. R. M. Natali, "Silkworm Sericin: Properties and Biomedical Applications," *BioMed Research International,* vol. no. 1, p. 8175701, 2016, doi: https://doi.org/10.1155/2016/8175701.

[27] M. Yang, Y. Shuai, G. Zhou, N. Mandal, L. Zhu, and C. Mao, "Tuning Molecular Weights of Bombyx mori (B. mori) Silk Sericin to Modify Its Assembly Structures and Materials Formation," *ACS Applied Materials & Interfaces,* vol. 6, no. 16, pp. 13782-13789, 2014, doi: https://doi.org/10.1021/am503214g.

[28] K. B. Djagny, Z. Wang, and S. Xu, "Gelatin: a valuable protein for food and pharmaceutical industries," *Critical reviews in food science and nutrition,* vol. 41, no. 6, pp. 481-492, 2001, doi: https://doi.org/10.1080/20014091091904.

[29] W. E. Stites, "Protein–Protein Interactions: Interface Structure, Binding Thermodynamics, and Mutational Analysis," *Chemical Reviews,* vol. 97, no. 5, pp. 1233-1250, 1997, doi: https://doi.org/10.1021/cr960387h.

[30] K. M. Biswas, D. R. DeVido, and J. G. Dorsey, "Evaluation of methods for measuring amino acid hydrophobicities and interactions," *Journal of Chromatography A,* vol. 1000, no. 1, pp. 637-655, 2003, doi: https://doi.org/10.1016/S0021-9673(03)00182-1.

[31] A. Schwab, R. Levato, M. D'Este, S. Piluso, D. Eglin, and J. Malda, "Printability and Shape Fidelity of Bioinks in 3D Bioprinting," *Chemical Reviews,* vol. 120, no. 19, pp. 11028-11055, 2020, doi: https://doi.org/10.1021/acs.chemrev.0c00084.

[32] S. D. Frazier and W. V. Srubar III, "Evaporation-based method for preparing gelatin foams with aligned tubular pore structures," *Materials Science and Engineering: C,* vol. 62, pp. 467-473, 2016, doi: https://doi.org/10.1016/j.msec.2016.01.074.

[33] X. Zhang and P. Wyeth, "Using FTIR spectroscopy to detect sericin on historic silk," *Science China Chemistry,* vol. 53, pp. 626-631, 2010, doi: https://doi.org/10.1007/s11426-010-0050-y.

[34] D. C. C. Martínez, C. L. Zuluaga, A. Restrepo-Osorio, and C. Álvarez-López, "Characterization of sericin obtained from cocoons and silk yarns," *Procedia engineering,* vol. 200, pp. 377-383, 2017, doi: https://doi.org/10.1016/j.proeng.2017.07.053.

[35] N. Cebi, M. Z. Durak, O. S. Toker, O. Sagdic, and M. Arici, "An evaluation of Fourier transforms infrared spectroscopy method for the classification and discrimination of bovine, porcine and fish gelatins," *Food chemistry,* vol. 190, pp. 1109-1115, 2016, doi: https://doi.org/10.1016/j.foodchem.2015.06.065.

[36] M. Yooyod, G. M. Ross, N. Limpeanchob, N. Suphrom, S. Mahasaranon, and S. Ross, "Investigation of silk sericin conformational structure for fabrication into porous scaffolds with poly(vinyl alcohol) for skin tissue reconstruction," *European Polymer Journal,* vol. 81, pp. 43-52, 2016, doi: https://doi.org/10.1016/j.eurpolymj.2016.05.023.

[37] D. Gupta, A. Agrawal, H. Chaudhary, M. Gulrajani, and C. Gupta, "Cleaner process for extraction of sericin using infrared," *Journal of Cleaner Production,* vol. 52, pp. 488-494, 2013, doi: https://doi.org/10.1016/j.jclepro.2013.03.016.

[38] K. Boonpavanitchakul, N. Pimpha, W. Kangwansupamonkon, and R. Magaraphan, "Processing and antibacterial application of biodegradable sponge nano-composite materials of silver nanoparticles and silk sericin," *European Polymer Journal,* vol. 130, p. 109649, 2020, doi: https://doi.org/10.1016/j.eurpolymj.2020.109649.

[39] M. F. DeCamp, L. DeFlores, J. M. McCracken, A. Tokmakoff, K. Kwac, and M. Cho, "Amide I Vibrational Dynamics of N-Methylacetamide in Polar Solvents: The Role of Electrostatic Interactions," *The Journal of Physical Chemistry B,* vol. 109, no. 21, pp. 11016-11026, 2005, doi: https://doi.org/10.1021/jp050257p.

SUBCHAPTER 4.2

Hydrogel films and loading into scaffolds

Based on the following publication (under submission):

Polymeric composites loaded with crosslinked hydrogels as scaffolds for tissue engineering

André S Macedo, Alaitz Etxabide, Clarisse Ribeiro, Pedro Guerrero, Koro de la Caba, Senentxu Lanceros-Méndez

4.2.1. Introduction

Crosslinked hydrophilic polymer structures called hydrogels have a high capacity for absorbing water and other biological fluids. The linkage of polymer chains with the aid of crosslinking agents affects the physical properties of the polymer depending on the degree of crosslinking [1]. Hydrogels can also act as artificial ECMs with 3D network structures fabricated to provide microenvironments for cell adhesion, proliferation and migration, as well as to promote the exchange of nutrients and signaling molecules [2].

Among the various polymers used for hydrogel fabrication, gelatin stands out due to its biological origin, tunable physicochemical properties and cell-interactive motifs [3]. It is a soluble protein derived from the partial hydrolysis of collagen and a main constituent of the ECM in animal tissues (of porcine, bovine, fish and other origins), including skin, cartilage, and bone [4]. It is highly biocompatible and completely resorbable *in vivo*, inexpensive, and easily attainable. It also exposes ligands such arginine-glycine-aspartic acid tripeptide motifs (the RGD sequence) that promote cell attachment by integrin-mediated interactions, and target sites for cellular metalloproteinases (MPP) that promote *in vivo* biodegradation of gelatin and ECM remodeling [5].

To improve the mechanical and physicochemical stability of gelatin-based hydrogels, different crosslinking strategies have been developed, including photo-, chemical and carbodiimide-mediated approaches. One way of achieving crosslinking of biopolymers is by photo-crosslinking. Through the addition of photo active compounds and UV radiation, covalent bonds are formed. These include photoinitiators, which absorb UV irradiation and generate free radicals or ions for inducing crosslinking reactions; photosensitizers can absorb light and transfer electrons to a suitable photoinitiator and lead to free radical, cationic or anionic photopolymerization; lastly, photo-crosslinkers may act as a crosslinker coupled with photoinitiators or photosensitizers under UV irradiation[6]. Riboflavin, commonly known as vitamin B2, is a heterocyclic aromatic compound [7]. It is also a yellow-green fluorescent compound often employed for UV-induced crosslinking of biopolymers. Riboflavin absorbs light at wavelengths of 223, 267, 373 and 444 nm, subsequently decomposing into various byproducts depending on the conditions. For example, lumiflavin is formed in alkaline pHs, while lumicromum results from acidic or neutral conditions. Among photoactive compounds, riboflavin has gained particular attention as a natural, non-toxic and biocompatible photosensitizer for biological crosslinking. By forming covalent bonds with polymers such as gelatin, properties of the resulting hydrogel such as water solubility, water vapor permeability, mechanical properties and melting point can be manipulated [8, 9].

Another major strategy relies on chemical crosslinking. The MR, a type of chemical crosslinking, consists of a series of reactions starting with carbonyl and amino compounds that ultimately polymerize

to form melanoidin networks. This reaction is influenced by a number of factors including temperature, pH, reactant type, reactant concentration, buffer salts, and metal ions [10]. Widely used in the food industry, where the browning associated with the formation of melanoidin improves flavor profiles [11], it has also been exploited for other ends in research. As MR products show antimicrobial activity, ribose and lysine have been used to take advantage of this reaction's byproducts, incorporating them in low-density polyethylene film to make active packaging foils [12]. Fructose is a monosaccharide found in small amounts in fruit and honey. A hexose of chemical formula $C_6H_{12}O_6$, it differs from glucose by having a keto group in position 2 of its carbon chain, whereas an aldehyde group at position 1 of glucose's carbon chain can be found [13]. As such, it is susceptible to undergo the MR. The preparation of hydrogel films using the MR has also been studied using different elements, often with gelatin, in combination with the aforementioned fructose, but ascorbic acid [14] and lactose [15] as well.

In addition to photo- and sugar-mediated routes, carbodiimide coupling systems such as EDC and NHS are widely employed for protein crosslinking due to their efficiency and cytocompatibility. Protein crosslinkers usually possess reactive sites that target functional moieties like thiol, amine and carboxylic acid groups in the side chains of amino acid residues. They can be classified under two groups: non-zero length crosslinkers and zero length crosslinkers. Examples of the first, such as glutaraldehyde and polyepoxides, bridge the groups between adjacent polypeptides like free carboxylic acid/amino/hydroxyl groups. The latter work by forming covalent bonds between reactive groups including carboxylic acid and amines in proximity [16]. EDC and NHS are examples of these. This crosslinking system is biocompatible and non-cytotoxic, and significantly enhances the physicochemical properties of collagen [17]. N-substituted carbodiimide can interact with the carboxylic acid groups of gelatin to form a highly reactive O-acylisourea intermediate. NHS prevents the hydrolysis of this intermediate. The crosslinks (i.e., amide bonds) are generated within the gelatin through the nucleophilic attack reaction between the free amino groups and the NHS-activated carboxylic acid groups, with the release of water-soluble urea by-products [18].

In this chapter, gelatin was separately combined with fructose, riboflavin and EDC-NHS, and three different methods of crosslinking were tested to prepare hydrogel films and hydrogel-loaded 3D PHBV scaffolds. Different methods of crosslinking were used to study how they differ in aspects that may be more or less suitable for cell adhesion and proliferation.

4.2.2. Materials and Methods

4.2.2.1. Materials

For gelatin-riboflavin hydrogel synthesis, gelatin from porcine skin (270 Bloom, Type A) was obtained from Sancho de Borja S.L. (Zaragoza, Spain); for gelatin-fructose, gelatin from porcine skin (300 g Bloom, Type A); for gelatin-EDC-NHS, gelatin from porcine skin (180 g Bloom, Type A), D-(-)Fructose, (-)-riboflavin, 2-(N-morpholino)ethanesulfonic acid (MES), NaOH pellets were acquired from Merck (Darmstadt, Germany).

For scaffold synthesis and cell studies, the same materials and methodology from Chapter 2, sections 2.2.1 and 2.2.6, respectively, were used.

Type II water was obtained from an Elix Advantage 5 water purification system (Sigma-Aldrich, Darmstadt, Germany).

4.2.2.2. Preparation of 3D PHBV scaffolds

The 3D PHBV scaffolds were prepared using sacrificial mold casting, as described in Chapter 2, Section 2.2.2. Magnetic scaffolds now consisted of PHBV containing 25% (w/w) Fe_3O_4 NPs, instead of the 10 and 20% used previously.

4.2.2.3. Hydrogel preparation and loading into scaffolds

In this section, the different methods of crosslinking, film preparation and evolution of the methodology used for loading the hydrogels into the scaffolds are detailed. The scaffolds prepared are illustrated in Figure 4.7.

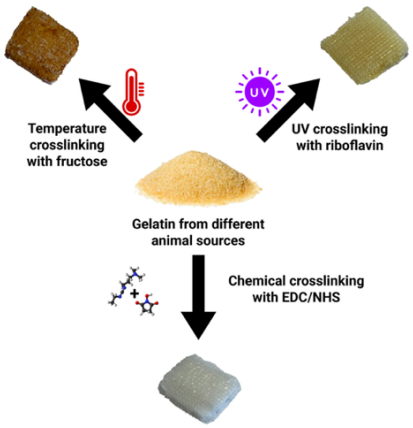


Figure 4.7. Illustration of the methods of crosslinking and crosslinkers combined with gelatin to prepare the different hydrogel-loaded PHBV scaffolds.

4.2.3.3.1. Gelatin-Riboflavin hydrogel

Gelatin at a concentration of 5% w/v and riboflavin at different concentrations (listed in Table 4.5), were dissolved in Type II water by heating at 60 °C for 30 min and stirring at 300 rpm. The scaffolds were immersed in the hot gelatin–riboflavin solution to allow infiltration before UV curing. Samples were immersed in the solution, removed from heating, and slowly agitated at 100 rpm for 30 min. They were then removed and exposed to UV light (4 lamps, 36 W, 370–405 nm, Domotek, Spain) for the desired period according to Table 4.5, then left to dry for 24 h at 37 °C.

Table 4.5. Synthesis parameters of the gelatin-riboflavin UV-crosslinked hydrogels.

Sample (NP when containing Fe_3O_4 nanoparticles)	Riboflavin concentration (% w/w)	UV exposure (h)
R1/R1NP	0.2	1
R2/R2NP	0.2	2
R3/R3NP	0.4	2

For the hydrogel films, 4.5 g of the solutions were dropped onto a plastic petri dish (60 mm diameter) and exposed to UV light. They were then moved to a drying oven for 24 h at 37 °C for final drying.

4.2.3.3.2. Gelatin-Fructose hydrogel

Gelatin and fructose at concentrations of 5% w/v and 20% w/w, respectively, were dissolved in Type II water by heating at 60 °C for 30 min with stirring at 300 rpm. Using these concentrations, four samples at different pH conditions and crosslinking temperatures were prepared according to Table 4.6.

Table 4.6. Synthesis parameters of the gelatin-fructose temperature-crosslinked hydrogels.

Sample (NP when containing Fe_3O_4 nanoparticles)	pH	Crosslinking temperature (°C)
F1/F1NP	7	80
F2/F2NP	10	80
F3/F3NP	10	110

The pH was adjusted to the desired value using 1 M NaOH solution, and the solutions were again stirred in the same conditions for 30 min. Loading of the gel into the scaffold was executed at this time. Samples were then immersed in the solution for 5 min to allow infiltration, removed, and frozen at -20 °C overnight. Following this, they were subjected to their corresponding temperature for crosslinking according to Table 4.6. After, hydrogel films were obtained by casting 4.5 g of solution into a plastic petri

dish (60 mm diameter), followed by drying at 37 °C for 24 h. The samples were then removed from the petri dishes and placed in an oven at their corresponding temperature for the final crosslinking step, according to the same table.

4.2.3.3.3. Gelatin-EDC-NHS hydrogel

MES buffer was dissolved at a concentration of 0.05 M in Type II water and the pH adjusted to 5.5. Gelatin at a concentration of 5% w/v was dissolved in this buffer by heating at 60 °C for 30 min with stirring at 300 rpm. After complete dissolution, the solution was removed from the heating plate and scaffolds were immersed in the solution and put in a vacuum chamber for 5 min to ensure complete infiltration and left to rest for 1 h. The scaffolds were then immersed in a 10 mM EDC and 5 mM NHS in MES buffer solution (prepared just before use) for 2 h. Finally, the samples were frozen at -80 °C for 24 h and freeze-dried in a Christ Beta 2-8 LDplus (Martin Christ, Osterode am Harz, Germany) for another 24 h.

4.2.2.4. Morphological and physicochemical characterization

Stereo microscopy, FTIR spectroscopy, mechanical compression analysis was carried out using the same methodology described in Chapter 2, section 2.2.4, again using 1x1x0.3 cm cuboid samples of hydrogel-loaded scaffolds.

Solubility of the Gelatin-Riboflavin films was evaluated from three samples of R1, R2, and R3 immersed in 2 mL of PBS in covered 12-well plates at 37 °C for 24 h. Their weights were measured before (IW, initial weight) and after (FW, final weight) immersion and subsequent drying, and values were calculated according to Equation 4.4:

$$Solubility\ (\%) = \frac{(IW - FW)}{IW} \times 100 \qquad \textbf{(4.4)}$$

Swelling of the Gelatin-Fructose hydrogel films and Gelatin-EDC-NHS hydrogels were carried from 3 samples, including each of F1, F2 and F3. Experiment was carried as described in Chapter 4, section 4.1.2.5, with the swelling ratio calculated using Equation 4.2 from the same section.

For degradation studies, 3 samples of Gelatin-Fructose and Gelatin-Riboflavin-loaded pure PHBV and composite scaffolds were put in 2 mL of PBS in a covered 24-well TCPS, at 37 °C. Samples were analyzed in both static and dynamic conditions in an 1 h on/11 h off cycle as used for the cell proliferation assay

described in Chapter 2, section 2.2.7. Remaining sample % was calculated according to Equation 4.3. The PBS medium from each sample was collected on days 7, 15, 22, 30 and 40 and subjected to UV–Vis absorption spectroscopy (Infinite M Nano, Tecan) at the 230–1000 nm range. Pure PBS medium was measured as background.

4.2.2.5. Cell studies

Both sides of the scaffolds were previously sterilized by exposure to UV for 1 h each and aseptically stored until used. MC3T3-E1 preosteoblast cells were used in cytotoxicity and proliferation tests under the same static and dynamic conditions as described in Chapter 2, section 2.2.5, with the exception of two aspects in the proliferation assays: a drop with cell concentration of 35×10^4 cells.mL^{-1} was used, and samples were evaluated after 1 (T_0) and 4 (T_1) days.

6 samples from each type of scaffold (pure PHBV polymer, pure containing Gelatin-EDC-NHS hydrogel, 25% (w/w) Fe_3O_4-loaded PHBV, and Fe_3O_4-PHBV containing hydrogel) evaluated for each state and timepoint.

The data were subjected to two-way ANOVA as described in Chapter 2, section 2.2.8.

Fluorescence microscopy was carried in the same way described in Chapter 2, section 2.2.9.

4.2.3. Results and discussion

4.2.3.1. Morphology of the hydrogel-loaded 3D printed samples

Stereomicroscopy images of the hydrogel-loaded 3D samples are presented in Figure 4.8. All hydrogels are immediately visibly adhered to the structures when compared to the stereo microscopy images of the PHBV scaffolds illustrated in Figure 2.2 of Chapter 2, confirming that infiltration of the hydrogel precursors into the porous matrix was successfully achieved.

In both riboflavin and fructose-crosslinking hydrogels, a progressive intensification of color saturation is evident from left to right. This indicates an increasing degree of crosslinking: from R1 to R2 as UV exposure time increases, from R2 to R3 as riboflavin concentration increases. In the case of the fructose-crosslinked hydrogels, the color intensification results from the higher pH used in F1 versus F2 (7 to 10) and from the increase of temperature exposition from F2 to F3 (80 to 110 °C). Local variations in color saturation within each sample can be observed, likely arising from regions of denser hydrogel accumulation, but also from irregular light source absorption and reflectance during imaging. F3 presents

the clearest example of this phenomenon, as darker orange regions are indicative of higher local concentrations of melanoidins formed via the MR.

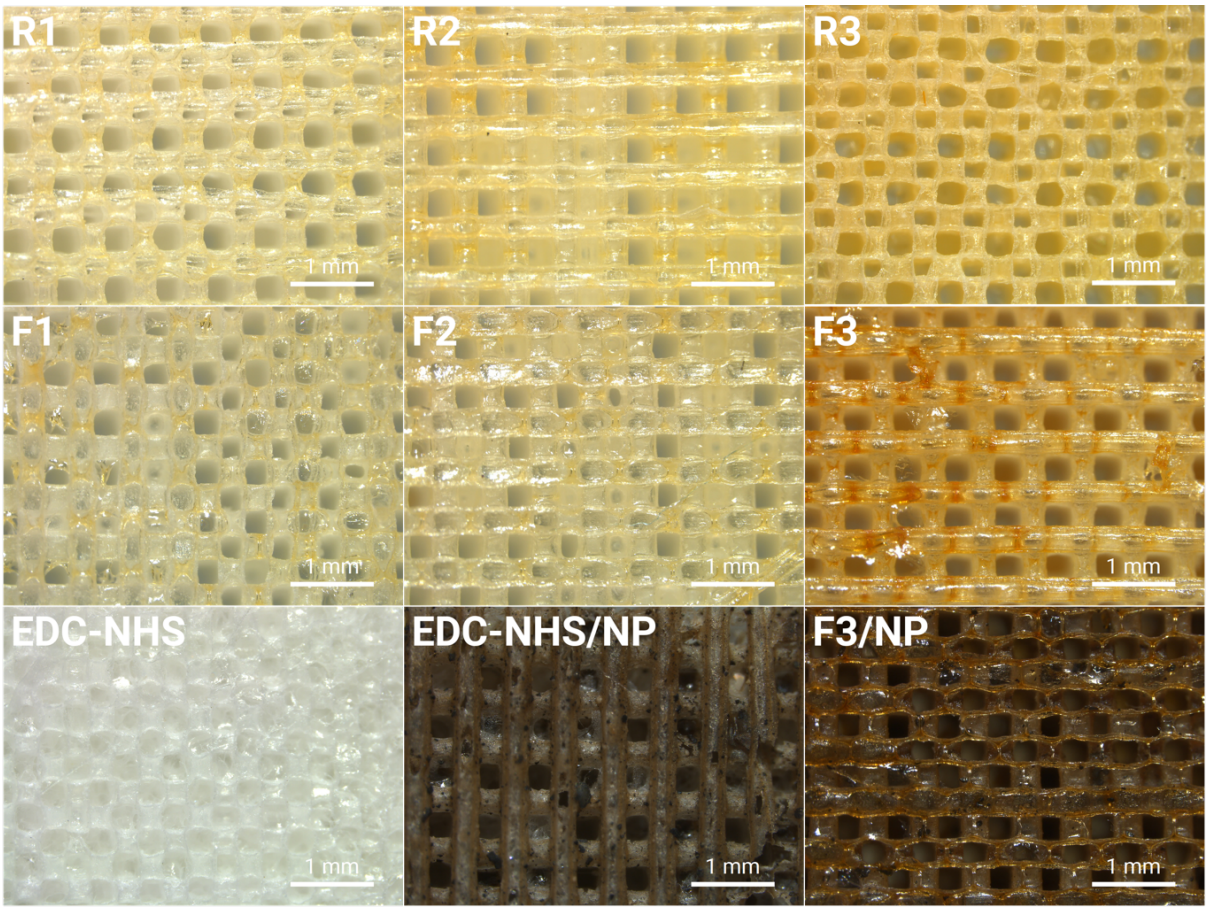


Figure 4.8. Stereo microscopy images of PHBV scaffolds loaded with gelatin hydrogels crosslinked by riboflavin (first row), fructose (second row and last position), and EDC-NHS (first and second images in the last row). (R1: 0.2% riboflavin, 1 h crosslinking; R2: 0.2% riboflavin, 2 h crosslinking; R3: 0.4% riboflavin, 2 h crosslinking; F1: pH 7, 80 °C; F2: pH 10, 80 °C; F3: pH 10, 110 °C).

The EDC-NHS-crosslinked hydrogel exhibits a milky white appearance, which contrasts strongly with the dark brown of the NP scaffolds and is also distinct from the orange tones of the fructose-based hydrogels. The hydrogel-loaded NP scaffolds are not shown here, as comparison between samples is clearer when using- the white pure-PHBV scaffolds as the reference background. The EDC-NHS sample also appears to have been more thoroughly infiltrated with hydrogel. Although the NP scaffold samples exhibited some regions devoid of hydrogel, the use of a vacuum pump likely facilitated its penetration into the scaffolds' pores. Some other samples, such as R2, also appear to have a reduced degree of hydrogel penetration, with less uniformity and completeness when compared with EDC-NHS. In other

areas of samples R3 and F3, for example, a predominantly surface-level coating over the PHBV filament layers seems to have occurred rather than full internal loading.

4.2.3.2. Compression studies

Stress-strain curves from mechanical compression of the hydrogel-loaded scaffolds are presented in Figure 4.9, with the PHBV scaffold without hydrogel included for comparison. Young's modulus, as well as the elastic and plastic regime data for each sample, are presented in Table 4.7.

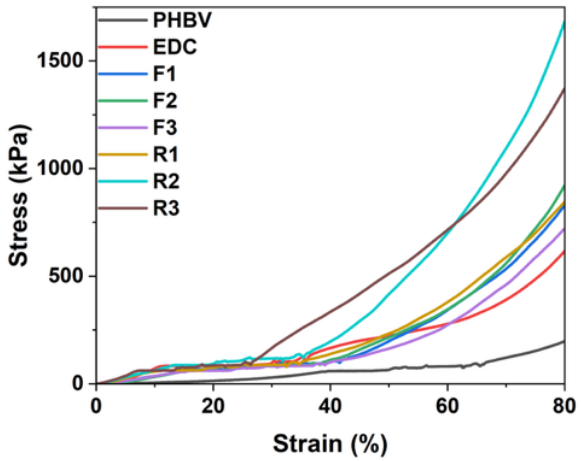


Figure 4.9. Mechanical compression stress-strain curves of the Gelatin-Riboflavin, Gelatin-Fructose and Gelatin-EDC-NHS-loaded PHBV scaffolds (R1: 0.2% riboflavin, 1 h crosslinking; R2: 0.2% riboflavin, 2 h crosslinking; R3: 0.4% riboflavin, 2 h crosslinking; F1: pH 7, 80 °C; F2: pH 10, 80 °C; F3: pH 10, 110 °C).

Two main aspects are immediately noticed from the data. First, the incorporation of hydrogels within the porous PHBV matrix significantly enhances mechanical strength, with Young's modulus values about one order of magnitude higher than those of the neat scaffolds. Second, the Gelatin-Riboflavin-loaded scaffolds are noticeably stiffer (≈8-9 kPa) compared to the Gelatin-Fructose ones (≈5 kPa). The elastic and plastic regions are smaller for the riboflavin series (7-15%) than for the fructose series (10-22%), suggesting a denser and more rigid crosslinking network. F3 possesses the lowest Young's modulus value among the fructose samples, which is consistent with the more pronounced browning observed in F3 relative to F1 and F2 (Figure 2.1). While stronger browning reflects a more advanced MR, this does not necessarily translate into higher stiffness. Instead, excessive MR-driven crosslinking can lead to the formation of a brittle and micro-fragile network with reduced mechanical performance. This mechanism explains why F3 shows increased brittleness, but a lower Young's modulus compared to the other fructose samples. The Gelatin-EDC-NHS-loaded scaffolds have Young's modulus values similar to F2,

although this formulation presents the longest plastic regime, at a value of ≈29%, suggesting a structure that is simultaneously crosslinked yet more deformable before failure.

Table 4.7. Young's modulus, elastic and plastic behavior values of the Gelatin-Riboflavin, Gelatin-Fructose and Gelatin-EDC-NHS-loaded PHBV scaffolds (R1: 0.2% riboflavin, 1 h crosslinking; R2: 0.2% riboflavin, 2 h crosslinking; R3: 0.4% riboflavin, 2 h crosslinking; F1: pH 7, 80 °C; F2: pH 10, 80 °C; F3: pH 10, 110 °C).

Sample	Young's modulus (kPa)	Elastic behavior up to	Plastic behavior up to
PHBV	0.7 ± 0.1	24.4 ± 6.1	44.6 ± 6.8
R1	7.8 ± 0.4	7.3 ± 1.2	16.8 ± 3.2
R2	7.8 ± 1.5	8.4 ± 2.6	16.4 ± 2.5
R3	9.2 ± 0.8	5.7 ± 0.7	13.7 ± 0.5
F1	4.7 ± 0.3	8.5 ± 2.1	20.5 ± 4.6
F2	5.6 ± 0.7	11.7 ± 2.2	19.9 ± 2.5
F3	3.9 ± 0.6	11.9 ± 1.8	23.8 ± 0.9
EDC-NHS	5.4 ± 0.5	7.1 ± 1.5	29.4 ± 3.8

4.2.3.3. Degradation studies

4.2.3.3.1. Solubility of the Gelatin-Riboflavin hydrogel films

Gelatin-riboflavin hydrogel films showed decreasing solubility in water (24 h) with increasing crosslinking time and riboflavin concentration: 95.4 ± 2.2%, 83.1 ± 1.8%, and 55.7 ± 2.3% of average mass loss for R1, R2, and R3, respectively (Table 4.8). This indicates that higher riboflavin content and exposure time lead to a higher crosslinking degree and, consequently, to lower solubility.

Table 4.8. Average mass loss of the Gelatin-Riboflavin hydrogel films after 24 h in water (R1: 0.2% riboflavin, 1 h crosslinking; R2: 0.2% riboflavin, 2 h crosslinking; R3: 0.4% riboflavin, 2 h crosslinking; F1: pH 7, 80 °C; F2: pH 10, 80 °C; F3: pH 10, 110 °C).

Sample	Average mass loss after 24 h (%)
R1	95.4 ± 2.2
R2	83.1 ± 1.8
R3	55.7 ± 2.3

4.2.3.3.2. Swelling of the Gelatin-Fructose hydrogel films

Figure 4.10 shows the mass variation of gelatin–fructose hydrogels over 30 days. Swelling and solubility strongly depend on pH and temperature during crosslinking. F1 (pH 7, 80 °C) dissolves completely within 24 h, while F2 (pH 10, 80 °C) resists longer, reaching a maximum swelling of ≈665% around day 4 before collapsing between days 7-9. In contrast, raising the temperature from 80 to 110 °C (F3), reduces both swelling capacity and solubility, with samples still stable in PBS solution after 30 days. This behavior is in line with what is expected: higher pH increases the availability of reactive amino groups [19], while elevated temperature accelerates the MR rate [20]. Gelatin-EDC-NHS samples present a maximum swelling of almost 90% by day 2 before disintegration around day 3.

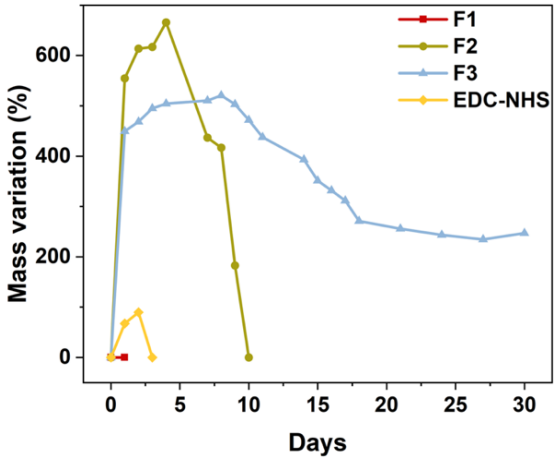


Figure 4.10. Mass variation of the Gelatin-Fructose hydrogel films and Gelatin-EDC-NHS hydrogels over 30 days (F1: pH 7, 80 °C; F2: pH 10, 80 °C; F3: pH 10, 110 °C).

4.2.3.3.3. Hydrogel-loaded scaffold mass loss

Figure 4.11 shows the average mass loss of Gelatin-Fructose and Gelatin-Riboflavin-loaded PHBV after 30 and 40 days under static and dynamic conditions.

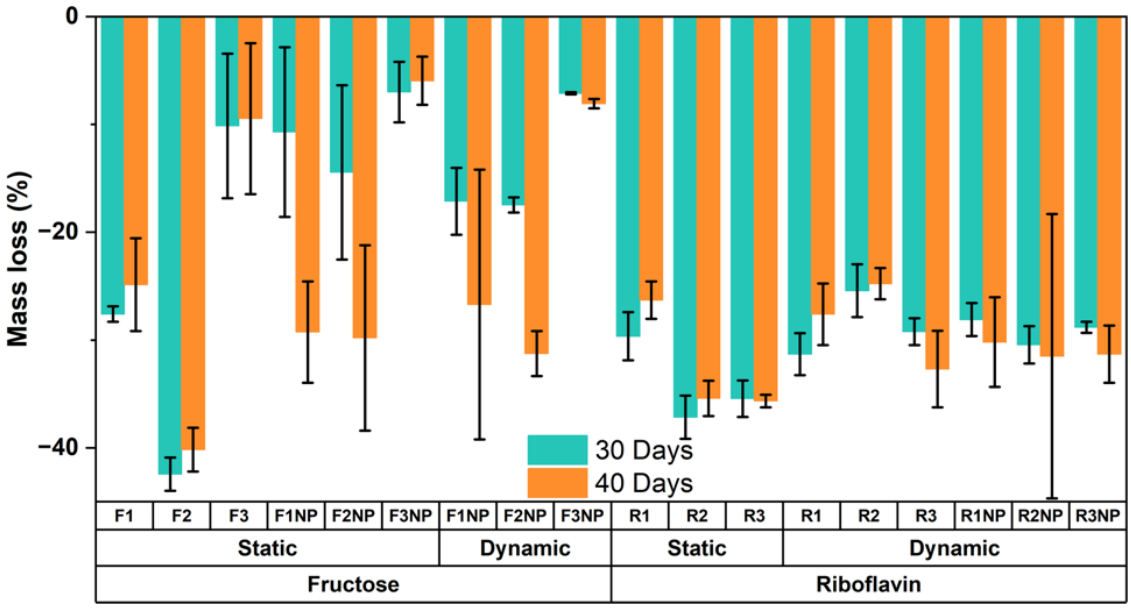


Figure 4.11. Average mass loss of PHBV scaffolds loaded with riboflavin and fructose-crosslinked gelatin hydrogels after 30 and 40 days, under static and dynamic conditions (F1: pH 7, 80 °C; F2: pH 10, 80 °C; F3: pH 10, 110 °C; R1: 0.2% riboflavin, 1 h crosslinking; R2: 0.2% riboflavin, 2 h crosslinking; R3: 0.4% riboflavin, 2 h crosslinking).

The most evident trend in the mass loss behavior of the composite scaffolds is that riboflavin-loaded samples consistently exhibit higher mass loss than their fructose-loaded counterparts, despite the absolute average values differing by approximately 10%. In addition, the F1, F1NP, F2, and F2NP samples display similarly high mass loss values. By the 30-day mark, these samples are expected to be nearly or fully dissolved, with mass loss values comparable to those observed in the riboflavin-loaded samples These values likely include partial degradation of the PHBV matrix itself as it becomes progressively exposed, contributing to the measured mass loss. Some samples, namely F1NP and F2NP, show a sharp increase in mass loss from day 30 to 40. However, the overall trend remains similar under both static and dynamic conditions, so the differences are most plausibly attributed to the presence of NPs and their interaction with the polymer-hydrogel system, rather than to the magnetic stimulation alone. It is interesting to observe that, under all conditions, F3 and F3NP present much smaller mass loss values (averaging less than 10%). This is consistent with the behavior observed for the F3 hydrogel film, indicating this sample possesses a much higher crosslinking degree than F1 and F2. This higher crosslinking density likely results in a more stable hydrogel network, which may exert a protective effect on the underlying PHBV structure, helping retain structural integrity for longer periods.

4.2.3.3.4. Vibrational spectra of the hydrogel-loaded scaffold

FTIR-ATR spectra allow at least partial assessment of several important aspects: first, that PHBV scaffolds can hold the hydrogels; second, that the degradation trends of the hydrogels inside the scaffolds follow the same qualitative behavior observed in the hydrogel films; and third, whether loading of the hydrogel into the interior of the structures was attained or if the hydrogel merely formed a surface coating. To further assess the consistency of these aspects, different samples were used for each timepoint (rather than repeatedly measuring the same sample). The results are presented in Figures 4.12, 4.13 and 4.14 for riboflavin-, fructose-, and EDC-NHS-crosslinked hydrogel-loaded scaffolds, respectively.

All FTIR-ATR spectra present characteristic peak of both PHBV and gelatin. Regarding gelatin, the peaks at 1634, 1526, and 1240 cm^{-1} correspond to the –C=O and –NH vibrations of the amide I, –NH and –CN vibrations of the amide II, and –CN and –NH vibrations of amide III respectively [21]. PHBV is manifested mainly by the 1724 cm^{-1} band that represents the stretching vibration of the C=O bonds from ester functional groups [22], as well as C–O stretching at 1183, 1133 and 1057 cm^{-1} while peaks that bookend this middle zone can be attributed to C–H stretching of methyl (CH_3) and methylene (CH_2) deformations [23, 24]. A series of smaller PHBV peaks at 1275, 1261, 1227, 1180, 1054, and 1044 cm^{-1} [24] also overlap the amide III region, making this band difficult to distinguish in the composite spectra.

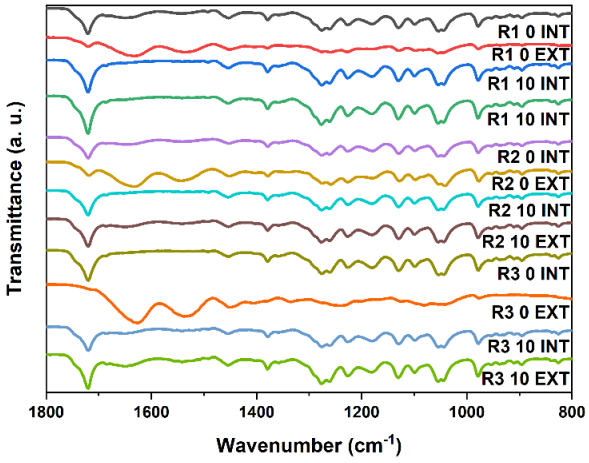


Figure 4.12. FTIR-ATR spectra of the interior and exterior of PHBV scaffolds loaded with Gelatin-Riboflavin hydrogels before and after immersion in water (R1: 0.2% riboflavin, 1 h crosslinking; R2: 0.2% riboflavin, 2 h crosslinking; R3: 0.4% riboflavin, 2 h crosslinking); before (Day 0) and after immersion in water for 10 days; and the interior (INT) or exterior (EXT) of the scaffolds.

A slight shift of the amide II band from 1536 to 1540 cm^{-1} is observed, occurring from day 0 in R1 to R2, as well as the day 10 R3 sample. Although the shift is small, Wang *et al.* [25] have associated similar blue shifts in amide II and III (which in the present case is hard to discern, as mentioned above) with increasing degrees of riboflavin-mediated UV crosslinking. Thus, even minor shifts may reflect differences in crosslinking density.

Day 10 R1 samples show an absence of the hydrogel initially present, as anticipated. More surprisingly, day 10 R2 sample of the scaffold's exterior presents a small but noticeable amide I peak. Given this observation, it is positively therefore not unexpected that the R3 hydrogel is also present after 10 days, as R3 exhibits both higher UV exposure time and higher concentration of riboflavin. This is further indication that the degree of crosslinking is greater in R3 than R2, and in R2 than R1. It is also a significant finding that the amide peaks are observed both on the inside and outside of the scaffold, suggesting that the polymer structure may also be providing some physical protection for the hydrogel, thereby delaying its degradation.

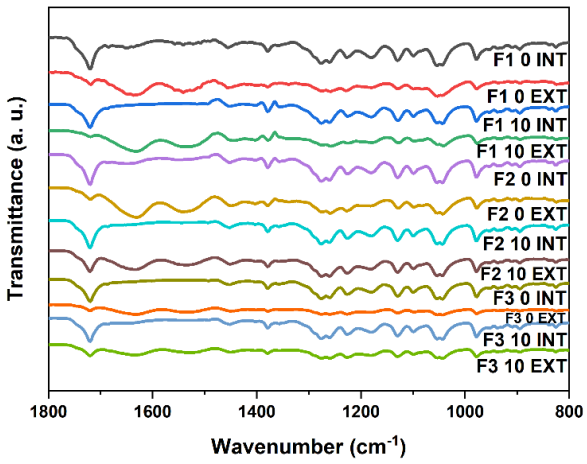


Figure 4.13. FTIR-ATR spectra of the interior and exterior of PHBV scaffolds loaded with Gelatin-Fructose hydrogels before and after immersion in water (F1: pH 7, 80 °C; F2: pH 10, 80 °C; F3: pH 10, 110 °C); before (Day 0) and after immersion in water for 10 days; and the interior (INT) or exterior (EXT) of the scaffolds.

For the fructose hydrogels, some results are somewhat similar. Although small shifts of 2 to 4 cm^{-1} have been associated with the MR [19], they are typically disregarded due to the change being too subtle to be precise, and it is usually assumed that no significant spectral changes arise from this reaction [26]. Amide I is visible in the scaffold's interior of day 0 F1 and F2, but not in F3. However, day 10 F3's interior does indeed present a small amide I peak, which is similar to what happens in the R3 sample. As some

samples' interiors reveal the presence of gelatin at day 10 but not day 0, this can only be attributed to a non-homogeneous distribution of the hydrogel in the interior of the structure. This may happen due to imperfect penetration of the hydrogel into the structure, potentially caused by obstructed pores and fluid-flow limitations associated with the hydrophobic nature of PHBV while gelatin cools after immersion of the PHBV scaffolds in the solution. At day 10, the exterior of all samples still possesses the fructose-crosslinked gelatin hydrogel. Again, its presence in F1 (and F2 to a lesser extent) is surprising when considering Figure 4.10, further supporting the hypothesis that integration into the scaffolds offers a delay in solubilization. F3, as expected, still carries the hydrogel in both the exterior and interior of the composite scaffolds.

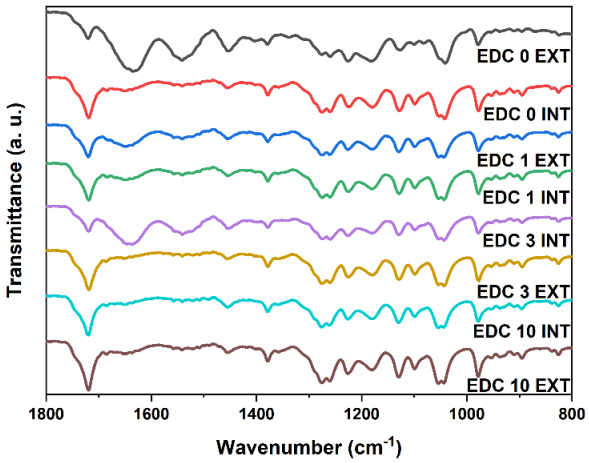


Figure 4.14. FTIR-ATR spectra of the interior and exterior of PHBV scaffolds loaded with Gelatin-EDC-NHS hydrogels before and after immersion in water for 10 days.

Again, crosslinking with EDC/NHS does not induce considerable changes in the FTIR spectra of gelatin [27]. In this case, a combination of factors may be at play, including the protective effect of the composite in delaying solubilization. Although the intensity of the amide I band decreases sharply between day 3 and day 10, it remains detectable at the latter time point. Again, given that in the swelling studies the Gelatin-EDC-NHS samples solubilized by day 3, this reinforces the possibility of a protective effect and a consequent slowing of hydrogel degradation.

It is also observed throughout all hydrogels (as is the case for R1 0 EXT and R3 0 EXT), that over time the amide I band at 1634 cm^{-1} progressively diminishes as the PHBV peak at 1724 cm^{-1} intensifies, confirming both the presence of a hydrogel coating and the progressive exposure of the PHBV structure as the hydrogels dissolve.

4.2.3.3.5. Assessment of the degradation of the hydrogel-loaded scaffold

The representative UV-Vis spectroscopy profiles presented in Figure 4.15 were chosen to illustrate the overall contents found in the PBS medium in which the scaffolds were immersed after the first week. Since the medium was changed and recovered weekly and later samples only presented progressively lower intensity absorbance peaks at the same positions, these spectra were selected as representative data.

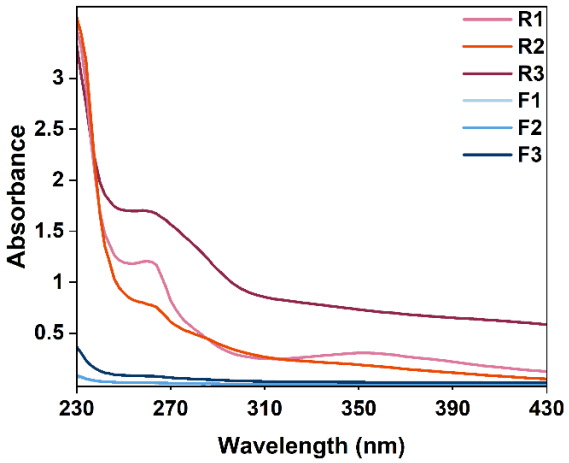


Figure 4.15. Representative UV-Vis spectroscopy spectra of Gelatin-Riboflavin and Gelatin-Fructose-loaded PHBV scaffolds. PBS medium simples recovered after 7 days of immersion, under static conditions (F1: pH 7, 80 °C; F2: pH 10, 80 °C; F3: pH 10, 110 °C; R1: 0.2% riboflavin, 1 h crosslinking; R2: 0.2% riboflavin, 2 h crosslinking; R3: 0.4% riboflavin, 2 h crosslinking).

The Gelatin-Riboflavin UV-Vis spectroscopy profiles show absorbance peaks around 260 nm which can be attributed to uncrosslinked riboflavin, a compound also associated with peaks around 223 nm. Although this region lies outside the equipment's scan range, all samples show high absorbance values at 230 nm, suggesting that the true peak occurs slightly before the lower detection limit. This high initial absorbance suggests the presence of components absorbing strongly below this range. R1 also presents a wide, lower intensity peak around 354 nm which can be a manifestation of photodegradation products such as lumicromum and lumiflavin [8, 9].

Meanwhile, although the literature lists several sugar-derived degradation products, such as 5-Hydroxymethylfurfural (HMF) and furfural [28], or browning intermediates of the MR [29], as compounds that may be detected in UV-Vis scans, no clear spectral signatures of these species appear in our measurements, aside from small absorbance values around 230 nm. Again, fructose monomer absorbance is weak under the typical UV-Vis scan range, with typical bands occurring at 210-220 nm. It

is plausible that the small absorbance observed near 230 nm originates from unreacted fructose, as it is expected that not all of the crosslinker reacts with gelatin.

4.2.3.4. Cell studies

4.2.3.4.1. Cytotoxicity studies

Figure 4.16 shows the results from the indirect cytotoxicity assays performed. The results show that all hydrogel films exhibited average cell viability above the 70% threshold outlined by the ISO 10993-5 standard, with all formulations remaining within the non-cytotoxic range. The highest values among the fructose and riboflavin formulations correspond to samples F1 and F2, with values of 83.7 ± 3.8 and 89.7 ± 4.7% respectively. F3, R1, R2 and R3 all present average values in the ≈73-75% range. The EDC-NHS hydrogel samples presented average cell viability of 97.8 ± 4.3%, close to the negative control and clearly above all other hydrogel conditions. Although all average values are above the ISO threshold, the fructose- and riboflavin-crosslinked hydrogels show comparatively lower viability and a narrower safety margin than the EDC-NHS formulation. Therefore, considering both cytocompatibility and structural stability, gelatin-EDC-NHS hydrogels were selected for the assessment of adhesion and proliferation of the 3D scaffolds studied in Chapter 2 loaded with this hydrogel.

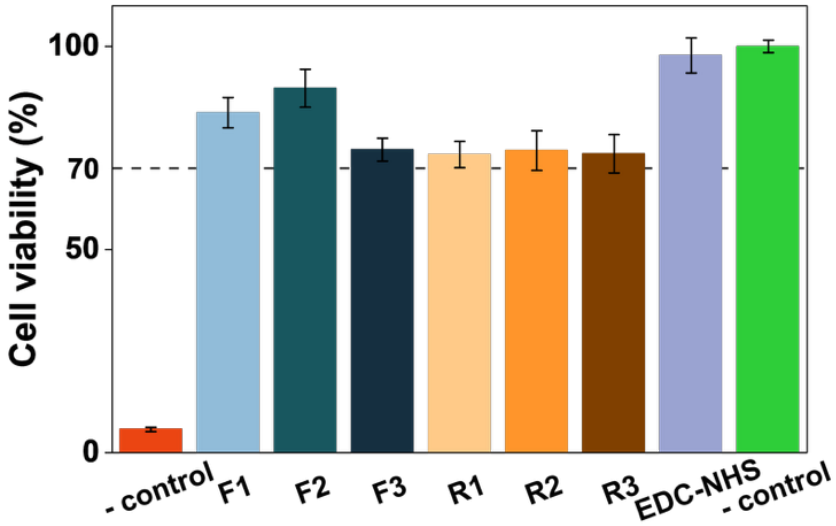


Figure 4.16. Indirect cytotoxicity assay of MC3T3-E1 preosteoblasts in contact with the Gelatin-Fructose and Gelatin-Riboflavin hydrogel films and Gelatin-EDC-NHS hydrogels. (F1: pH 7, 80 °C; F2: pH 10, 80 °C; F3: pH 10, 110 °C; R1: 0.2% riboflavin, 1 h crosslinking; R2: 0.2% riboflavin, 2 h crosslinking; R3: 0.4% riboflavin, 2 h crosslinking).

4.2.3.4.2. Proliferation studies

After confirming that all hydrogel formulations were not cytotoxic, preliminary adhesion tests (data not shown) revealed marked differences between them. Gelatin-Riboflavin and Gelatin-Fructose hydrogels showed poor initial cell attachment, whereas the EDC-NHS-crosslinked hydrogel supported consistent adhesion. This behavior is consistent with the chemical profiles discussed in section 4.2.3.3.5, where the presence of unreacted or partially reacted photo- and sugar-derived species may contribute to suboptimal cell–material interactions. Furthermore, considering future work, this crosslinking method appears to be the most suitable among the three for investigating the 3D printing of hydrogel structures that remain stable in solution over extended periods. Given its superior cytocompatibility, adhesion performance and structural stability in aqueous environments, the EDC-NHS-crosslinked hydrogel was selected for the proliferation studies. Adhesion and proliferation were therefore assessed under static and dynamic conditions to evaluate the combined effects of magnetic stimulation and hydrogel incorporation on preosteoblast behavior. The results are presented in Figure 4.17.

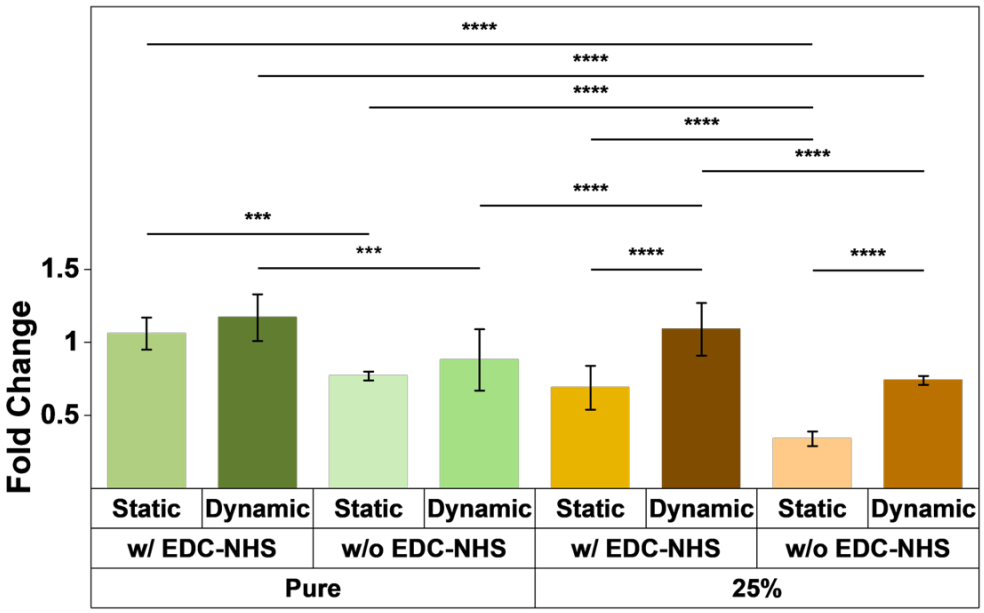


Figure 4.17. Cell proliferation of MC3T3-E1 preosteoblast culture after 4 days under static and dynamic conditions. The cell proliferation values of the pure and composite PHBV scaffolds both with and without the Gelatin-EDC-NHS hydrogel were determined regarding the cells adhered on the material after 24 h adhesion, just before the first magnetic stimulus. The results are expressed as mean ± SD. *** $p < 0.001$, ****$p < 0.0001$.

Cell proliferation is observed on all samples. The second most important observation is that every sample containing hydrogel, under the same stimulus condition and of the same composition, exhibits a higher average fold-change value than its hydrogel-free counterpart, demonstrating that the EDC-NHS hydrogel is not only biocompatible but also actively enhances cell proliferation on the polymeric scaffolds.

Importantly, the proliferation advantage in hydrogel-containing scaffolds is also consistent with their higher local stiffness, since the incorporation of the hydrogel increases the effective modulus of the composite system.

While still promoting higher cell proliferation than samples without hydrogel, scaffolds containing 25% Fe_3O_4 show lower static proliferation compared with their pure polymer counterparts, which is consistent with observations in Chapter 2, where 20% Fe_3O_4 PHBV scaffolds seemed to perform worse than to both pure and 10% NP-loaded scaffolds. Under static conditions, the pure PHBV scaffold exhibits nearly twice the proliferation observed for the 25% Fe_3O_4 scaffold without hydrogel, whereas under dynamic conditions the observed behavior differs substantially. The coupled magnetostrictive and piezoelectric effects of the scaffolds appear to positively influence cell proliferation, as the difference between static and dynamic conditions is substantially larger in composite scaffolds than in pure ones. This is further supported by the higher average fold-change values of scaffolds containing MNPs compared with their pure counterparts under magnetic stimulation, reinforcing the contribution of the magnetoelectric effect. Although pure PHBV scaffolds also show slightly higher average values under dynamic conditions, these differences are not statistically significant, and the improvement in Fe_3O_4-containing scaffolds is considerably more noticeable. Average fold-change increases were as follows: 0.67 to 1.09 in 25% Fe_3O_4 with hydrogel, 0.34 to 0.73 in 25% Fe_3O_4 without hydrogel, 1.05 to 1.17 in pure scaffolds with hydrogel, and 0.77 to 0.88 in pure scaffolds without hydrogel, corresponding to approximate 63%, 115%, 11% and 14%, respectively. These quantitative differences clearly demonstrate that magnetic stimulation exerts a disproportionately stronger proliferative effect when magnetic NPs are present. The notably higher proliferation observed in the 25% Fe_3O_4 sample without hydrogel is likely related to rapid hydrogel solubilization and subsequent cell detachment, as by T_1 the hydrogel is considerably degraded despite the partial protective effect of the polymer matrix. Further investigations using higher crosslinking degrees or shorter culture durations (e.g., 48 h) may clarify this behavior. Nonetheless, the overall results indicate that magnetic stimulation and hydrogel incorporation exert beneficial, and often synergistic, effects on preosteoblast proliferation.

Fluorescence microscopy images corresponding to these studies are presented in Figure 4.18. These results did not fully reproduce the quantitative differences observed in Figure 4.17, as distinctions

between samples with and without hydrogel were difficult to visualize. This is likely due to the fixation and staining process: repeated washings almost certainly removed a substantial fraction of the already fragile hydrogel, as previously discussed.

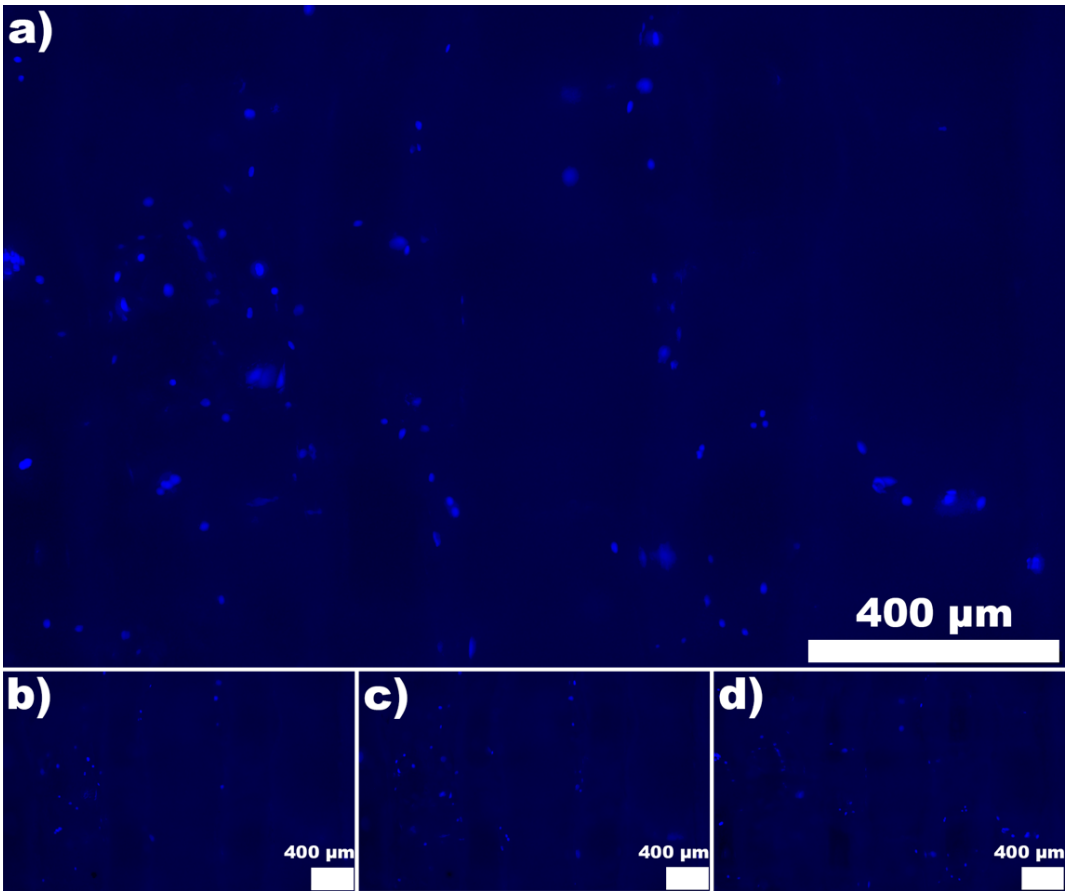


Figure 4.18. a) Composite of three layers of **b)**, **c)**, **d)** different z-axis focal points fluorescence microscopy images of MC3T3-E1 cells adhered on the same sample of a Gelatin-EDC-NHS hydrogel-loaded pure PHBV scaffold, under static conditions, after 4 days (T_1).

Still, carefully examination of pure PHBV scaffold loaded with hydrogel at different focal depths allowed meaningful interpretation. Cells were observed not only on the scaffold surface but also deep within its interior, and some cells appeared located within pore spaces, suggesting that remnants of hydrogel persisted locally and supported cellular proliferation prior to washing. Background fluorescence was higher than that observed in Figure 2.9 (Chapter 2), making interpretation more challenging, but the overall evidence remains consistent with the proliferation assay results.

This internal colonization further supports the suitability of the hydrogel as an infiltration matrix capable of supporting 3D cell organization, which is essential for bone tissue engineering applications.

4.2.4. Conclusions

This study demonstrates the feasibility of hydrogel-loaded PHBV-based scaffolds as multiresponsive electroactive platforms for bone tissue regeneration, providing a solid foundation for further development and future *in vivo* research and implementation.

Different crosslinkers and crosslinking methods were employed to prepare hydrogel films and hydrogel-loaded pure PHBV and composite (25% Fe_3O_4) scaffolds. Gelatin was crosslinked by UV exposure using riboflavin; fructose combined with exposure to high temperatures promoted crosslinking by MR; lastly, EDC-NHS as a chemical crosslinking agent was used. Gelatin-Riboflavin and Gelatin-Fructose hydrogel films were characterized regarding their swelling and solubility, and while the different preparations of riboflavin-crosslinked films were stable for up to 48 h, fructose-crosslinked films offer the option for either short-term stability (F1, < 24 h) or extended stability in PBS solution (F3, still intact at day 30).

Degradation of these hydrogels loaded into the scaffolds was also evaluated under static and dynamic conditions, with mixed results relating to the stimulation effects, although some samples, such as the F3-loaded scaffolds, clearly showed lower mass loss due to their higher stability, as well as slightly increased degradation under magnetic stimulation. As riboflavin samples largely solubilize long before the 30-day mark, results are more homogeneous. FTIR-ATR analysis of the interior of the hydrogel-loaded scaffolds indicated a prolonged hydrogel persistence, likely due to the scaffolds imposing a protective effect by reducing direct exposure to the medium. This medium was also analyzed for degradation byproducts or uncrosslinked agents. Peaks associated with photodegradation products such as lumicromum and lumiflavin were detected, with a strong possibility of the presence of uncrosslinked riboflavin. While all hydrogels were shown to be non-cytotoxic in the indirect assays, these leachable components may have contributed to the inferior adhesion performance of the riboflavin- and fructose-based hydrogels, which is why EDC-NHS-crosslinked hydrogels were selected for the proliferation assays.

The magnetostrictive effect on composite scaffolds, as well as the presence of Gelatin-EDC-NHS hydrogels, were shown to exert a beneficial effect on cell proliferation. While the performance of the static composite samples was lower than that of the pure polymer samples, consistent with the observations in Chapter 2, dynamic conditions induced a strong positive effect that had not been previously observed. It is likely that a higher nanoparticle content (25% versus 10% and 20%) promotes faster proliferation due to the magnetostrictive response within the shorter culture period considered here (3 versus 7 days). However, the hypothesis that composites with higher nanoparticle content are more susceptible to structural disintegration should be directly validated in future studies.

Overall, these results validate the hydrogel-loaded electroactive scaffolds as a robust and versatile platform for bone TE, demonstrating the combined relevance of material design, magneto-mechanical stimulation, and biochemical tuning in accelerating cellular responses.

References

[1] H. Nasution *et al.*, "Hydrogel and Effects of Crosslinking Agent on Cellulose-Based Hydrogels: A Review," *Gels,* vol. 8, no. 9, p. 568, 2022, doi: https://doi.org/10.3390/gels8090568.

[2] W. Hu, Z. Wang, Y. Xiao, S. Zhang, and J. Wang, "Advances in crosslinking strategies of biomedical hydrogels," *Biomaterials science,* vol. 7, no. 3, pp. 843-855, 2019, doi: https://doi.org/10.1039/C8BM01246F.

[3] K. Su and C. Wang, "Recent advances in the use of gelatin in biomedical research," *Biotechnology letters,* vol. 37, no. 11, pp. 2139-2145, 2015, doi: https://doi.org/10.1007/s10529-015-1907-0.

[4] J. Gómez-Estaca, M. C. Gómez-Guillén, F. Fernández-Martín, and P. Montero, "Effects of gelatin origin, bovine-hide and tuna-skin, on the properties of compound gelatin–chitosan films," *Food Hydrocolloids,* vol. 25, no. 6, pp. 1461-1469, 2011, doi: https://doi.org/10.1016/j.foodhyd.2011.01.007.

[5] C. Campiglio, C. Marcolin, and L. Draghi, "Electrospun ECM macromolecules as biomimetic scaffold for regenerative medicine: Challenges for preserving conformation and bioactivity," *AIMS Materials Science,* vol. 4, no. 3, pp. 638-669, 2017, doi: https://doi.org/10.3934/matersci.2017.3.638.

[6] C. Li, L. Sheng, G. Sun, and L. Wang, "The application of ultraviolet-induced photo-crosslinking in edible film preparation and its implication in food safety," *LWT,* vol. 131, p. 109791, 2020, doi: https://doi.org/10.1016/j.lwt.2020.109791.

[7] S. Talreja and S. Tiwari, "A Study on Aromatic Heterocyclic Organic Compounds," *Journal of Pharmaceutical Research International,* vol. 34, no. 41B, 2022, doi: https://doi.org/10.9734/jpri/2022/v34i41B36284.

[8] M. Taghizadeh *et al.*, "Photosensitizer-induced cross-linking: A novel approach for improvement of physicochemical and structural properties of gelatin edible films," *Food Research International,* vol. 112, pp. 90-97, 2018, doi: https://doi.org/10.1016/j.foodres.2018.06.010.

[9] M. A. Sheraz, S. H. Kazi, S. Ahmed, Z. Anwar, and I. Ahmad, "Photo, thermal and chemical degradation of riboflavin," *Beilstein Journal of Organic Chemistry,* vol. 10, pp. 1999-2012, 2014, doi: https://doi.org/10.3762/bjoc.10.208.

[10] P. Liu, X. Lu, N. Li, Z. Zheng, and X. Qiao, "Characterization, Variables, and Antioxidant Activity of the Maillard Reaction in a Fructose–Histidine Model System," *Molecules,* vol. 24, no. 1, p. 56, 2019, doi: https://doi.org/10.3390/molecules24010056.

[11] M. N. Lund and C. A. Ray, "Control of Maillard Reactions in Foods: Strategies and Chemical Mechanisms," *Journal of Agricultural and Food Chemistry,* vol. 65, no. 23, pp. 4537-4552, 2017, doi: https://doi.org/10.1021/acs.jafc.7b00882.

[12] C. Hauser, U. Müller, T. Sauer, K. Augner, and M. Pischetsrieder, "Maillard reaction products as antimicrobial components for packaging films," *Food Chemistry,* vol. 145, pp. 608-613, 2014, doi: https://doi.org/10.1016/j.foodchem.2013.08.083.

[13] L. Tappy and K.-A. Lê, "Metabolic Effects of Fructose and the Worldwide Increase in Obesity," *Physiological Reviews,* vol. 90, no. 1, pp. 23-46, 2010, doi: https://doi.org/10.1152/physrev.00019.2009.

[14] P. Guerrero *et al.*, "Effect of Fructose and Ascorbic Acid on the Performance of Cross-Linked Fish Gelatin Films," *Polymers,* vol. 12, no. 3, p. 570, 2020, doi: https://doi.org/10.3390/polym12030570.

[15] A. Etxabide, M. Urdanpilleta, I. Gómez-Arriaran, K. de la Caba, and P. Guerrero, "Effect of pH and lactose on cross-linking extension and structure of fish gelatin films," *Reactive and Functional Polymers,* vol. 117, pp. 140-146, 2017, doi: https://doi.org/10.1016/j.reactfunctpolym.2017.04.005.

[16] B. Jayachandran, T. N. Parvin, M. M. Alam, K. Chanda, and B. MM, "Insights on Chemical Crosslinking Strategies for Proteins," *Molecules,* vol. 27, no. 23, p. 8124, 2022, doi: https://doi.org/10.3390/molecules27238124.

[17] K. Adamiak and A. Sionkowska, "Current methods of collagen cross-linking: Review," *International Journal of Biological Macromolecules,* vol. 161, pp. 550-560, 2020, doi: https://doi.org/10.1016/j.ijbiomac.2020.06.075.

[18] S.-F. Chou, L.-J. Luo, J.-Y. Lai, and D.-K. Ma, "Role of solvent-mediated carbodiimide cross-linking in fabrication of electrospun gelatin nanofibrous membranes as ophthalmic biomaterials," *Materials science & engineering. C, Materials for biological applications,* vol. 71, pp. 1145-1155, 2017, doi: https://doi.org/10.1016/j.msec.2016.11.105.

[19] D. Dechojarassri, R. Kaneshige, H. Tamura, and T. Furuike, "Preparation and Characterization of Crosslinked Electrospun Gelatin Fabrics via Maillard Reactions," *Materials,* vol. 16, no. 11, p. 4078, 2023, doi: https://doi.org/10.3390/ma16114078.

[20] H. Kchaou, N. Benbettaieb, M. Jridi, M. Nasri, and F. Debeaufort, "Influence of Maillard reaction and temperature on functional, structure and bioactive properties of fish gelatin films," *Food Hydrocolloids,* vol. 97, p. 105196, 2019, doi: https://doi.org/10.1016/j.foodhyd.2019.105196.

[21] H. Staroszczyk, K. Sztuka, J. Wolska, A. Wojtasz-Pająk, and I. Kołodziejska, "Interactions of fish gelatin and chitosan in uncrosslinked and crosslinked with EDC films: FT-IR study," *Spectrochimica Acta Part A: Molecular and Biomolecular Spectroscopy,* vol. 117, pp. 707-712, 2014, doi: https://doi.org/10.1016/j.saa.2013.09.044.

[22] A. Aramvash, S. Hajizadeh-Turchi, F. Moazzeni-zavareh, N. Gholami-Banadkuki, N. Malek-sabet, and Z. Akbari-Shahabi, "Effective enhancement of hydroxyvalerate content of PHBV in Cupriavidus necator and its characterization," *International Journal of Biological Macromolecules,* vol. 87, pp. 397-404, 2016, doi: https://doi.org/10.1016/j.ijbiomac.2016.03.002.

[23] M. Kansiz, H. Billman-Jacobe, and D. McNaughton, "Quantitative Determination of the Biodegradable Polymer Poly(β-hydroxybutyrate) in a Recombinant Escherichia coli Strain by Use of Mid-Infrared Spectroscopy and Multivariative Statistics," *Applied and Environmental Microbiology,* vol. 66, no. 8, pp. 3415-3420, 2000, doi: https://doi.org/10.1128/AEM.66.8.3415-3420.2000.

[24] G. M. Kim, G. H. Michler, S. Henning, H. J. Radusch, and A. Wutzler, "Thermal and spectroscopic characterization of microbial poly(3-hydroxybutyrate) submicrometer fibers prepared by electrospinning," *Journal of Applied Polymer Science,* vol. 103, no. 3, pp. 1860-1867, 2007, doi: https://doi.org/10.1002/app.25348.

[25] K. Wang, W. Wang, X. Wu, J. Xiao, Y. Liu, and A. Liu, "Effect of photochemical UV/riboflavin-mediated cross-links on different properties of fish gelatin films," *Journal of Food Process Engineering,* vol. 40, no. 5, p. e12536, 2017, doi: https://doi.org/10.1111/jfpe.12536.

[26] S. Ahmed, N. Doğan, C. Doğan, and Y. Akgul, "A Novel Approach to Crosslink Gelatin Nanofibers Through Neutralization-Induced Maillard Reaction," *Food and Bioprocess Technology,* vol. 17, no. 2, pp. 489-503, 2024, doi: https://doi.org/10.1007/s11947-023-03146-6.

[27] J. Skopinska-Wisniewska, M. Tuszynska, and E. Olewnik-Kruszkowska, "Comparative Study of Gelatin Hydrogels Modified by Various Cross-Linking Agents," *Materials,* vol. 14, no. 2, p. 396, 2021, doi: https://doi.org/10.3390/ma14020396.

[28] H. Zhang, Q. Ping, J. Zhang, and N. Li, "Determination of Furfural and Hydroxymethyl furfural by UV Spectroscopy in ethanol-water hydrolysate of Reed," *Journal of Bioresources and Bioproducts,* vol. 2, no. 4, pp. 170-174, 2017, doi: https://doi.org/10.21967/jbb.v2i4.84.

[29] A. Nurrulhidayah, "Optimisation of browning index of maillard reaction in gelatine powder by response surface methodology (RSM) for halal authentication," *Food Research,* vol. 3, no. 5, pp. 525-529, 2019, doi: https://doi.org/10.26656/fr.2017.3(5).116.

CHAPTER 5

Conclusions and future work

5.1. Concluding remarks

With the advance of modern medicine promoting increasingly longer life expectancy, TE solutions are ever-more required to maintain quality of life in later years, as well as providing treatments that offer faster recovery after accidental damage or invasive procedures. As bone is a naturally electroactive tissue regulated by electrical and mechano-electrical cues, preosteoblasts cells were selected as the most suitable cellular model for the development of a multiresponsive electroactive platform, enabling the exploration of different types of structures and materials combinations.

In **Chapter 2**, the suitability of PHBV and PHBV/Fe_3O_4 composite scaffolds as electroactive microenvironments for MC3T3-E1 preosteoblast adhesion and proliferation was demonstrated across all experimental conditions, whether static or dynamic and regardless of NP content. However, the 20% NP fraction presented slightly lower performance than the pure polymer and 10% NP samples, likely due to earlier loss of structural integrity. This hypothesis was supported by detailed physicochemical characterization, which revealed non-homogeneous NP distribution and a decrease in Young's modulus in composite scaffolds. Degradation studies in PBS and DMEM further showed accelerated structural degradation in composite scaffolds under magnetic stimulation over 40 days. Together, these findings support why magnetic stimulation enhanced cell proliferation most effectively in the 10% Fe_3O_4 scaffolds, where structural integrity was still preserved.

The development of microspheres as an additional structural element to be integrated into hydrogels, either to fine-tune degradation behavior or to serve as electrically active cargo, was presented in **Chapter 3**. $CoFe_2O_4$@PHBV microspheres were synthetized using an emulsion method and characterized in terms of magnetic properties and size distribution. Although partial aggregation occurred, the challenge became more pronounced in Fe_3O_4@PHBV microspheres, prompting the transition to electrospray processing. This allowed the successful fabrication of Fe_3O_4@PVDF microspheres with suitable roundness and dispersion: 80% of microspheres were below 1 μm, while larger droplets (≈ 5 μm) could be removed through filtration, demonstrating that a fully integrable microstructured system was achieved.

Chapter 4 was divided in two main works concerning hydrogels. **Subchapter 4.1** focused on the 3D printing of a biocompatible gelatin-sericin hydrogel without chemical crosslinking. Sericin concentrations of 0.75, 2 and 3.25% w/v and a gelatin concentration of 2% w/v were used to prepare the hydrogels. Rheological analysis confirmed shear-thinning behavior suitable for extrusion during 3D printing, and higher sericin content led to higher viscosity and improved shape fidelity. FTIR-ATR analyses revealed interactions between gelatin and sericin, which correlated with swelling and degradation

behavior: higher sericin content led to lower swelling and preservation of structural integrity for a longer period. Indirect cytotoxicity studies confirmed the non-cytotoxicity of these samples. However, maintaining stability in PBS medium long enough to support cell proliferation proved challenging, motivating the exploration of alternative gelatin-based hydrogels.

Subchapter 4.2 addressed this by developing three different gelatin-based hydrogels, crosslinked respectively with riboflavin (UV-mediated), fructose (MR), and EDC–NHS (carbodiimide chemistry). Of these, EDC-NHS crosslinking produced the most structurally stable hydrogel within the PHBV and composite scaffolds, enabling successful proliferation studies. Cell studies showed that both magnetostrictive effect of the composite scaffolds and the presence of Gelatin-EDC-NHS hydrogel promoted significantly higher proliferation when compared with unloaded or unstimulated scaffolds. Although preliminary adhesion on Gelatin-Riboflavin and Gelatin-Fructose hydrogels was inconsistent, all developed hydrogels were successfully integrated into the polymeric scaffolds and characterized thoroughly. These last two hydrogels were also processed in the form of hydrogel films. Gelatin-Riboflavin and Gelatin-EDC-NHS hydrogels displayed short-term stability (0–48 h), whereas the Gelatin-Fructose hydrogel exhibited markedly prolonged stability, maintaining integrity beyond 30 days in PBS. When loaded into scaffolds, these hydrogels also exhibited lower mass loss, indicating a protective effect on the polymer. Conversely, FTIR analysis revealed that the polymer scaffold also exerted a protective role, delaying hydrogel degradation by shielding interior regions from direct exposure to the medium. Degradation medium analyses identified photodegradation products such as lumicromum and lumiflavin, and although full consumption of riboflavin and fructose could not be confirmed, all hydrogels were classified as non-cytotoxic.

The combination of EDC-NHS-crosslinked hydrogels with polymeric and composite scaffolds thus demonstrated itself as a robust platform for bone TE, exploiting magnetoelectric stimulation to promote preosteoblast growth. Microspheres and hydrogel films, developed in earlier chapters, expand the toolbox of available structural and functional components, opening multiple future directions for constructing increasingly complex multiresponsive systems.

Overall, this thesis establishes a coherent, experimentally validated foundation for the development of multiresponsive magnetoelectric platforms for bone tissue regeneration. By integrating polymeric scaffolds, magnetostrictive fillers, functional hydrogels and microscale components, it advances the design of next-generation electroactive biomaterials and opens multiple avenues for translation into preclinical regenerative medicine strategies.

5.2. Future work

The hydrogels integrated into pure and composite PHBV scaffolds and Gelatin-EDC-NHS-loaded scaffolds were proven to be promising as multiresponsive platforms for bone tissue regeneration. Already combining the piezoelectric and magnetoelectric effects, the integration of agents such as growth factors into the hydrogel should not pose an obstacle and would further enhance control over cell proliferation and differentiation.

Optimal NP content in the polymeric scaffolds, balancing the magnetostrictive effect while minimizing loss of structural integrity, is yet to be determined, although a useful working window for NP wt.% has been established. In addition, optimization of the magnetic stimulation parameters (namely the magnetic field amplitude, frequency and duty cycle) will be essential to determine the stimulation regimes that most effectively enhance osteogenic responses while avoiding potential overstimulation or premature scaffold degradation. Further studies could be carried out to extend the stability of the Gelatin-EDC-NHS hydrogels by using higher concentrations of the crosslinking agents. Ideally, hydrogel stability would be extended to approximately 30 days to allow MC3T3-E1 differentiation and mineralization; otherwise, Gelatin-Fructose hydrogels remain a viable alternative, as F3 hydrogels already demonstrate stability in PBS solution at 37 °C for over 30 days. Tuning their degradation rate should be attainable by lowering crosslinking temperature or solution pH.

After this, the microspheres developed in Chapter 3 also assessment of their influence on cell behavior, to determine whether the magnetostrictive effect can be further enhanced by dispersing the spheres within the hydrogel matrix.

The large number of possible combinations left to explore using the developed structures presents ample opportunity to overcome current limitations and tailor the scaffolds for eventual *in vivo* application. For instance, the hydrogel films could be loaded with active agents to be slowly released at defined time points and applied over the scaffolds as a coating. This would separate and allow finer control over the roles of drug release and structural support for cell adhesion and proliferation. The developed microspheres could also be incorporated into the film coating to further fine-tune its degradation behavior.

All together, these elements could transform the already effective scaffolds presented in this work into a more comprehensive and adaptable platform for TE studies, capable of supporting multipronged regenerative strategies.